Chapter 4

Creation of new materials

4.1. Study of energy ions, their varieties and charge on temperature, rate of temperature rise, thermal stresses, and also on the size, amount of volume, number of particles in nanostructures and effective current density for nanostructures

Gennadiy Kostyuk
Department of Theoretical Mechanical Engineering and Robotic-Mechanics Systems,
National Aerospace University named by N. Ye. Zhukovsky “KhAI”, Kharkov, Ukraine
E-mail: *gennadiykostyuk206@gmail.com*

Abstract. On the basis of joint decisions of the problem of heat conduction and thermoelasticity obtained temperature field and thermal stress in which the zones where the nanostructures are formed. For a large number of different ions and charge rules 1 to 3 were obtained according to the volume of the nanostructure, and the depth range, which are implemented by the nanostructure ion energy and charge, determined the effective current density.

Keywords: temperature, thermal stresses, nanostructures, effective current density.

1. Introduction

For nanocrystalline structures on the surface, as is well known, we need a certain temperature (or its rate of increase) in the required amount of pressure and having a metal atom around which the nanostructure.

As shown in [1-11], the action of charged particles on construction materials leads to the appearance of the material to a depth of rather high temperatures under the influence of individual ions of different varieties and heat affected zone has the probability of occurrence of thermal stresses of considerable magnitude, which confirms the possibility of local zones, where it reaches the conditions for the emergence of nanostructures.

To these conditions were realized in a large volume (high temperatures and voltages) is also necessary to ensure maximum filling of the temperature field with high temperatures and at the same time maintain the zone with the highest temperature gradients when implemented high values of thermal stresses. Clearly, a simple increase of ion current density to achieve this would be impossible, as the current density increases the temperature gradients in the adjacent area of the particles is reduced, and hence, reduces the amount of stress and temperature conditions for the formation of nanostructures not performed.

2. Status of the question

Due to the action of ions of various sorts, energy, battery, current densities it is possible to maintain a sufficient temperature (due to the corresponding temperature distribution of the temperature field in depth ensures a high average temperature), at the same time, choosing the location of the field depth (varying power, battery, and type of particle), provides high temperature gradients. Consequently, a fairly large amount of material will act on significant voltage value, i.e. will run conditions for obtaining the crystal structures.

Therefore, several upgraded models of the individual particles of structural materials [1-11], get a model that takes into account relevant factors (in particular, the model does not take into account the charge of the ion and the complex nature of their interference in the rather large amount of consideration).

3. Statement of the research task

Taking as criteria for obtaining nanostructures desired temperature range, the rate of rise of temperature, pressure (thermal stress) and the presence of the catalyst [2], we can consider the possibility of obtaining nanostructures depending on the physical and technological parameters of flow during processing, which will analyze some of the theoretical and technical task (Fig. 1):

I. The model of interaction of streams of ions of different sorts, energy, charge and current densities, which allows:

1) to obtain the depth range, which is likely to receive for each of the nanostructures streams separate and evaluate the effect of flow depth;

2) calculate the distribution of temperature fields and thermal stresses in the amount of detail;

3) to determine the grain size;

4) organize the flow of particles so that the maximum amount of items has been filled the fields of temperature and thermal stress (theoretically and technologically);

5) determine the amount theoretically nanocluster particles in a quantity of nanoclusters formed in unit time.

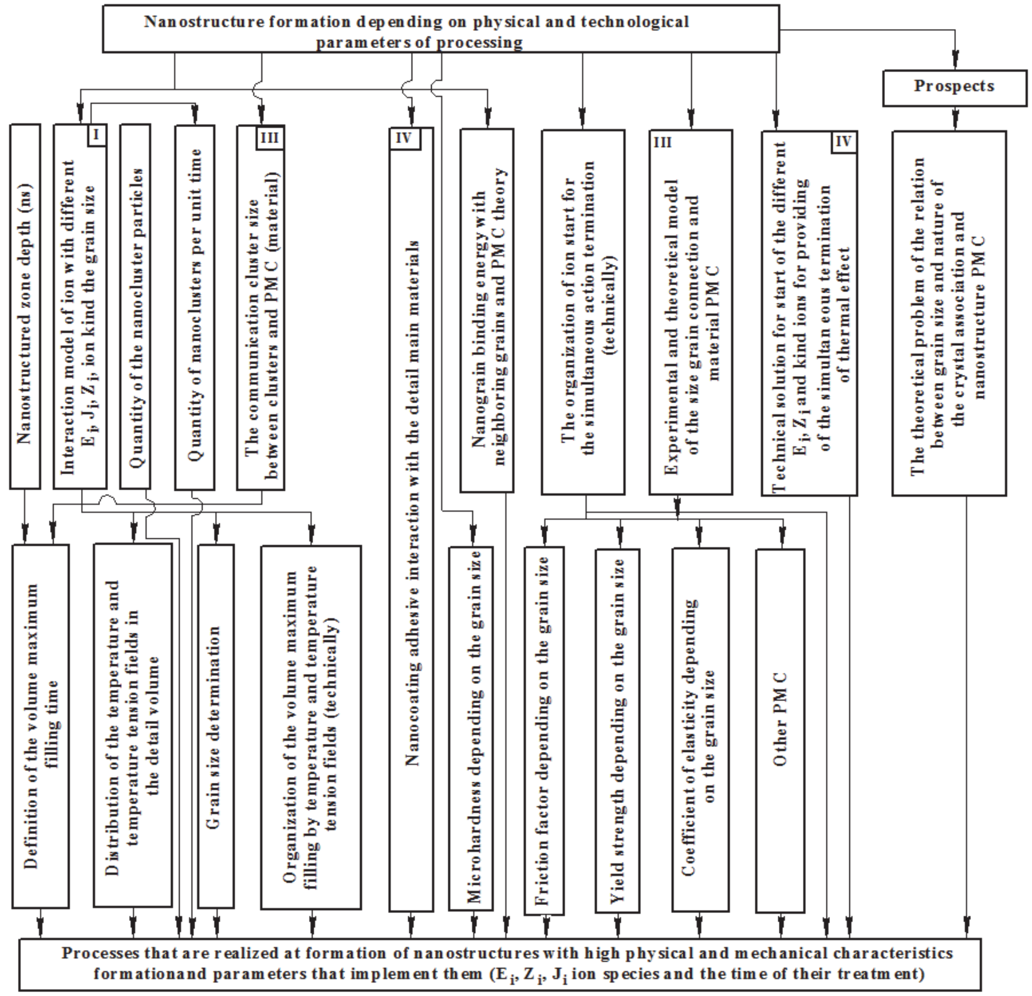

Fig. 1. Processes that are realized at formation of nanostructures with high physical and mechanical characteristics formation

II. The theory of the interaction of nanoclusters (nanocrystals) their size, power relations between them and the physical and mechanical properties of nanostructures, which allows you to:

1) calculate the size of nanoclusters energy ties with neighboring nanoclusters (grains) and physic-mechanical properties of the nanomaterial;

2) to obtain the theoretical dependence of physical and mechanical characteristics of the National Assembly on the grain size, location and nature of their interactions, completeness volume nanostructures.

III. Experimental and theoretical model of grain size due to the FMH:

1) microhardness;
2) the coefficient of friction;
3) the yield strength;
4) tensile strength;
5) The modulus of elasticity;
6) wear;
7) resistance of cutting tools (RI).

1. Adhesion bond nano-coatings to the base material part (theory).

2. Technical solution: software start flow of ions of different sorts, energy, charge and current densities.

Solving these problems will help you find the physical and technological parameters of ion fluxes, which will provide the desired physical and mechanical properties of nanostructures and nanomaterials.

Now consider the real possibility of implementing these tasks.

4. Model of the action of an individual ion on a structural material

The interaction of charged particles and plasma flows with structural materials related to the implementation of a wide range of processes: collisional, thermal, thermomechanical thermal fatigue, diffusion, thermochemical and plasma, but there are currently no job, taking into account these factors and the more their relationship. These processes influence both on the nature of heat transfer in the target volume and on the surface, so keeping these processes needed in the balance of energy in a volume element of a metal target and a target heat exchange surface, i.e. in boundary conditions.

4.1. Heat balance in an elementary volume of a part

Change the amount of heat per unit volume (the first term in the left-hand side of Eq. (1)) can be realized by moving the particle flow along the surface to be treated or moving target with respect to the plasma flow at a speed V_p (second term), thermal processes influence on heat transfer finite speed of propagation of heat (third term), thermal conductivity (the first term on the right), the displacement of the evaporation front (second term), point (third term); collisional processes: volumetric heat source due to the action of the particle (the fourth term), energy consumption in the displacement of atoms (fifth term); thermo-elastic, thermoplastic and thermal fatigue processes that determine the energy of deformation of the material elementary volume (six terms); diffusion processes that determine the heat transfer diffusing material (seventh term); thermochemical processes related to the implementation of chemical reactions between the material of the target and bombarding ions or between the alloy components in composite materials and Lentz-Joule heating due to the spreading of the ion current:

$$\begin{aligned}
&C[T]\cdot\gamma[T]\frac{dT(x,y,z,t)}{dt}+C[T]\cdot\gamma[T]\frac{\partial T(x,y,z,t)}{\partial y}\cdot V_n\\
&\quad+C[T]\cdot\gamma[T]\cdot\tau_{rt}\frac{d^2T(x,y,z,t)}{dt^2}=\nabla\lambda[T\cdot\nabla T](x,y,z,t)+C[T]\cdot\gamma[T]\cdot V\frac{\partial T(x,y,z,t)}{\partial x}\\
&\quad-A\cdot L_{m.m}\cdot\gamma[T]\frac{dV_{m.m}}{dt}+B\cdot j_{i,e}\cdot\mu_{i,e}\frac{\partial E_{i,e}}{\partial x}-E_{dis}\cdot S_{dis}\frac{j_{i,e}}{\lambda_{cpi,e}}\pm D\frac{dW(x,y,z,t)}{dt}\\
&\quad\pm m_a\cdot C_a[T_a]\frac{dn_a}{dt}\big(T_a-T(x,y,z,t)\big)\pm P_{T.C.}(n_A,n_B,T,t_e)\frac{dn_{A(B)}}{dt}L_{T.C.}\\
&\quad+\rho[T]\cdot j^2(x,y,z,t),
\end{aligned}\tag{1}$$

where $C[T]$ and $\gamma[T]$ – specific heat and density of the target material corresponding to a temperature T; τ_r – the relaxation time of one Kelvin temperature; V_n – ion flux moving speed or the target relative thereto; $L_{m.m}$ and $L_{T.C.}$ – specific heat of fusion and thermochemical reaction; $V_f[T]$ – the rate of displacement of the evaporation front; $V_{m.m}$ – the volume of molten metal; $j_{i,e}$ – the current density of ions, electrons or plasma flow; $\mu_{i,e}$ – accommodation coefficient ion and an electron; $-\partial E_{i,e}/\partial x$ loss of ion energy and electron at a depth of target; E_{dis} – the energy of the atomic displacements; S_{dis} – the number of displaced atoms as a result of ion or electron; $\lambda_{cpi,e}$ – linear average free path of ions and electrons in a target material; $W(x,y,z,t)$ – the strain energy per unit volume of the target; m_a – mass diffusing atom; $C_a[T_a]$ – diffusing the heat capacity of the material at a temperature T_a; $P_{T.C.}(n_A,n_B,T,t_{B3})$ – chance of thermochemical reactions, depending on the concentration of the reactants n_A and n_B, temperature T and reaction time t_{B3}; n_A and n_B – reagent concentration, determines the possible reactions; $\rho[T]$ – electrical resistivity at a temperature T; $j(x,y,z,t)$ – the current density based on current spreading.

Strain energy per unit volume is defined as:

$$\begin{aligned}
W=G\Bigg[&\varepsilon_{xx}^2+\varepsilon_{yy}^2+\varepsilon_{zz}^2+2\big(\varepsilon_{xy}^2+\varepsilon_{yz}^2+\varepsilon_{zx}^2\big)+\frac{\mu}{1-\mu}l^2\\
&-\frac{2(1+\mu)\alpha_1}{1-2\mu}l(T(x,y,z,t)-T)\Bigg],
\end{aligned}\tag{2}$$

where $2\varepsilon_{ik}=2\varepsilon_{ki}=\frac{\partial u_k}{\partial i}+\frac{\partial u_i}{\partial k}\ (k,\ i=x,\ y,\ z)$; $l=\varepsilon_{xx}+\varepsilon_{yy}+\varepsilon_{zz}$, ε_{xx}, ε_{yy}, ε_{zz} – extension; ε_{xy}, ε_{yz}, ε_{zx} – shifts relative to the respective axes; u_x, u_y, u_z – movement about respective axes; α_1 – the coefficient of linear expansion of the target material; μ – Poisson's ratio (the ratio of transverse strain to longitudinal μ values are between 0 and 0.5); G – the shear modulus (modulus of the second kind); T_n – initial temperature. for iron $G=$ 3,5,…, 5,3·1010 N/m^2, $\mu=0{,}23,\ \ldots,\ 0{,}31$.

Shear strain ε_{ik} can not be set arbitrarily, they are connected by differential relations – conditions for compatibility:

$$\begin{aligned}
&\frac{\partial^2\varepsilon_{xx}}{\partial y^2}+\frac{\partial^2\varepsilon_{yy}}{\partial x^2}=2\frac{\partial^2\varepsilon_{xy}}{\partial x\,\partial y}, &&\frac{\partial^2\varepsilon_{xx}}{\partial y\,\partial z}=\frac{\partial}{\partial x}\left[-\frac{\partial\varepsilon_{yz}}{\partial x}+\frac{\partial\varepsilon_{zx}}{\partial y}+\frac{\partial\varepsilon_{xy}}{\partial z}\right],\\
&\frac{\partial^2\varepsilon_{yy}}{\partial z^2}+\frac{\partial^2\varepsilon_{zz}}{\partial y^2}=2\frac{\partial^2\varepsilon_{xy}}{\partial z\,\partial y}, &&\frac{\partial^2\varepsilon_{yy}}{xy\,\partial z}=\frac{\partial}{\partial y}\left[-\frac{\partial\varepsilon_{zx}}{\partial y}+\frac{\partial\varepsilon_{xy}}{\partial z}+\frac{\partial\varepsilon_{yz}}{\partial x}\right],\\
&\frac{\partial^2\varepsilon_{xx}}{\partial z^2}+\frac{\partial^2\varepsilon_{zz}}{\partial x^2}=2\frac{\partial^2\varepsilon_{zx}}{xz}, &&\frac{\partial^2\varepsilon_{zz}}{\partial y\,\partial x}=\frac{\partial}{\partial z}\left[-\frac{\partial\varepsilon_{yx}}{\partial z}+\frac{\partial\varepsilon_{yz}}{\partial x}+\frac{\partial\varepsilon_{xz}}{\partial y}\right].
\end{aligned}\tag{3}$$

These conditions verified the correctness of the extensions and changes, and their adjustment the introduction of additional stresses.

To determine elongations ε_{xx}, ε_{yy}, ε_{zz} and shifts ε_{xy}, ε_{yz}, ε_{zx}. We use the expression thermoelastic potential of displacement Φ:

$$\Delta\Phi - \frac{1-2\mu}{2(1-\mu)} \cdot \frac{\gamma}{G} \cdot \frac{\partial^2\Phi}{\partial t^2} = \frac{1+\mu}{1-\mu} \cdot \alpha_1 \cdot [T(x,y,z,t) - T], \tag{4}$$

where γ – density target material.

Considering that the solution of the problem is carried out in a moving coordinate system and output to a landline or close to it mode, the second term in the left side of the Eq. (4) becomes negligible, we obtain:

$$\Delta\Phi = \frac{1+\mu}{1-\mu} \cdot \alpha_1 \cdot [T(x,y,z,t) - T]. \tag{5}$$

The magnitude of thermoelastic potential of displacement and the known ratio is the elongation and shifts:

$$\varepsilon_{ik} = \frac{\partial^2\Phi}{\partial i\,\partial k}, \quad (i,k = x,y,z). \tag{6}$$

The values of thermal stress is defined by the expression:

$$\sigma_{ik} = 2G\left(\frac{\partial^2\Phi}{\partial i\,\partial k} - \Delta\Phi \cdot \delta_{ik}\right), \tag{7}$$

where δ_{ik} subject to the conditions $\delta_{ik} = 0$ at $i \neq k$ $(i,k = x,y,z)$, $\delta_{ik} = 1$ at $i = k$.

The term of the Eq. (1) takes into account the heat transfer diffusing material, the mass of the diffusing atom is defined as:

$$m_a = M \cdot m_p, \tag{8}$$

where M – the atomic weight of the coating material; m_p – proton mass.

The change in concentration of the diffusing atoms per unit time in $t < t_k$ defined as:

$$\frac{dn_a}{dt} = \frac{j}{e \cdot z \cdot \sqrt{\alpha\tau}}.$$

At $t \geq t_k$:

$$\frac{dn_a}{dt} = \frac{j}{e \cdot z \cdot L_D}, \tag{9}$$

where j – current density; e – electron charge; z – atomic number material applied; L_D – part thickness; t_k – the time in which the item is to warm up the entire thickness, $t_k = L_{D2}/\alpha$; α – thermal diffusivity.

The formula to calculate the diffusion coefficient is given by:

$$K_{\text{dif}} = a_{\text{d}} \cdot d_{\text{e}}^2 \cdot V_0 \cdot \exp\left(-\frac{U}{(kT)}\right), \tag{10}$$

where a_d – factor on the order of 0.1, determined by the type of crystal lattice; d_e – the distance between the closest equivalent to the provisions of vacancies in the crystal; V_0 – the order of the frequency of atomic vibrations in a crystal (10^{12}, …, 10^{14} s^{-1}); U – the potential barrier that must be overcome job when skewed to the adjacent position; k – the Boltzmann constant; T – the absolute temperature T.

4.2. Heat transfer on the surface of a part

The heat flux on the target surface created by:

1. Collisional processes heat is generated on the surface due to the action of an electron or ion (the first term on the right), is given the heat flux from the sputtered particles (second term), with thermionic (third term) for the ions is given – heat flux from ion-ion emission or secondary ion emission (fifth term), the potential of the ion-electron emission (six terms), the kinetic ion-electron emission (seventh term), the characteristic X-ray radiation (eighth term), bremsstrahlung (ninth term), transition radiation (tenth term).

2. Thermophysical processes assigned to the heat flow from the vaporized material (eleventh term), departed from the material in the liquid phase, if the conditions for its release (twelfth term), the thermal radiation of the heated surface (thirteenth term) and condensed atoms, previously steamed (fourteenth term).

3. The plasma-chemical processes, realized due to the reactions of the plasma flow and the flow of ions and spray vaporized target material or adsorbed gases (fifteenth term); This energy is transferred by radiation.

The transfer of energy is also carried out by the radiation flux of ions, electrons or plasma (the last term in Eq. (11)):

$$\begin{aligned}
-\lambda[T]\frac{\partial T(x,y,z,t)}{\partial x} &= F_{i,e} - F_{ev} - F_{m.e} \\
&-\left[F_{ii.e} + F_{i.p.e} + F_{i.e.e} + F_{k.e} + F_{c.re} + F_{thr} + F_{tr}\right]_i \\
&-F_{ev} - F_{m.m} - \sigma\varepsilon T^*(0,y,z,t) \pm F_{cond} + F_{nx} + \sigma\varepsilon_c T_c^*,
\end{aligned} \tag{11}$$

where σ – the Stefan Boltzmann.

To address the issue of effective filling volume nanostructures is necessary to determine the energy charges and ion species in which this condition is satisfied. It should be performed for each of the streams of ions, and it is desirable that the depth ranges where the nanostructures are realized, complement each other. Therefore, such a study is conducted.

5. The study of temperature and rate of rise of temperature depending on the ion energy and charge the different varieties

The study area size, wherein the nanostructure can be formed, allowing the temperature to identify the boundary of the formation of the nanostructure, and the maximum instantaneous temperature in the area.

Analysis Figs. 2-7 shows that an increase in energy and charge the maximum temperature in the area of origin of nanoclusters grow, and reach temperatures of up to 10^6 K, but the duration of these temperatures -10^{-14}, …, 10^{-9} °C during heating and cooling, which does not lead to melting of the material is even. The temperatures at the border of the zone within the formation range of the definition, i.e. near the error of their determination.

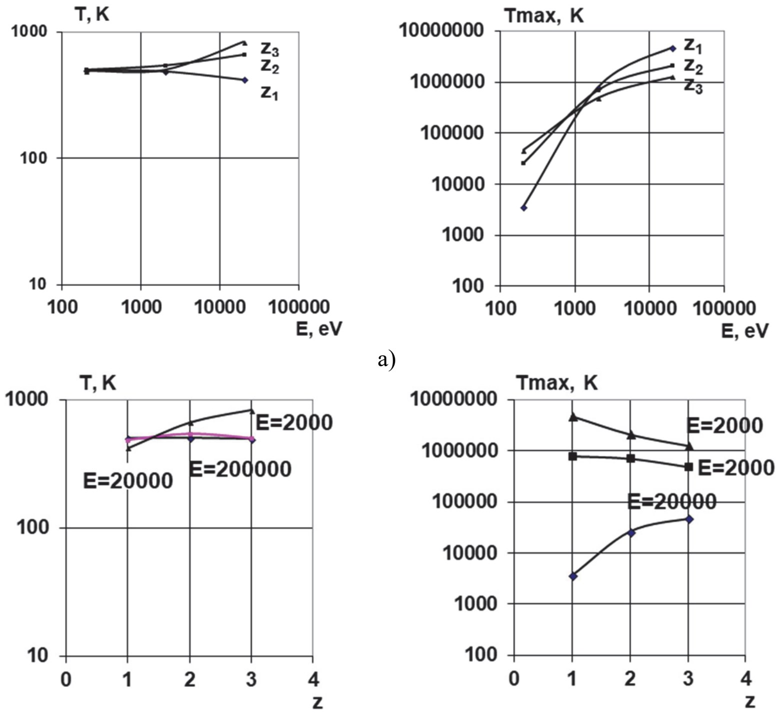

a)

b)

Fig. 2. Plots of T and T the maximum energy from the a) ion charge and b) for the ions C, B, N

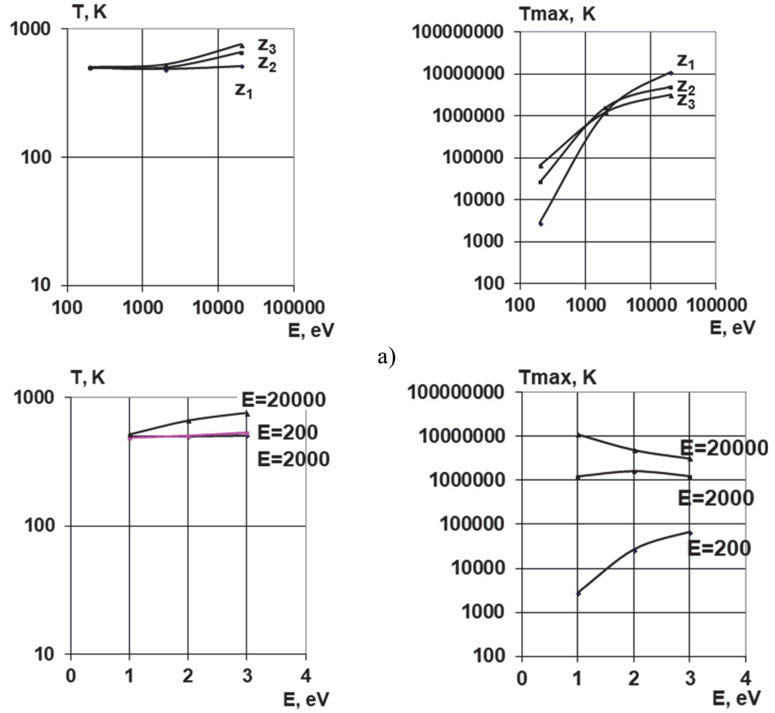

a)

b)

Fig. 3. Plots of T and T the maximum energy from the a) ion charge and b) the ion Al

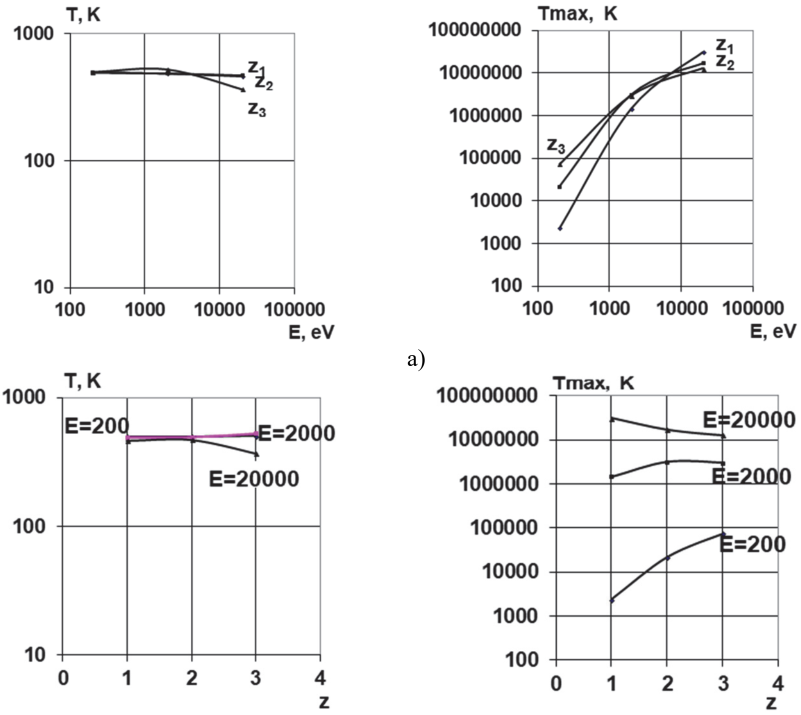

a)

b)

Fig. 4. Plots of *T* and *T* the maximum energy from the a) ion charge and b) for the ions Ti, V, Cr

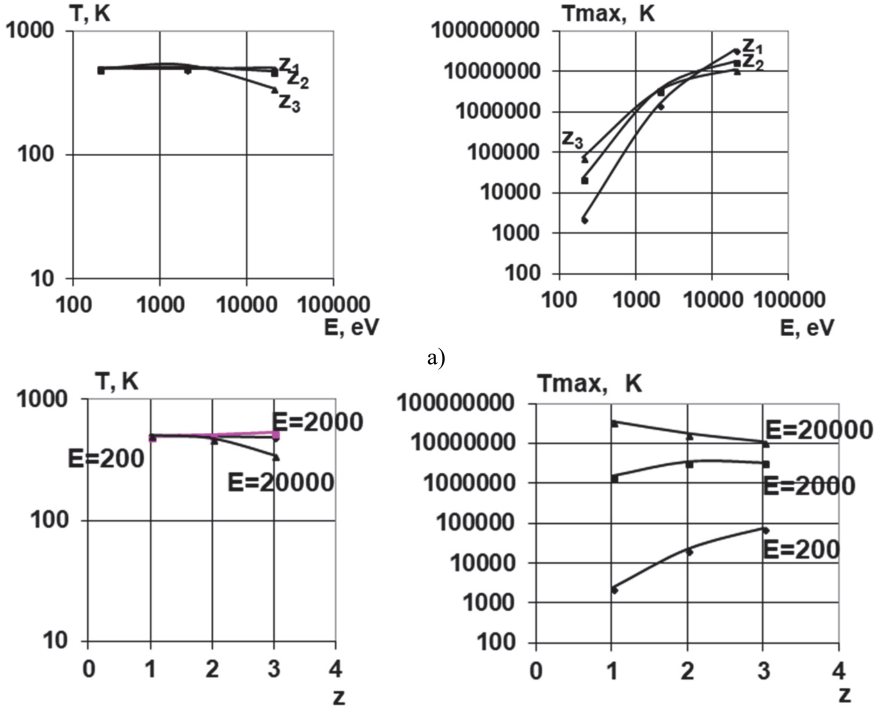

a)

b)

Fig. 5. Plots of *T* and *T* the maximum energy from the a) ion charge and b) for the ions Fe, Ni, Co

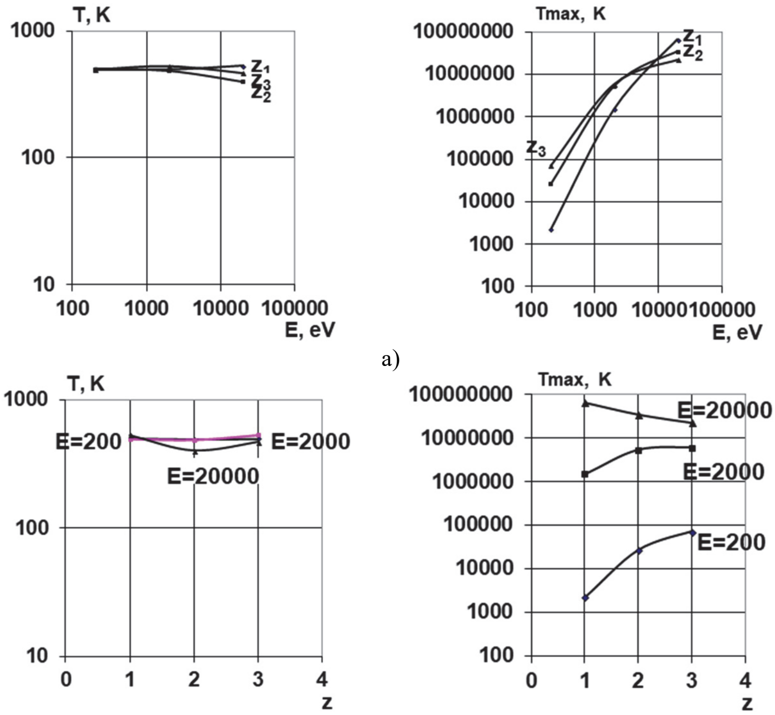

a)

b)

Fig. 6. Plots of *T* and *T* the maximum energy from the a) ion charge and b) for the ions Y, Zr, Nb, Mo

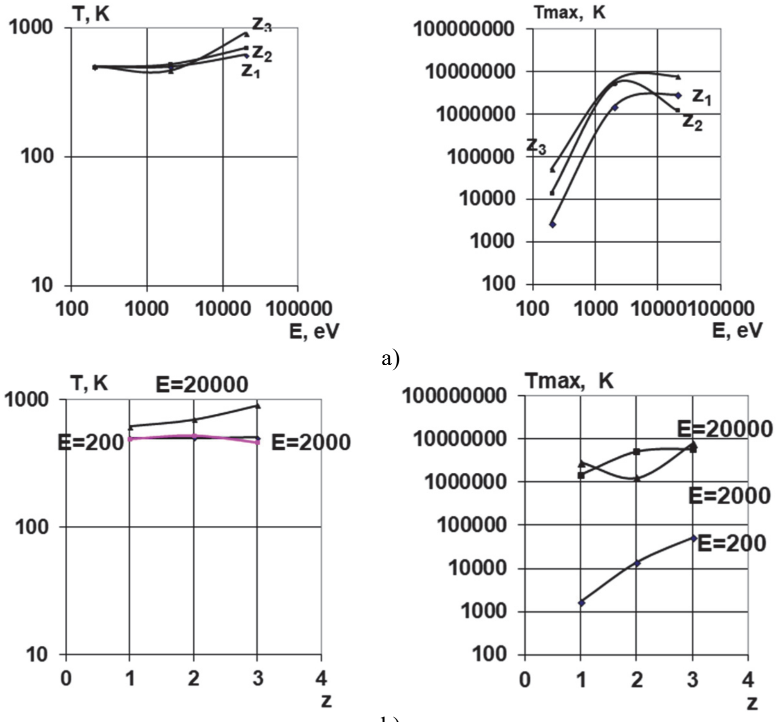

a)

b)

Fig. 7. Plots of *T* and *T* the maximum energy from the a) ion charge and b) ion Hf, Ta, W, Pt

5.1. Research results

The rate of rise in temperature is an important factor in the possibility of forming a nanostructure which is formed at the rate of increase in temperature greater than 10^7 K/s. The calculation results are obtained depending on the rate of rise of temperature on the energy and charge are shown in Figs. 8, 9. It is seen that with increasing energy and charge increases the rate of rise in temperature, ranging from 10^{16} to 10^{18} K/s.

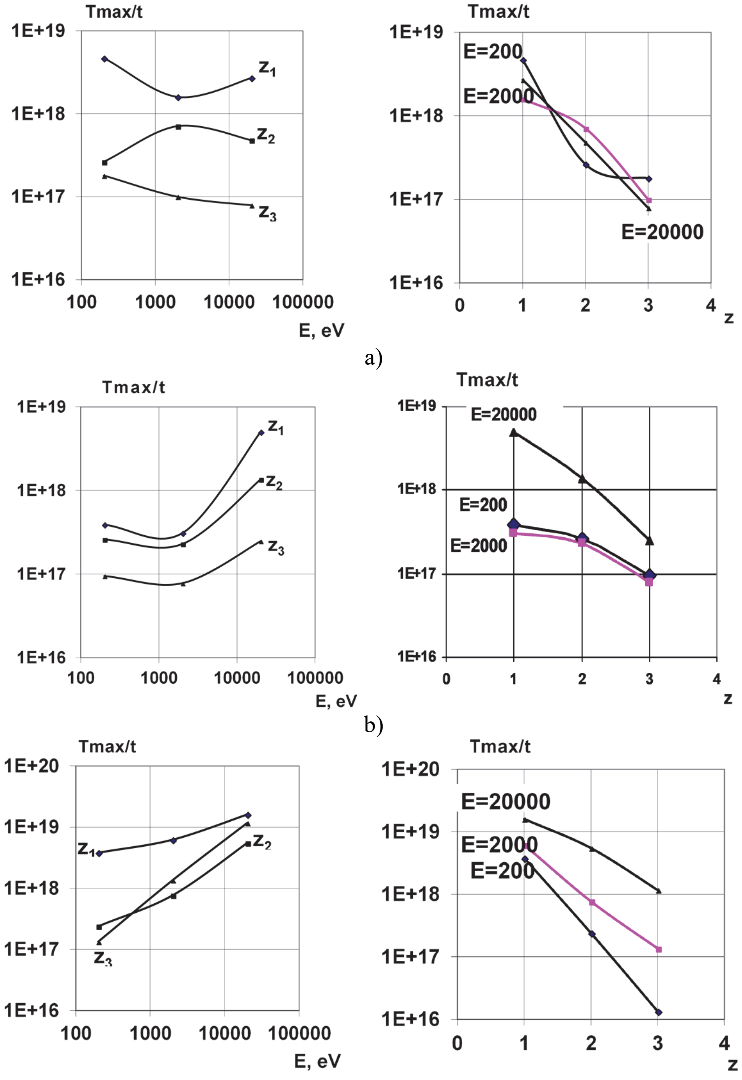

a)

b)

c)

Fig. 8. The graphs of the rate of rise in temperature the energy and charge of ions:
a) C, B, N; b) Al; c) Ti, V, Cr

5.2. Conclusions

The dependence of the maximum temperature of energy and ion charge in steel treatment showed that their growth is increasing the maximum temperature for all investigated types of ions.

Investigation of the temperature dependence of the rate of increase of energy and charge of the ions showed that with increasing energy and charge the rate of rise in temperature increases and reaches the maximum values for ions.

The values obtained for the temperature and rate of rise of temperature confirm the reality of the formation of nanoclusters in filling a number of layers of nanostructures by the simultaneous action of different kinds of ions, energy and charge and receive nanolayer sufficient surface detail.

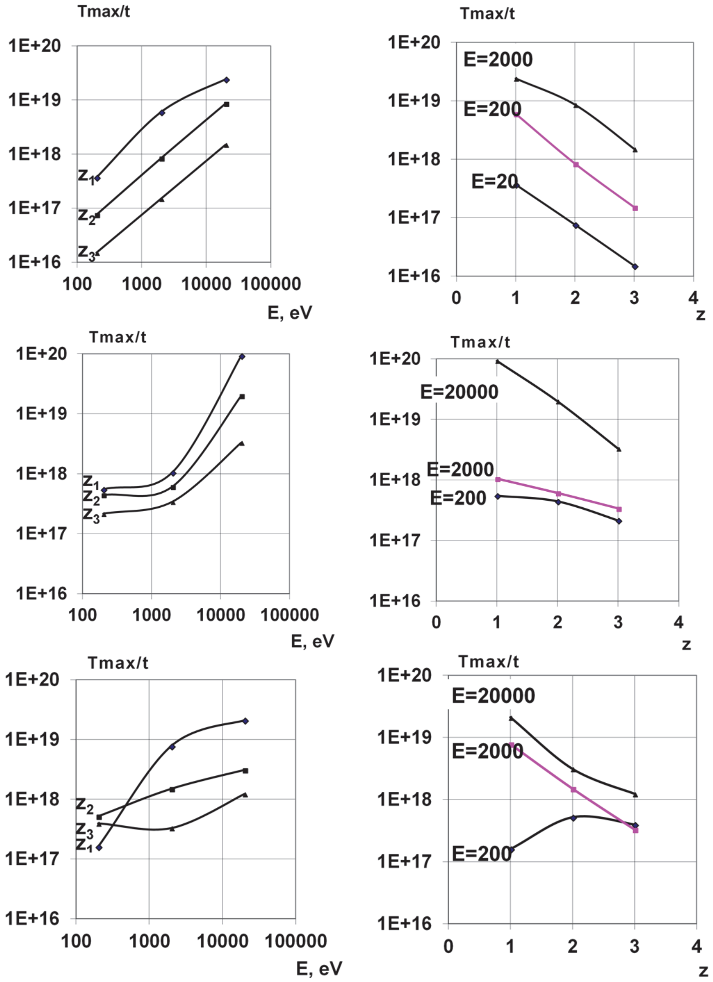

Fig. 9. The graphs of the rate of rise in temperature of energy and charge of the ions:
a) Fe, Ni, Co; b) Y, Zr, Mo; c) Hf, Ta, W, Pt

6. Research quantities of thermal stresses in the zone of ions of various sorts, energy and charge for steel

In addition to the required temperature and rate of rise of temperature important factor is the presence of pressure (thermal stress) in the area of formation of nanostructures. In the first two criteria defined area nanocluster. Conduct a review of the results of calculations of thermal stresses on the boundary of the formation of nanostructures on the first two criteria – σ_{h1} and the maximum value of thermal stress – σ_{h2} under various charges of 1 to 3, Energy – 200, 2000 and 20000 eV (the actual technologies for hardening) ions C, B, N, Al, Ti, V, Cr, Fe, Ni, Co, Y, Zr, Nb, Mo, Hf, Ta, W, Pt.

6.1. Research results

The results of investigations of temperature stresses on the boundary of the formation of nanostructures are shown in Fig. 10 for the ions: a) C, B, N; b) Al; in c) Ti, V, Cr, and Fig. 11 ions: a) Fe, Ni, Co; b) Y, Zr, Nb, Mo, c) Hf, Ta, W, Pt. It is seen that with increasing ion charge and ion energy value of their increased slightly, with the exception of aluminum ions, for which the voltage increases to energy 2000 eV, then decline. The voltages range from 10^6 to 10^8 H/m^2, maximum values are realized for triply charged ions of Hf, Ta, W, Pt and constitute $5{,}85 \cdot 10^8$ H/m^2. The values of thermal stresses on the boundary of the formation of nanostructures even by themselves are not sufficient to produce nanostructures, but together with the action of the other two factors – the temperature and the rate of increase in temperature will significantly accelerate the emergence of nanostructures on the border zone.

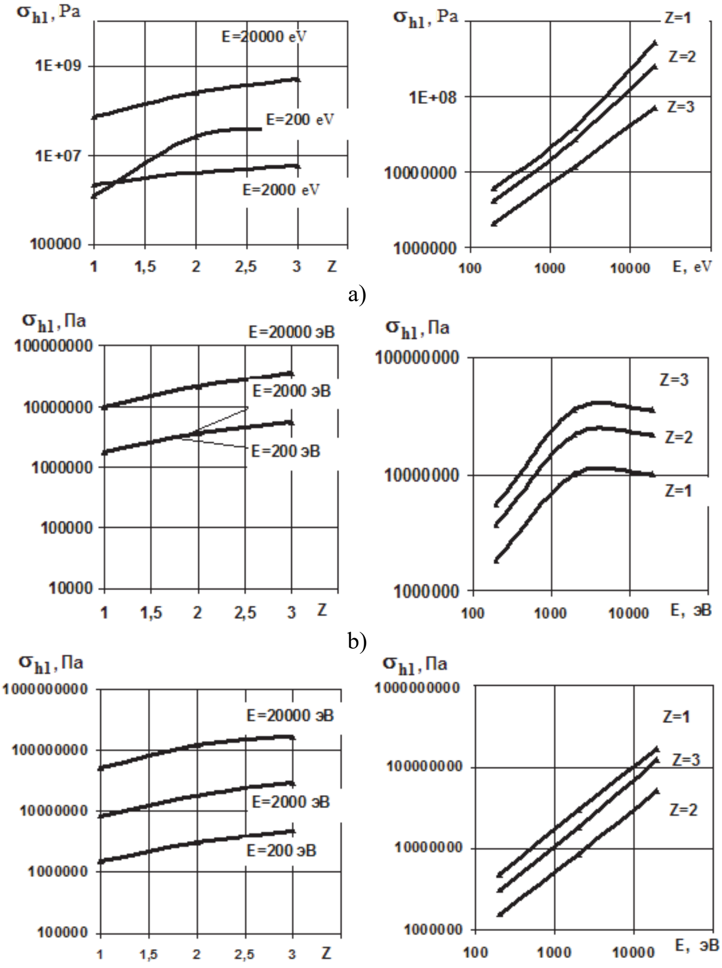

a)

b)

c)

Fig. 10. Plots of the values of thermal stress on the border of nanostructure formation on the charge and energy of the ions: a) C, B, N; b) Al; c) Ti, V, Cr

The findings of maximum thermal stress σ_{h2} in nanoclusters are shown in Fig. 12 ions: a) C, B, N; b) Al; c) Ti, V, Cr and in Fig. 13 for ions: a) Fe, Ni, Co; b) Y, Zr, Nb, Mo, c) Hf, Ta, W, Pt. It can be seen that the magnitude of the stresses increased significantly, about more than an order of magnitude, which, depending on the charge (to an energy of 200 eV) increases, i.e., with increasing charge voltage temperature rise, whereas with increasing energy from $2{\cdot}10^3$ to $2{\cdot}10^4$ eV and increasing the value of the charge of thermal stresses are reduced. Exceptions are ions Hf, Ta, W, Pt, where the energies of 200 eV and 2000, an increase in thermal stress.

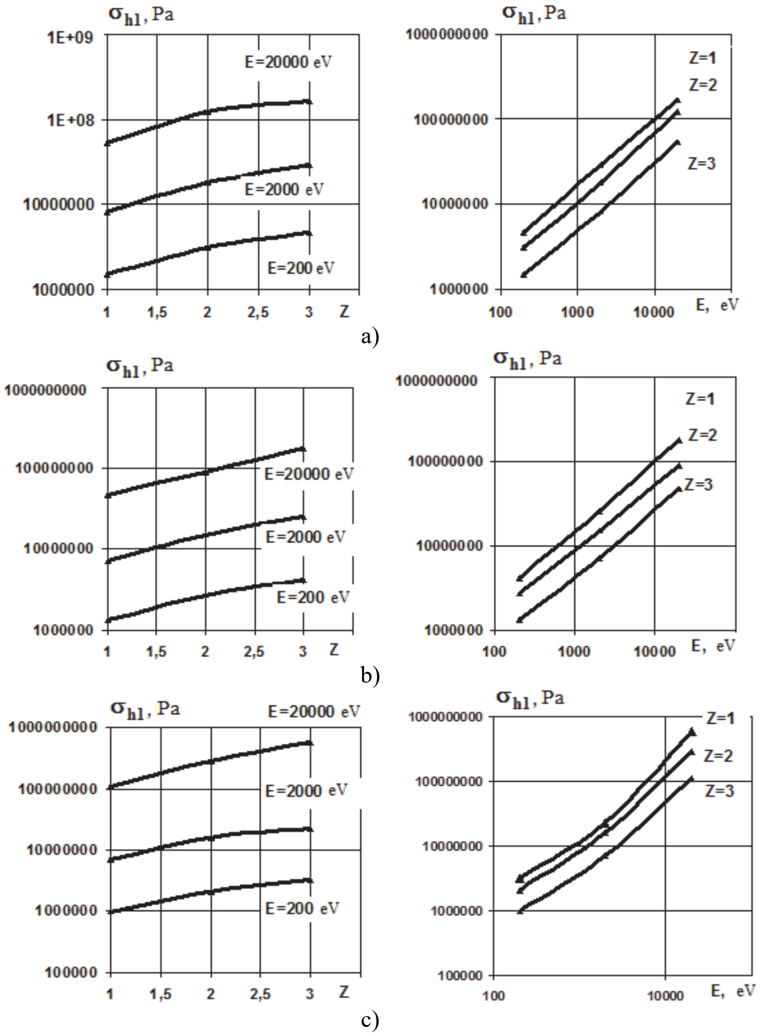

a)

b)

c)

Fig. 11. Plots of the values of thermal stress on the border of nanostructure formation on the charge and energy of the ions: a) Fe, Ni, Co; b) Y, Zr, Mo; c) Hf, Ta, W, Pt

The dependence of the maximum thermal stresses σ_{h2} the energy for almost all of the charges at a maximum ion energy of ions $2{\cdot}10^3$ eV, with the exception of dependence $\sigma_{h2} = f(E_i)$ for singly charged ions of Ti, V, Cr, Fe, Ni, Co, Y, Zr, Mo, where the energy increases the value of thermal stress are increasing, due to the small area of the nanostructure formation (nanocluster).

The values of the maximum thermal stress range from 10^7 to 10^{10} N/m^2, the maximum value of thermal stress is $2.68{\cdot}10^{10}$ N/m^2 for singly charged ions Y, Zr, Mo.

It is seen that the maximum values of temperature and stress mostly do not reach the required pressure value for the formation of nanostructures, but together with the action required temperatures and temperature growth will accelerate or enhance the probability of formation of nanostructures.

Perhaps the emergence of an independent nanostructures by action of singly charged ions Y,

Z_r, M_o $2{\cdot}10^4$ eV of energy when the temperature voltage reaches the necessary pressure for the formation of nanostructures.

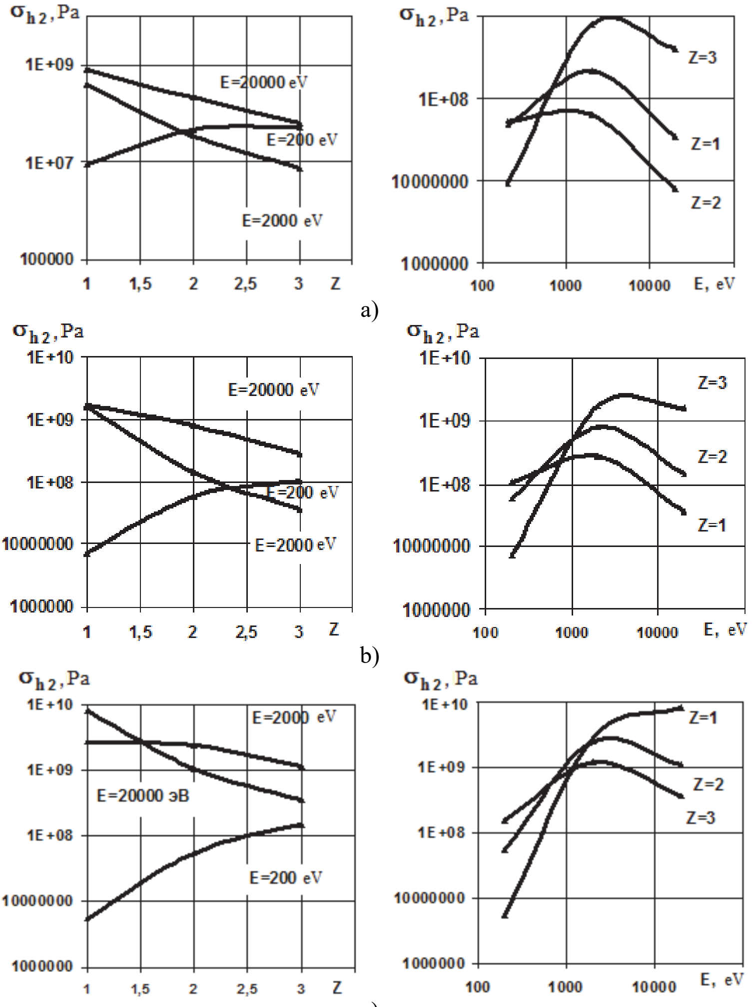

a)

b)

c)

Fig. 12. The graphs of the maximum values of temperature stresses on the charge and energy of the ions: a) C, B, N; b) Al; c) Ti, V, Cr

6.2. Conclusions

1. In the example of processing steel the possibility substantial acceleration of nanostructure formation by the action of thermal stresses on the boundary of the nanocluster and in its entirety.

2. The possibility of formation of nanostructures only by the action of thermal stresses of singly charged ions Y, Zr, Mo at energies eV $2{\cdot}10^4$ when thermal stresses exceed 10^{10} N/m^2.

3. The resulting thermal stresses depending on the zone boundary nanostructure formation and maximum thermal stress on the charge and energy allows for a wide range of ions C, B, N, Al, Ti, V, Cr, Fe, Ni, Co, Y, Zr, Nb, Mo, Hf, Ta, W, Pt in the processing of steel to choose the process conditions and the type of ions to obtain the desired thermal stress, accelerating the formation of nanostructures.

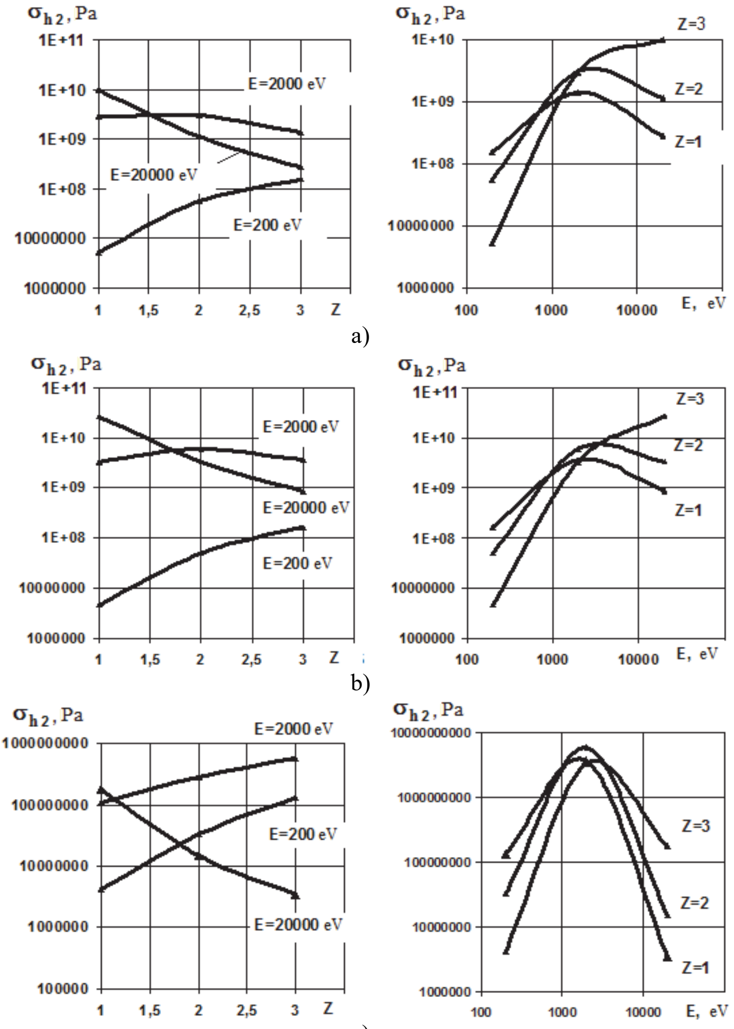

a)

b)

c)

Fig. 13. The graphs of the maximum values of temperature stresses on the charge and energy of the ions: a) Fe, Ni, Co; b) Y, Zr, Mo; c) Hf, Ta, W, Pt

7. Influence of the type of ion, its energy and charge on the grain size and number of particles in nanocluster

The size of the grains of the material defined area where temperatures exceed 500-1500 K, the rate of rise in temperature over 10^7 K/s and pressure values (thermal stress) about 10^7, …, 10^{10} Pa. In the fields of temperature, operating by the end of the thermal action of the ion, it highlights a zone where the temperature exceeded the necessary temperature rise rate for almost all studied types of ions, and the values of thermal stresses are close to or above required for current densities less than or equal to the first critical (for the duration of the heat source particles is observed imposing temperature fields of action of neighboring particles).

Given these criteria formation of nanostructures were obtained depending on the grain size of the ion energy (energy of $2{\cdot}10^2$, $2{\cdot}10^3$ and $2{\cdot}10^4$ eV) at different charge number of ions ($z = 1$, 2 and 3) and the grain size of the ion charge ($z = 1$, 2 and 3) for different ion energies ($2{\cdot}10^2$, $2{\cdot}10^3$ and $2{\cdot}10^4$ eV) ions for the groups that differ little by weight of 1 – P, B, N; 2 – AI; 3 – Ti, V, Cr; 4 – Fe, Ni, Co; 5 – Y, Zr, Mo; 6 – Hf, Ta, W, Pt, which are shown in Figs. 14-25. It is seen that with increasing ion charge the grain size increases for all examined types of ions, but the absolute value decreases during the transition from the lighter ions (N) to heavier (P_t) (Fig. 25).

The increase in grain size with increasing ion charge due to the fact that with increasing ion charge increases mileage and hence the growing zone in which the subject field of temperature and stress, and hence the area where they exceed the criterial value for nanostructures. By increasing the ion energy increases the grain size (cluster) that is also associated with increasing mileage, and hence the size of the area in which it is possible obtaining nanostructures.

Knowing the size of the grains, one can predict the microhardness, tensile strength, friction coefficient, wear resistance and other physical and mechanical performance. For example, in Fig. 26 and 27 are generalized dependence of the microhardness and yield stress of the grain size derived from surveys [12] or from [3, 4]. These values can give a forecast of the microhardness and yield stress. Using the data book [1].

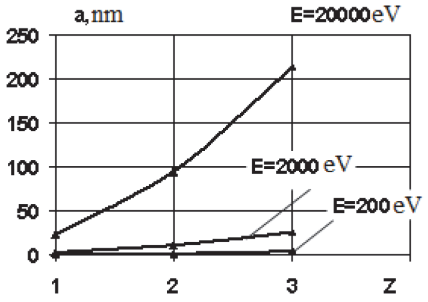

Fig. 14. The plots of the grain size of the ion charge C, B, N at energies $2 \cdot 10^2$, $2 \cdot 10^3$ and $2 \cdot 10^4$ eV

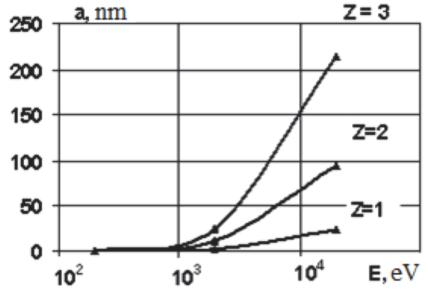

Fig. 15. The plots of the grain size of the ion energy C, B, N at the charges 1, 2 and 3

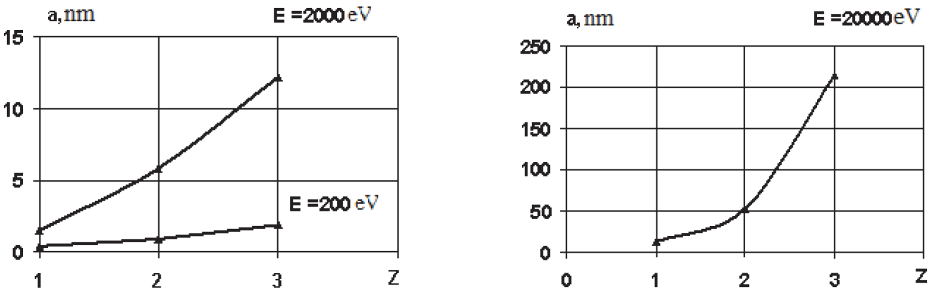

a) b)

Fig. 16. The plots of the grain size of the charge of Al ions at energies a) $2 \cdot 10^2$, $2 \cdot 10^3$ and b) $2 \cdot 10^4$ eV

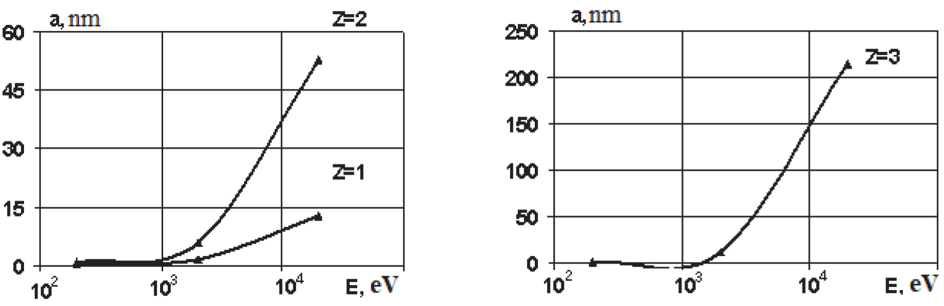

a) b)

Fig. 17. The plots of the grain size of the energy of Al ions when a) charges 1, 2 and b) 3

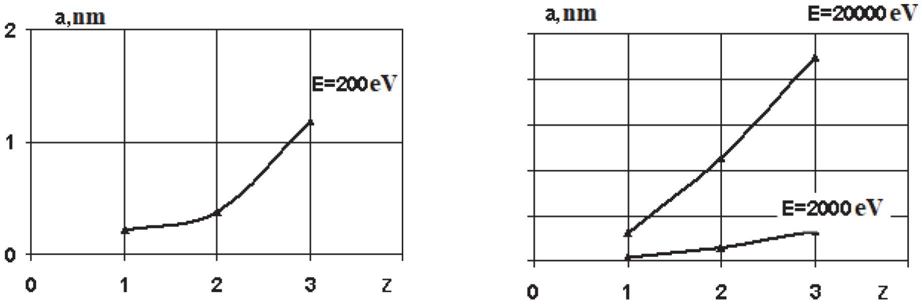

a b

Fig. 18. The plots of the grain size of the charge of the ions Ti, V, Cr at energies a) $2{\cdot}10^2$ eV and b) $2{\cdot}10^3$, $2{\cdot}10^4$ eV

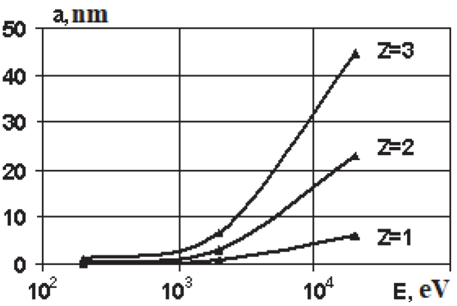

Fig. 19. The plots of the grain size of the ion energy Ti, V, Cr charges at 1, 2 and 3

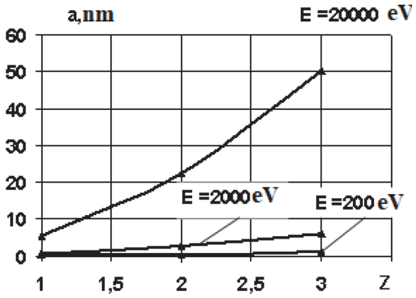

Fig. 20. The plots of the grain size of the charge of the ions Fe, Ni, Co at energies $2{\cdot}10^2$, $2{\cdot}10^3$, $2{\cdot}10^4$ eV

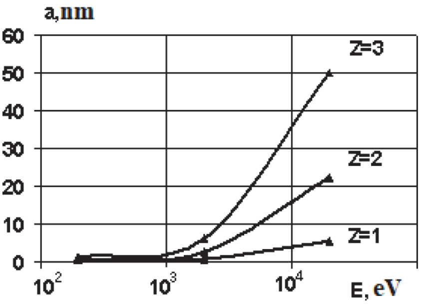

Fig. 21. The plots of the grain size of the energy of the ions Fe, Ni, Co when charging 1, 2 and 3

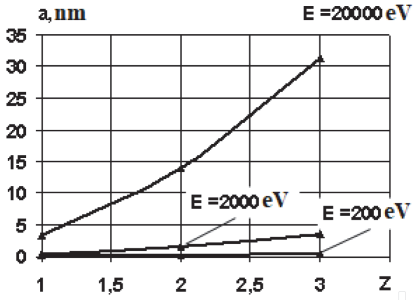

Fig. 22. The plots of the grain size of the charge of the ions Y, Zr, Mo at energies $2{\cdot}10^2$, $2{\cdot}10^3$, $2{\cdot}10^4$ eV

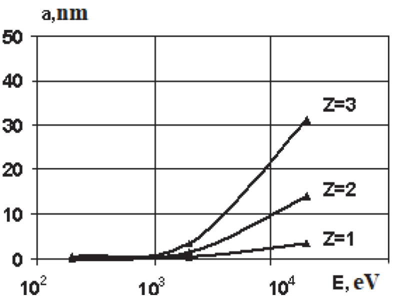

Fig. 23. The plots of the grain size of the energy of the ions Y, Zr, Mo when charging 1.2 and 3

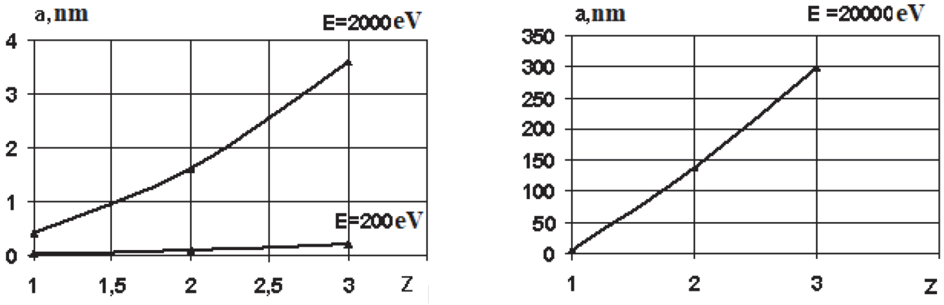

a) b)

Fig. 24. The plots of the grain size of the charge of the ions Hf, Ta, W, Pt at energies a) $2 \cdot 10^2$, $2 \cdot 10^3$ and b) $2 \cdot 10^4$ eV

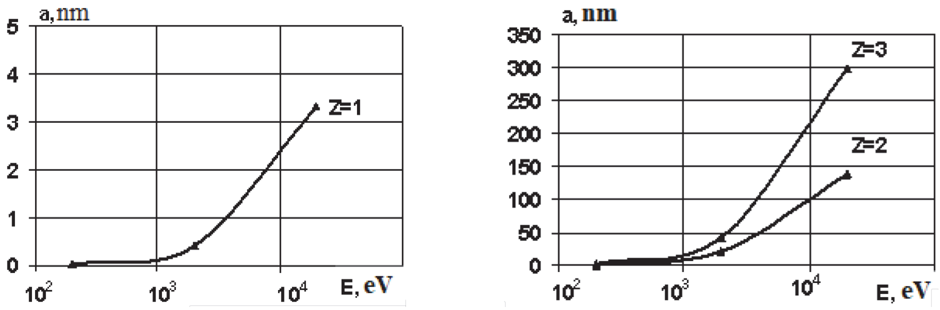

a) b)

Fig. 25. Plots of the grain size of the ion energy Hf, Ta, W, Pt when charges a) 1 and b) 2, 3

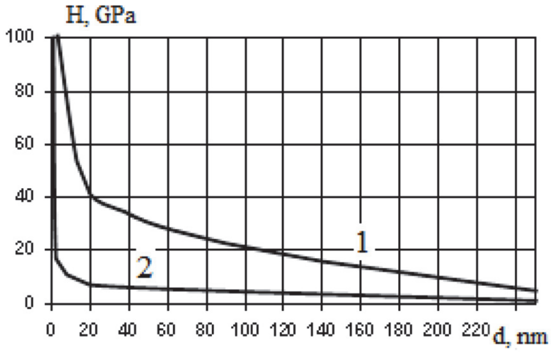

Fig. 26. The results generalize the microhardness grain size: 1 – maximum values; 2 – minimum

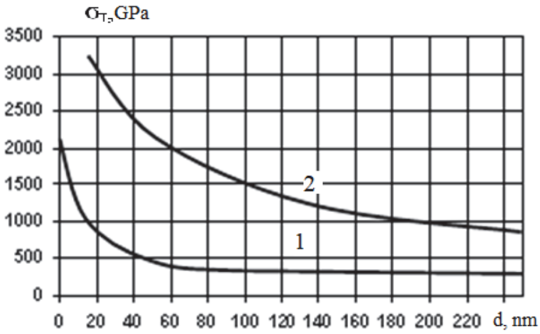

Fig. 27. The results are generalizations based yield strength the grain size of the 1.2

8. Investigation of the effect of the charge and grade ion energy the number of particles in nanocluster

The number of particles in the nanocluster nanocluster determines the possibility of obtaining with the usual bars, when the number of particles greater than 4, or deformed bars nanoscale $n < 4$ (special nanostructures), so this study is necessary.

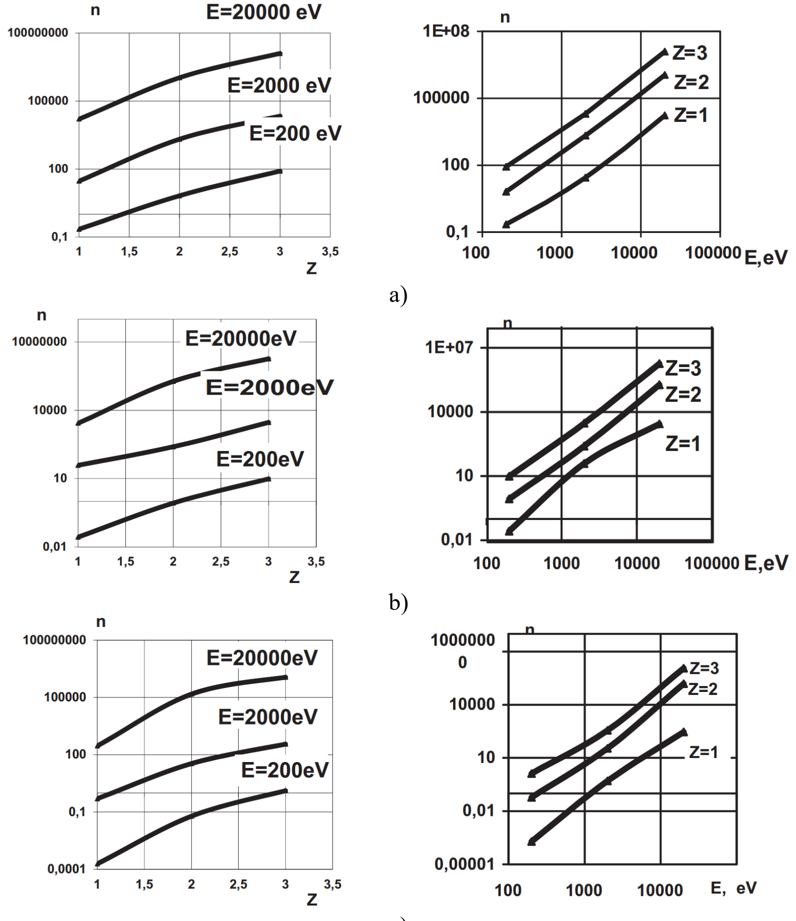

a)

b)

c)

Fig. 28. The graphs of the number of particles in nanoclusters on the charge z, and ion energy Ei ions: a) C, B, N; b) Al; c) Ti, V, Cr

The calculation results of the particles in the cluster, depending on the charge and energy of the ions are shown in Fig. 28, for ions a) C, B, N, b) Al, c) Ti, V, Cr and in Fig. 29 for ions a) Fe, Ni, Co; b) Y, Zr, Mo and c) Hf, Ta, W, Pt. It is seen that with increasing ion charge increases the number of particles in the cluster, which is associated with an increase in area covered by a temperature sufficient to produce the nanostructures. The rate of temperature increase to virtually all ions than necessary – 10^7 K/s, and the values of thermal stress (the required pressure) of the order of from 10^7 to 10^{10} Pa.

It is seen that with increasing mass ions occurs more problematic modes where nanostructures are formed only on the surface with a deformed grain, i.e. major contribution to nanograin give the incident ions at the same time for light ions at energy used in processing plants, it is possible to obtain the nanostructure in the base material parts, at the same time it is possible, for ion energies $2 \cdot 10^4$ eV and lower energies but to charge number 3 (sometimes 2).

All of this suggests the need to estimate the number of particles in a nanocluster.

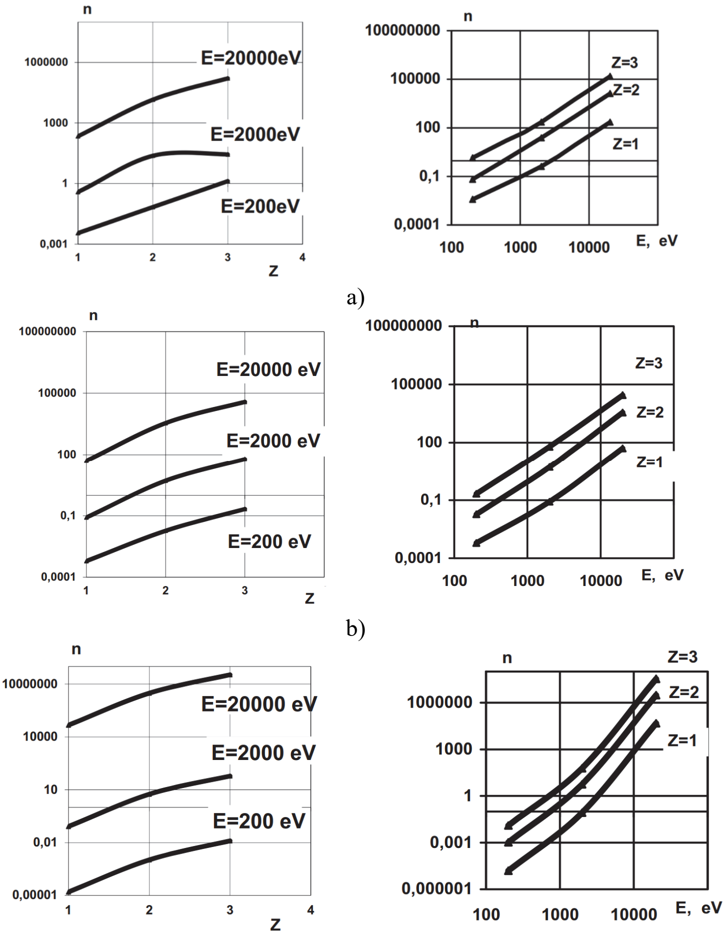

a)

b)

c)

Fig. 29. The graphs of the number of particles in the charge of the nanocluster charge z ion energy and ion Ei: a) Fe, Ni, Co; b) Y, Zr, Mo; c) Hf, Ta, W, Pt

8.1. Conclusions

Revealed power class and the charges of the ions, in which the nanoclusters are implemented and are within the scope of the nanostructure as surface structures, i.e. when the base material is not involved in the details of processing.

Solution of the problem allowed us to find the extent to which conditions can be implemented to produce nanostructures. Therefore, it is possible to determine the actual number of particles that can participate in the creation of volume or flat nanostructures.

9. Effect of the atomic mass of the ion in the grain size and number of particles in nanocluster

Results of the study of influence of the mass of the bombarding ions on the grain size are shown in Fig. 30, and 31, which shows that for low energies 200 and 2000 eV, the charge number 1 and 2 are unlikely to provide the bulk of nanostructures in detail, whereas the energy they produced 2×10^4 eV for all ion masses (Fig. 30(a)) when the charge number 2 has, for the energy of 2000 and 20000 eV actually get the bulk of the nanostructure on the details, whereas at $E_i = 200$ eV may receive only surface nanostructures (Fig. 30(b)) an increase in the number of charge up to 3 leads to an improvement of the situation, but to an energy of 200 eV at ion mass more than 26 amu implemented only the surface of the nanostructure.

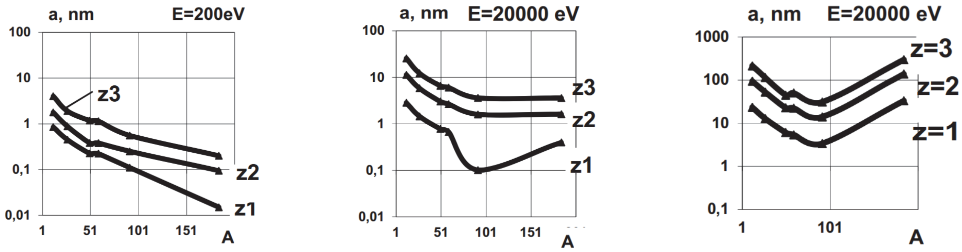

a) b) c)

Fig. 30. The plots of the grain size and the atomic mass of the incoming particles for various charges of ions and energy: a) 200 eV; b) 2000 eV and c) 20000 eV

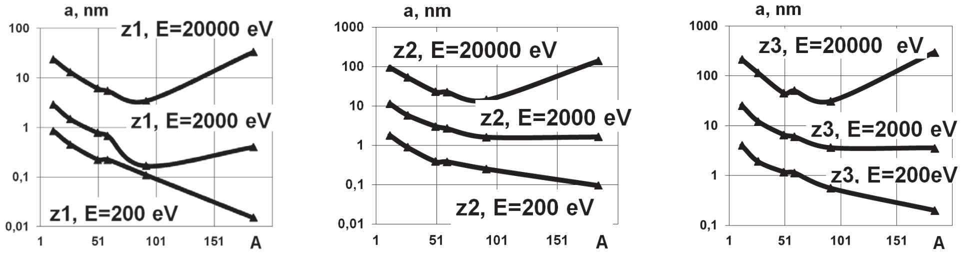

a) b) c)

Fig. 31. The plots of the grain size and the atomic mass of the ion at different energies (200, 2000 and 20000 eV), and the charge of all particles: a) 1; b) 2; c) 3

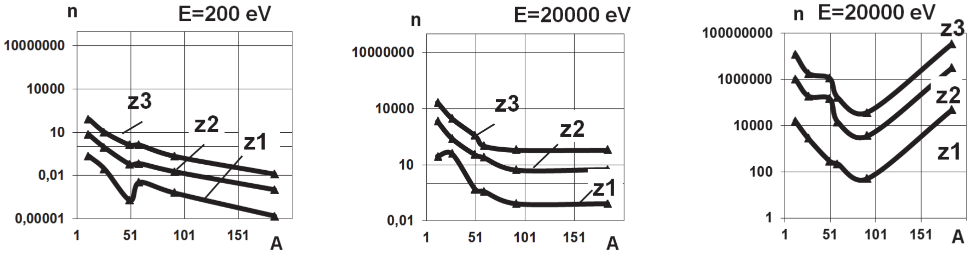

a) b) c)

Fig. 32. The graphs of the number of particles in the cluster n from the atomic mass of the ion A with an ion energy of a) 200 eV, b) 2000 eV, and c) $2{\cdot}10^4$ eV charges for various ions z

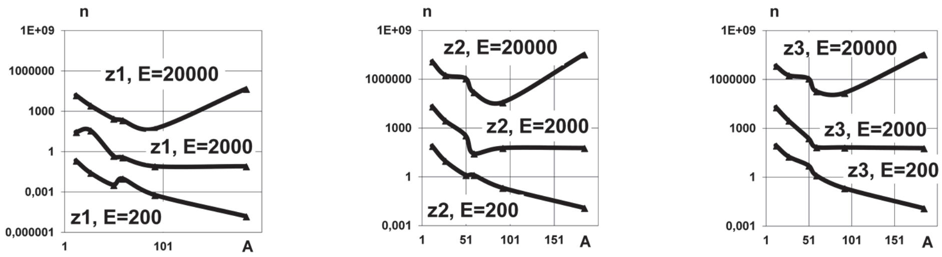

a) b) c)

Fig. 33. The graphs of the number of particles in the cluster from the atomic mass n ion A ions at different energies of the different charges: a) $z = 1$; b) $z = 2$; c) $z = 3$

Analysis of the dependency of the grain size on the ion mass suggests that the nanostructure is obtained or not. So out Fig. 31 and seen that at an energy of 200 eV only if the charge number 3, and then only for a very low-mass ions can obtain a nanostructure in the amount of detail, whereas the energy of 2000 eV can be guaranteed to get nanostructures at atomic number 2 and 3, and the charge number 1 is problematic.

At ion energies $2 \cdot 10^4$ eV for all chargers numbers can be guaranteed to get a real three-dimensional nanostructures.

9.1. Conclusions

The studies allow us to determine the critical values of the atomic mass of the ion, after which it is unlikely to obtain bulk nanostructures.

10. Effect of ion energy, their variety and magnitude of the charge on the volume of nanostructure and determining the effective current density for obtaining nanostructures

The value for a unit volume of na’nostructures ion action allows to predict the required density of the ion current to flow to completely fill the layer where formation of this ion to the corresponding sort, energy and charge.

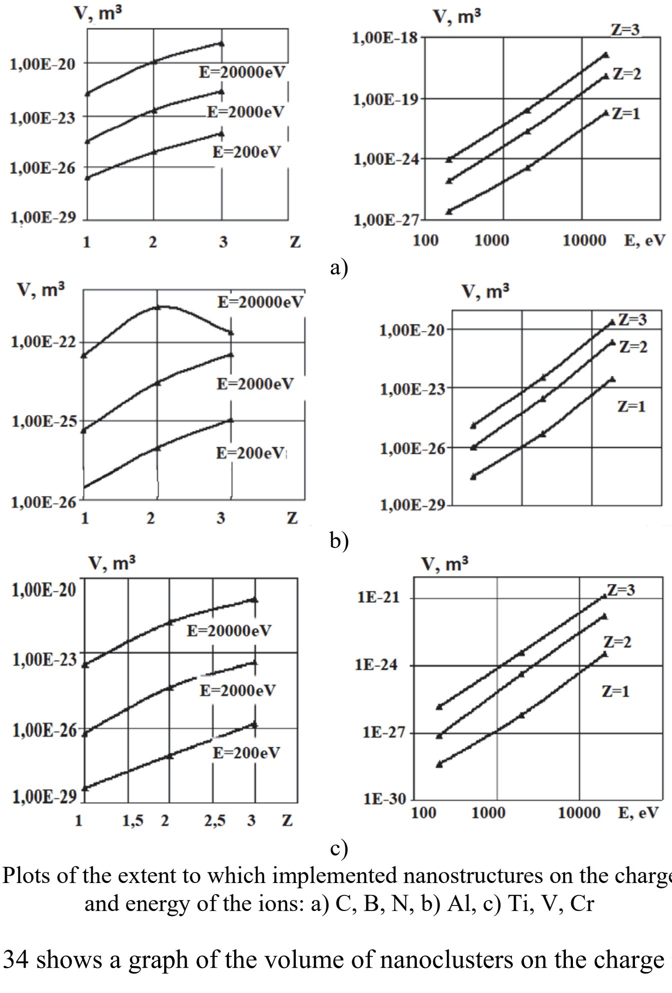

a)

b)

c)

Fig. 34. Plots of the extent to which implemented nanostructures on the charge number and energy of the ions: a) C, B, N, b) Al, c) Ti, V, Cr

Thus, in Fig. 34 shows a graph of the volume of nanoclusters on the charge number *z* and the ion energy E: C, B, N – well; b) Al; a) Ti, V, Cr similar function for the ions Fe, Ni, Co – Fig. 35, and; Y, Zr, Nb, Mo – Fig. 35(b); Hf, Ta, W, Pt – Fig. 35 in. It is seen that with increasing energy of the ions and their charges there is a significant increase in the charge of ions affects less.

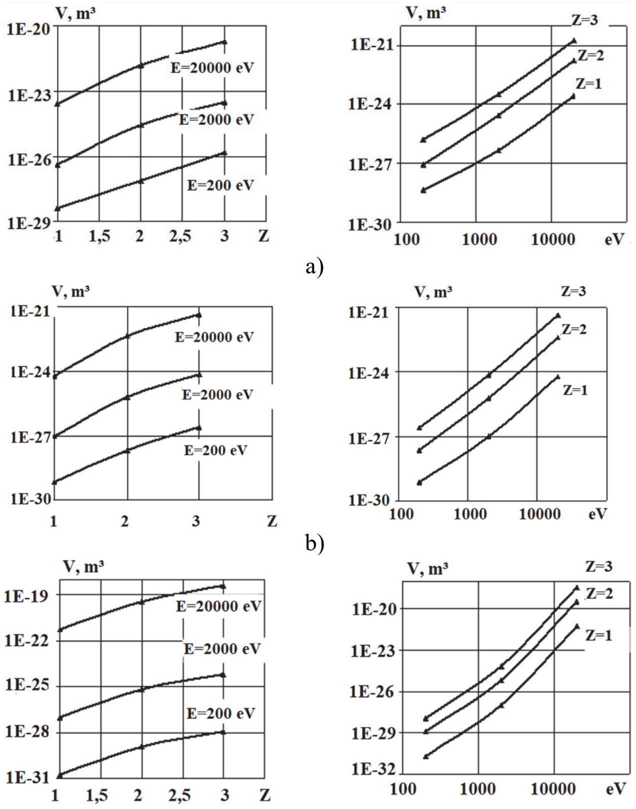

a)

b)

c)

Fig. 35. Plots of the volume of nanostructures on the charge and energy of the ions
a) Fe, Ni, Co, b) Y, Zr, Mo, c) Hf, Ta, W, Pt

These dependencies are required to identify the needs of the current density of the variety, charge and energy to completely fill the layer nanostructures, and selecting appropriate energy charges and the type of ions to produce nanostructures generally required thickness, similarly assesses the current densities required in each layer.

Knowing the volume occupied by the nanostructure in the corresponding energies, grades and charge of the ions and a range of depths at which this volume is obviously possible to estimate the ion current density.

Then the known range of depths of bedding areas, where the image of the nanostructure, select power, variety and ion charge to completely fill the volume of depth, i_e so that they complement each other. Next, determine the current density of each of the varieties of ion charge and to maximize the amount of fill required parts of the surface layer nanostructures (preferably to the end of the first layer was the beginning of the second end of the second the start of the third layer, and so on). Then for each ith layer of the current density is defined as:

$$j_i = \frac{h_{i2} - h_{i1}}{V_{HCi}} z_i e,$$

where h_{i1} and h_{i2} – starting and ending coordinates of the zone where the nanostructures are realized for the ith ion (Figs. 36-41); V_{HCi} – File size area, where the image of the nanostructure; z_i – charge number of ith ion: e – electron charge.

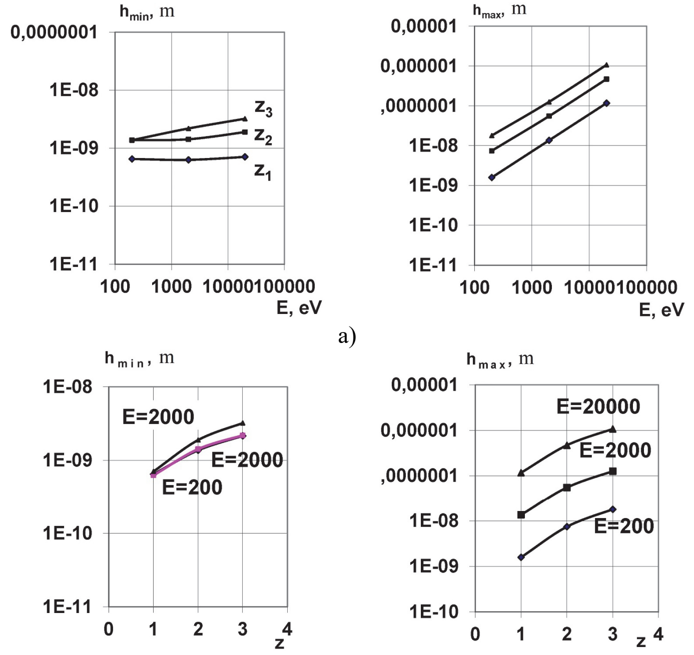

a)

b)

Fig. 36. The graphs of the maximum and minimum $h1$ $h2$ Depth nanolayer obtain the a) energy and b) ion charge (ions C, B, N)

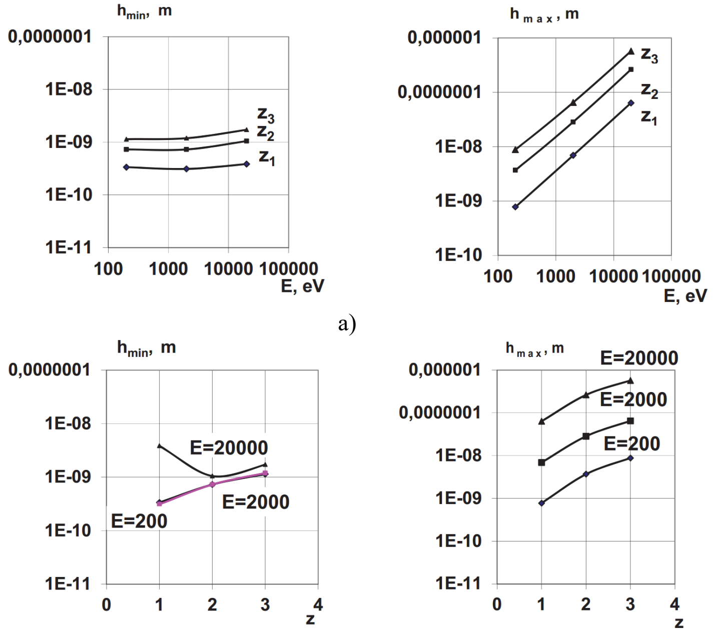

a)

b)

Fig. 37. Graphs of the dependence of the minimum $h1$ and maximum $h2$ of the depth of production of the nanolayer on a) energy and b) ion charge (Al ion)

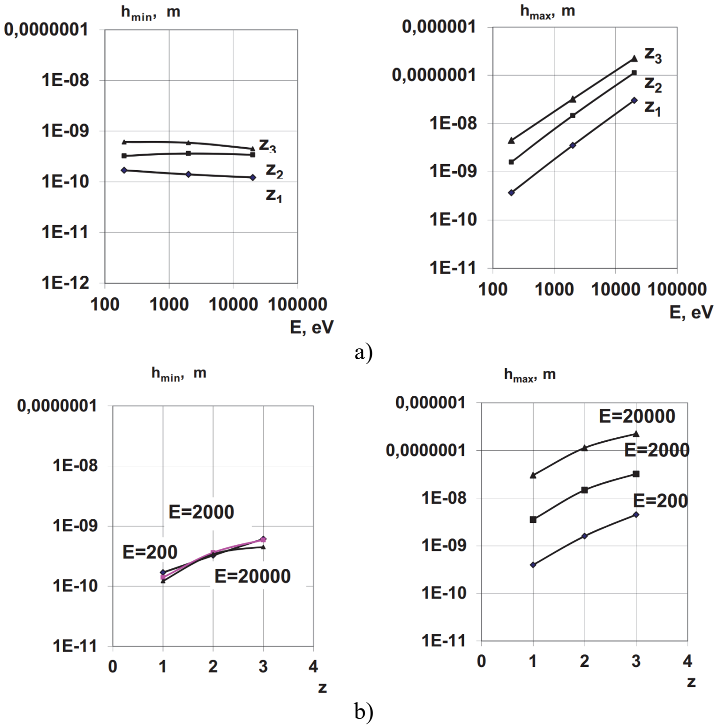

a)

b)

Fig. 38. The graphs of the maximum and minimum $h1$ $h2$ Depth nanolayer obtain the a) energy and b) ion charge (ions Ti, V, Cr)

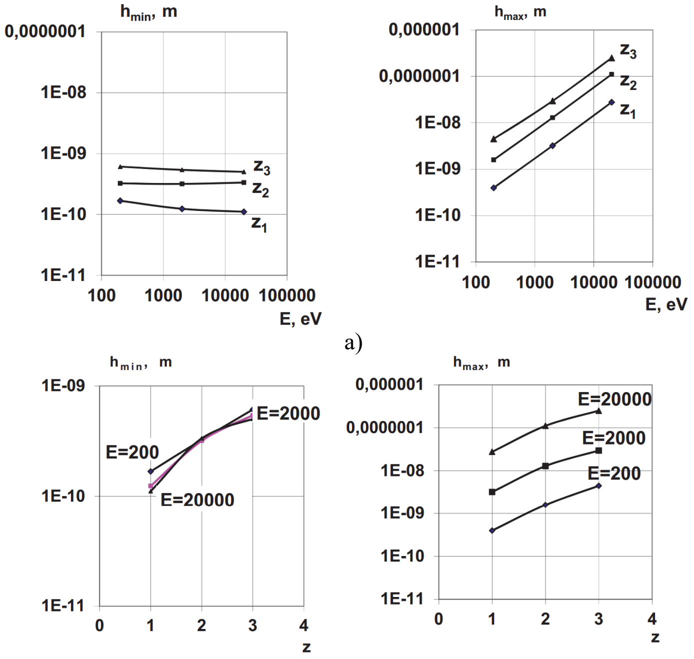

a)

b)

Fig. 39. The graphs of the maximum and minimum $h1$ $h2$ Depth nanolayer obtain the a) energy and b) ion charge (ions Fe, Ni, Co)

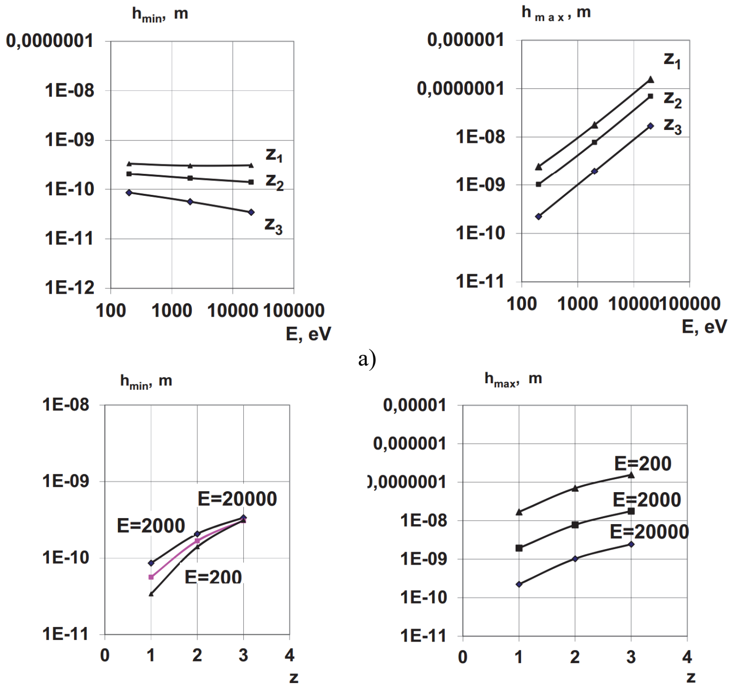

a)

b)

Fig. 40. The graphs of the maximum and minimum $h1$ $h2$ Depth nanolayer obtain the a) energy and b) ion charge (ions Y, Zr, Nb, Mo)

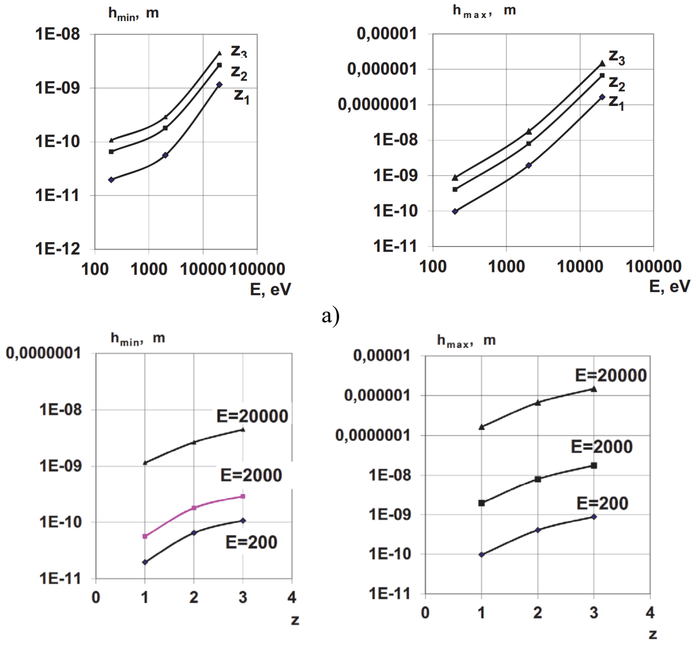

a)

b)

Fig. 41. The graphs of the maximum and minimum $h1$ $h2$ Depth nanolayer obtain the a) energy and b) ion charge (ions Hf, Ta, W, Pt)

Knowing j_i, V_{HCi}, h_{i1}, h_{i2}, E_i, we can create the necessary number of streams of ions that provide a nanostructured layer of the desired thickness, and with the technical task of forming nemonoenergetichnyh raznozaryadovyh ion fluxes can solve the problem of technological parameters of ion treatment.

10.1. Conclusion

On the basis of studies of the effect of energy, variety and ion charge the possibility of obtaining the ion current density at which you can ensure the best possible filling of nanostructures on the layer depth range (minimum and maximum (h_1 and h_2) occurrence of nanostructures.

The possibility of receiving the necessary layers of nanostructures and thickness through the use of ion beams with different energy charge and variety.

Construction of nanostructures using different streams of ions, is provided as follows: the maximum depth of the first layer should be close to the minimum depth of the second layer and so on.

11. Selection of technological parameters of ion fluxes different varieties, energy, charge and current densities for nanostructures

Ensuring nanostructures by controlling the flow of ions simultaneously hit and chargers to the workpiece is carried out under the conditions.

Terms and conditions: both ions hit:

$$\tau_{\max_1}\left[E_{\min_T}, Z_{\min_T}\right] = \tau_2 + \tau_{c3} + \tau_{H2} = \tau_3 + 2\tau_{c3} + \tau_{H3} = \tau_4 + 3\tau_{c3} + \tau_{H4} = \tau_5 + 3\tau_{c3} + \tau_{H5} = \cdots$$

where $E_{\min_T}$, $Z_{\min_T}$ – energy and the charge of the heavy ion; $*(L)$ – distance from the control grid to detail; $\tau_{\max_1}\left[E_{\min_T}, Z_{\min_T}\right]$ – the time of flight of the heavy-ion charger with minimum ($z = 1$) minimum energy; $\tau_2, \tau_3, \tau_4, \tau_5$ – time span the distance L ions of different energies, battery grade and increasing energy and charge; $(\tau_2 > \tau_3 > \tau_4 > \tau_5)$ – composition $E \cdot z$; τ_{c3} – while the interaction of ions with the workpiece; $(\tau_{H2}, \tau_{H3}, \tau_{H4}, \tau_{H5})$ – the launch of the second, third, fourth, fifth ions ($\tau_{H1} = 0$) with respect to the first and determined:

$$\tau_{H2} = \tau_{\max}\left[E_{\min}, E_{\min_T}\right]\tau_2 - \tau_{c3} = \frac{L}{\sqrt{\frac{2E_{\min}}{m_{i_T}} z_{\min}}} - \frac{L}{\sqrt{\frac{2E_2}{m_{i_2}} z_2}} - \tau_{c3}, \tag{12}$$

$$\tau_{H3} = \frac{\mathrm{L}}{\sqrt{\frac{2E_{\min}}{m_{i_T}} z_{\min}}} - \frac{L}{\sqrt{\frac{2E_3}{m_{i_3}} z_3}} - 2\tau_{c3}, \tag{13}$$

$$\tau_{H4} = \frac{\mathrm{L}}{\sqrt{\frac{2E_{\min}}{m_{i_T}} z_{\min}}} - \frac{L}{\sqrt{\frac{2E_4}{m_{i_4}} z_4}} - 3\tau_{c3}, \tag{14}$$

$$\tau_{H_\mathrm{J}} = \frac{\mathrm{L}}{\sqrt{\frac{2E_{\min}}{m_{i_T}} z_{\min}}} - \frac{L}{\sqrt{\frac{2E_j}{m_{i_j}} z_j}} - (j-1)\tau_{cj}. \tag{15}$$

Contact with ions of various sorts, and recharging energy can be arranged simultaneously using one or two of the ion source, pulling ions through the grid by using nanosecond pulse voltage, wherein the first pulse is supplied to the lower amplitude more later, i.e. increasing amplitudes as they are ascending:

$$C'_{ns} = V_{ns}\frac{j}{ez}, \quad S_{l.t}l_{ns} = V_{tr}. \tag{16}$$

$t = \frac{S_{det} \cdot l_{ns} \cdot ez}{V_{ns} \cdot j_i \cdot S_{l.t}}$ – the time of receipt of the nanostructure in a layer l_{ns} on the surface area S_{det}; $j_{i_{c.d}} = \frac{S_{det} \cdot l_{ns} \cdot ez}{t_{l.t} \cdot V_{ns} \cdot S_{pr}}$ – current density required to obtain a limited time for the desired layer l_{ns} the surface area of the details S_{det}; $j_{i_{c.d}} \geq j^I_{cr}$, therefore, the calculations can be taken a current density equal to the first critical.

The action is not mono-energetic ion flux of different varieties and recharging the critical current density for such flows can be obtained as described in [2, 3] or estimated from particle (ion) with the highest mileage (less heavy ion), and large work. Define the first critical current density, assuming that the remaining ions fill the volume between the zones of action of these ions, which is close to the real picture as shown by studies of the distribution of temperature fields and thermal stresses [1].

Then, for the action of the ions of different sorts, energy, charge and current densities while receiving nanostructure layer of the desired thickness can be obtained as:

$$t = \frac{S_{det} \cdot l_{ns}}{\left(\sum V_{ns}\frac{j^I_{cr}}{ez_i}\right) \cdot S_{pr}}, \tag{17}$$

or in the case can be used to simplify the expression:

$$t = \frac{S_{det} \cdot l_{ns} \cdot ez_{m.m}}{V_{ns} \cdot k_{as} \cdot j^I_{cr_{m.m}}},$$

where $z_{m.m}$ and $j^I_{cr_{m.m}}$ – the first charge and the critical current density of the ions with the maximum mileage, k_{as} = 1.2-2 to increase the filling ratio by volume of particles with smaller runs and, more important factor corresponds to a greater number of additional streams of ions. Examples of calculation of the duty ratio of volume and temperature fields, thermal stresses are presented in [8] for the different laws of distribution of the ions in space parts of various laws (spiral of Archimedes, cellular location and uniform rectangular arrangement of the particles).

Organization of simultaneous ingress of ions of different sorts of energy and recharging the surface of the parts is carried out under the conditions.

Contact with ions of various sorts, energy and recharging at the same time can be organized using one or two of the ion source, pulling them through the grid by using nanostructured voltage pulses. And the first pulse is applied to the lower amplitude, and later with large amplitudes with increasing.

11.1. Conclusions

The analysis allows to find treatment regimens in which is possible to obtain nanostructures.

The possibility of the simultaneous implementation of the end of the thermal springs of action-particles, which improve the quality of treatment.

References

[1] **Kostyuk G. I.** Nanotechnology: Theory, Experiment, Technology, Perspectives. Academy of Sciences and Innovation, 2012, p. 648.

[2] **Kostyuk G. I.** Physical and Technical Principles of Coating, Ion Implantation and Ion Doping, Laser Processing and Hardening, Combined Technologies. Book 1: Physical Processes of Plasma-Ion, Ion-Beam, Plasma, Light-Beam and Combined Technologies. Publishing House of AIU, 2002, p. 596.

[3] **Kostyuk G. I.** Physical and Technical Principles of Coating, Ion Implantation and Ion Doping, Laser Processing and Hardening, Combined Technologies. Book 2: Handbook for Calculating the Basic Physical and Technological Parameters, Assessing the Possibilities, Choosing the Type of Technology and Equipment. Publishing House of the AAS, 2002, p. 482.

[4] **Kostyuk G. I.** Nanostructures and Nanocoatings: Perspectives and Reality. University of Kharkov, 2009, p. 406.

[5] **Kostyuk G. I.** Scientific Foundations of the Creation of Modern Technologies. University of Kharkov, 2008, p. 552.

[6] **Kostyuk G. I.** Effective Cutting Tool with a Coating and a Reinforced Layer. University of Kharkov, 2007, p. 633.

[7] **Kostyuk G. I.** Effective Cutting Tool with a Coating and a Reinforced Layer. View of AINU, 2003, p. 412.

[8] **Kostyuk G. I.** Physicotechnical Foundations of Robot Production. University of Kharkov, 2006, p. 614.

[9] **Grechikhin L. I.** Physics of Nanoparticles and Nanotechnologies. Technoprint, 2004, p. 397.

[10] **Schneider P.** Engineering Problems of Heat Conduction. Izd-vo Inostr. Lit., Moscow, 1960, p. 488.

[11] **Aksenov I. I.** Vacuum Arc in Erosion Sources of Plasma. Publishing House of the Scientific Research Institute “KIPT”, 2005, p. 211.

[12] **Hayakawa S.** Nuclear-physical Aspect. Mir, Moscow, 1973, p. 701, (in 2 Books).

[13] **Gott Yu. V.** Interaction of Particles with Matter in Plasma Studie. Atomizdat, Moscow, 1978, p. 271.

[14] **Gusev A. I.** Nanocrystalline Materials: Methods of Obtaining and Properties. Publishing House of the Russian Academy of Sciences, Ural Division, Ekaterinburg, 1998, p. 302.

[15] **Gusev A. I.** Nanomaterials of Nanostructure, Nanotechnology. Fizmatlit, Moscow, 2005, p. 416.

[16] **Reshetnyak E. N.** Synthesis of hardening nanostructured coatings. Questions of Atomic Science and Technology, Vol. 2, 2008, p. 119-130.

[17] **Andrievsky R. A.** Nanomaterials: the concept and modern problems. Physics of Metals and Metallography, Vol. 91, Issue 1, 2003, p. 50-56.

[18] **Goncharov A. A., Ignatenko P. I., Petukhov V. V., et al.** Composition, structure and properties of nanostructured tantalum boride films. Zhurnal Tekhnicheskoĭ Fiziki, Vol. 76, Issue 10, 2006, p. 87-90.

Kostyuk Gennady Igorevich Professor of the Department of Theoretical Mechanics, Machine Science and Robot Mechanics Systems of the National Aerospace University. N. E. Zhukovsky “KhAI”, vice-president of the International Academy of Sciences and Innovative Technologies. Doctor of Technical Sciences, Professor, Academician of the Academy of Engineering Sciences and the Academy of Sciences of Technological Cybernetics of Ukraine. The scientific heritage of G. I. Kostyuk counts 1070 scientific works (including 210 works in the far abroad), 8 of them are monographs, 32 textbooks and textbooks, 12 patents for inventions and 13 copyright certificates. Under his leadership is protected 4 doctoral and 25 master’s theses.

4.2. Prediction of the physical and mechanical characteristics, the removable material volume for the durability period, cutting tools durability and processing productivity depending on the grain size of the coating or cutting tool base material

Gennadiy Kostyuk
National Aerospace University named by N. Ye. Zhukovsky, KhAI, Kharkov, Ukraine
E-mail: *gennadiykostyuk206@gmail.com*

Abstract. The microhardness and yield strength decrease with grain size increasing for wide range of the 0.2HfN + 0.8ZrN coated materials (K40, Sandvik Koromant, MS221) was disclosed. Two-layer Al_2O_3 + (0.2HfN + 0.8ZrN) coated Sandvik Koromant plate microhardness changes slightly (due to the fact that almost always nanostructures implemented) with the grain growth 33.7-63.8 nm, H_μ = 16.08-17.14 GPa. The coating effective application criterion will condition: the coating grain size should be less than the cutting tool base material grain size. Maximum microhardness is realized at the TiN concentrations in diborides from 50 to 80 % and grain sizes range from 5 to 13 nm. It is proved that modulus of elasticity increases with the grain size growth. It is shown that at the effectiveness and efficiency assessing of the coated hard alloys at the K19195 hardened materials and G10450 steel processing it is necessary to take into account the coating grain size at that to the smaller grain size is generally (but not always) corresponds to more effective processing (the maximum removable material volume for the durability period) and its working capacity. For G10450 steel effective processing can be used 0.18HfN + 0.82ZrN coated Sandvik Koromant company solid alloy, MS221 and K40, which will be both effective and operable. It found that at the cast iron processing the coating adhesive interaction with the manufacturable material is an important characteristic which provide unique value of removable volume for durability period of the (1.3-1.8) 10^7 mm^3 order. The maximum durability (19,000-14,000 sec) also realized in this case, maximum productivity is realized at the minimum G and T values. Performed investigations allow to predict the removable material volume over the durability period, cutting tool durability and processing productivity depending on the coating grain size. It is important to select the cutting tool coating and processing mode.

Keywords: cutting tools, microhardness, nanostructures, nanotechnologies.

1. Introduction

The experimental results presented in the previous parts showed that the grain size of the coating or the main cutting tool material affects on the physical-mechanical characteristics of the material cutting tools, its efficiency and productivity. Experiment results summary from the more than 500 references showed the following.

The grain size effect on the physical-mechanical and electrical properties of the materials were studied in [1-3]. The microhardness maximum presence, depending on the grain size (Figs. 1-5) was found in [1-3]. Weak grain size influence on the microhardness in magnetron nitride nanocomposites nc-TiN/αSi_3N_4 at the different annealing temperatures is observed in [2], whereas for vacuum-arc nanocomposites maximum microhardness realized for certain grain sizes (Fig. 5).

In [4-8] were obtained high microhardness values up to 45 GPa for 0.8ZrN + 0.2HfN coating at the combine processing, increased cutting tools wear resistance and durability up to 20 times, and at the only 0.8ZrN + 0.2HfN coating deposition the microhardness was about 35 GPa, which is more than twice higher than the individual components microhardness. All this allows to suppose that nanostructures appearance is realized even at the only coating deposition while additional electron-beam modification will provide more effective nanostructures with improved properties and in the considerable depth (0.1 mm).

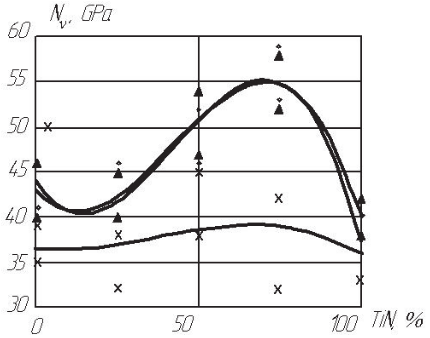

Fig. 1. The coating microhardness dependence on the TiN percentage composition in the TiB2 + TiN coating (crystal size 3-10.2 nm) [2]

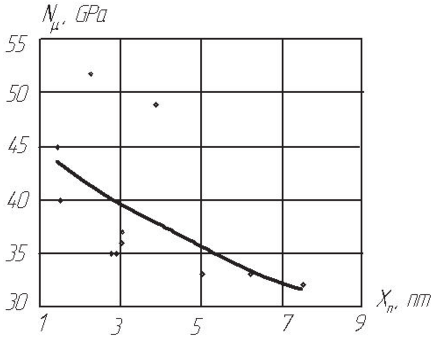

Fig. 2. The coating microhardness depending on the crystal size [1]

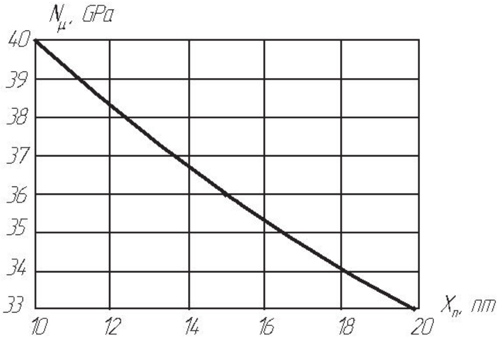

Fig. 3. The coating microhardness dependence on the grain size according to [3]

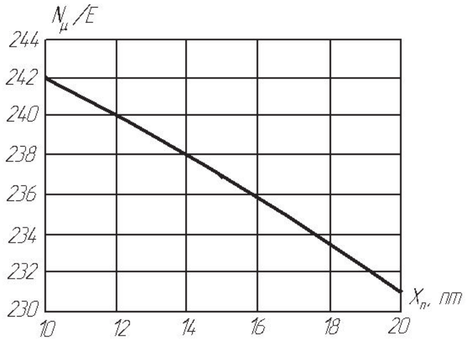

Fig. 4. The coating microhardness dependence on the grain size according to [3]

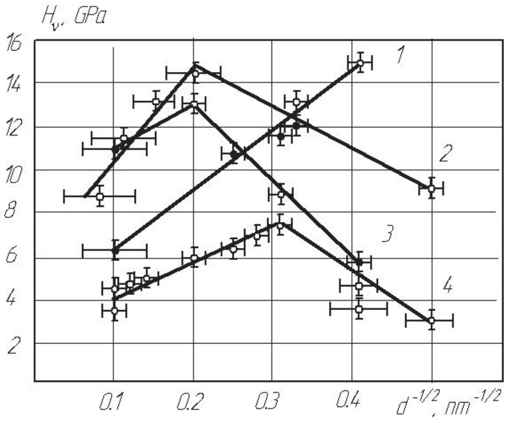

Fig. 5. The coating microhardness H_v dependence on the grain size of the dispersed phase, released in nanocrystalline alloys obtained by amorphous alloys crystallization:
1 – $Fe_{73.5}Cu_1Nb_3Si_{13.5}B_9$; 2 – $Fe_{81}Si_7B_{12}$; 3 – $Fe_5Co_{70}Si_{15}B_{10}$; 4 – $Pd_{81}Cu_7Si_{12}$ [4]

The grains size knowledge enables to predict the microhardness, yield strength, friction coefficient, wear resistance and other physical-mechanical and operational characteristics. For example, generalized microhardness and yield stress dependences on the size from the Fig. 7 and 6 are obtained from reviews [2] or papers [4-8]. The microhardness and yield strength data forecast can be performed on these values or at the monograph [8] using.

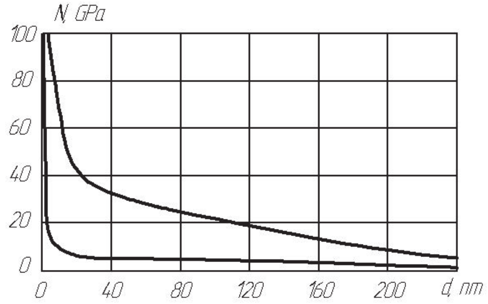

Fig. 6. The generalization results of the microhardness dependence on the grain size: top – maximum values; bottom – minimum values

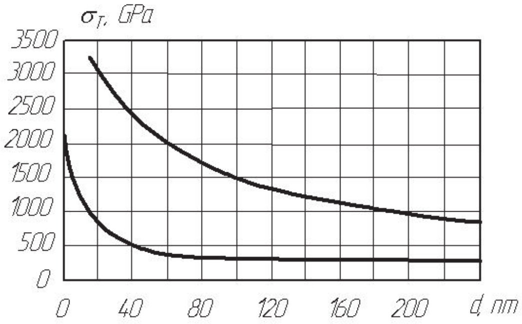

Fig. 7. The generalization results of the yield strength dependence on the grain size according to [9]

The most important nanotechnology mission is the required physical and mechanical characteristics obtaining on the cutting tools and details surface layers coating and directly in the cutting tools and details surface layer. Theoretical prediction of the physical and mechanical characteristics is not yet fully possible due to the complexity and diversity of the processes involved in the certain physical and mechanical characteristics formation. In this case it is possible with a reliability high degree to determine theoretically the grain size, and in future, using the experimental dependence of certain physical and mechanical characteristics on the grain size, to estimate its values for the given technological and physical parameters. Using such dependencies or extrapolate these dependencies relationships for other materials or modes, we can predict with reasonable accuracy the process parameters that provide the necessary characteristics.

2. Microhardness prediction in dependence on the grain size in the 0.2HfN + 0.8ZrN single-layer coating hard alloy cutting tool

Microhardness of the 0.2HfN + 0.8ZrN coated hard alloys cutting tools is measured on the PMT-3 microdurometer: the average value was selected from five measurements. The grain size was measured by the REM-106 electron microscope for 0.2HfN + 0. coating 8ZrN on plates made of VK-8 hard alloy (production of the USSR), Sandvik Koromant (H13 plate) and a bilayer coated Sandvik Koromant: Al_2O_3 (front surface layer) and 0.2HfN + 0.8ZrN (layer directly on the plate front surface, plate side surfaces and cutting tool back surface) (Fig. 8).

The 0.2HfN + 0.8ZrN coated MS 221 hard alloy plates (production of the Russia) and coated and uncoated Sandvik Koromant (H13) plates were investigated also.

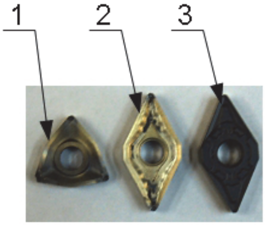

Fig. 8. Appearance plates: 1 – VK8; 2 – 0.2HfN + 0.8ZrN coated Sandvik Koromant (H13); 3 – two-layer coated Al_2O_3 + 0.2HfN + 0.8ZrN Sandvik Koromant

The most characteristic parts of the cutting tool coating surface are shown on the Figs. 9-13; the sizes of the typical grains for the coating each type are also given. It can be seen that the minimum grain sizes were realized on the two-layer coating Al_2O_3 + 0.2HfN + 0.8ZrN (33, …, 63 nm) (Fig. 9).

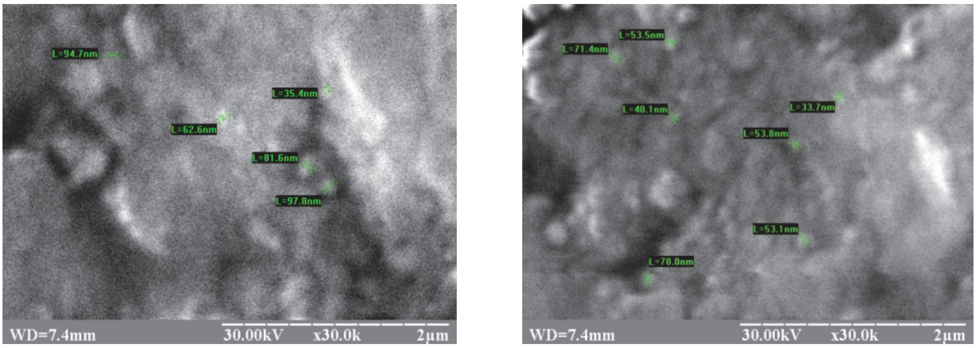

a) b)

Fig. 9. The micrograph of the surface Al_2O_3 + 0.2HfN + 0.8ZrN coating on the Sandvik Koromant hard alloy obtained by the electron microscope (Cu coating was used to reduce the charge effect on the Al_2O_3) for the front surface different zones: a) near the top; b) in the middle part of the plate front surface

Relatively low grain size in the 0.2HfN + 0.8ZrN coating is realized on the VK8 hard alloy plates; its value is in 84, …, 119 nm range, i.e. were realized both nanostructures $\alpha \leq 100$ nm) and submicrostructure with grain sizes range from 100 to 119 nm (Fig. 10(a, b)).

Photo of the 0.2HfN + 0.8ZrN coating fracture enables to estimate its thickness which in the wearing zone of the coating is ≈ 1, ..., 2 microns, whereas in the non-intensive wear zone it is close to the original value of 10 microns order (Fig. 10(c)).

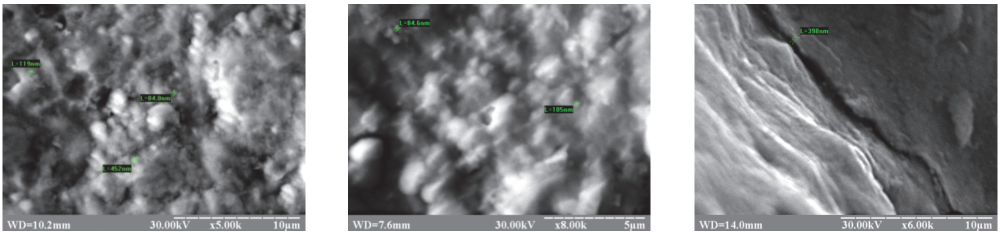

a) b) c)

Fig. 10. Photomicrographs of the 0.2HfN + 0.8ZrN coated VK8 plates: a) near the top; b) in the plate 4 middle; c) near the coating fracture zone

For the hard alloy Sandvik Koromant (H13) plates with 0.2HfN + 0.8ZrN coating grain sizes is from 84 to 200 nm, where the submicrostructure grain size 100 to 200 nm prevails, but there are a significant number of the nanoclusters grain size from 84 to 100 nm (Fig. 11).

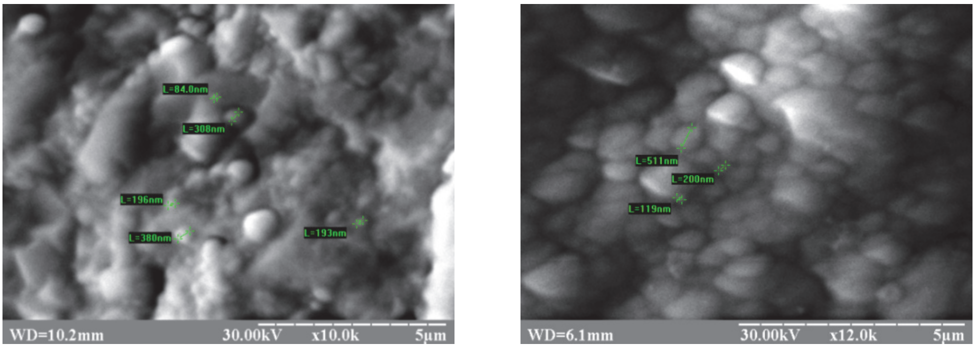

a) b)

Fig. 11. Photomicrographs of the 0.2HfN + 0.8ZrN coated Sandvik Koromant plates: a) near the top; b) in the middle part of the plate front surface

Photos of the MS221 hard alloy coating are shown in Fig. 12. Obviously that grain size is in the range from 36.5 to 105 nm, the grains part with size of 100, ..., 105 nm is very small, the grains vast majority has size from 36 to 58 nm, i.e. practically all coating is nanostructured.

Photos of the uncoated Sandvik Koromant hard alloy are shown in Fig. 13. Obviously that grain size is in the range from 35.6 to 115 nm, the grains significant amount has size from 40 to 88 nm, i.e. nanostructures are realized in the sufficiently large portion of the plate volume.

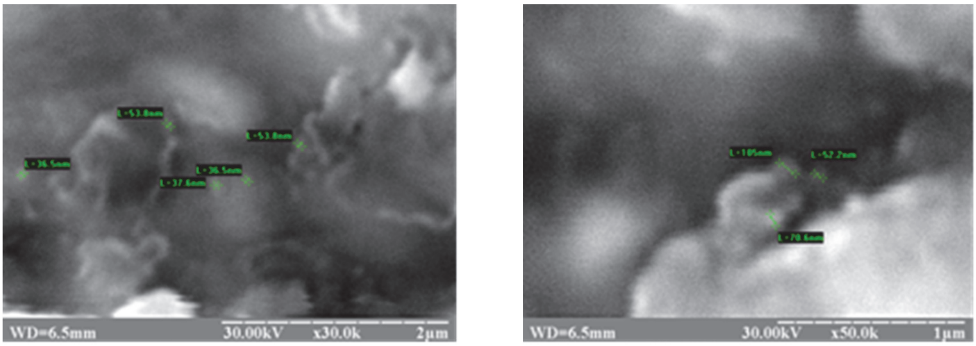

a) b)

Fig. 12. Photomicrograph of the 0.2HfN + 0.8ZrN coatingon the MS221 hard alloy

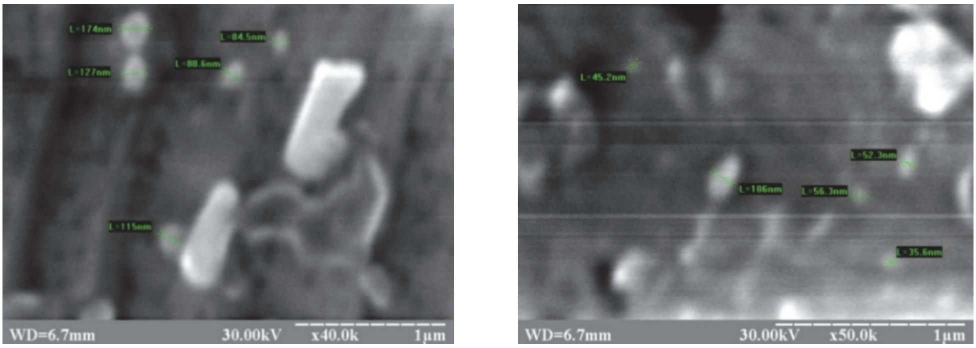

a) b)

Fig. 13. Photomicrograph of the uncoated Sandvik Koromant (H13) hard alloy Photomicrograph of the uncoated Sandvik Koromant (H13) hard alloy

All the above suggests that it is really to receive nanostructures not only in the coating but also in the base material of the cutting tool.

These coated plates microhardness dependence on the grain size are shown in Fig. 14, where microhardness decrease at the grain size increasing. VK8 plates (production of the USSR) are characterized by the highest microhardness, but at the same time they are characterized by the fastest microhardness value decline to 14.67 GPa ($\alpha = 119$ nm). For 0.2HfN + 0.8ZrN coated Sandvik Koromant plate microhardness decrease to the almost the same value (14 GPa) at the 200 nm grain size. For two-layer coating Al_2O_3 + 0.2HfN + 0.8ZrN Sandvik Koromant plates microhardness varies within small range 16.08-17.14 GPa for grain size variation between 33.7, ..., 63.8 nm, i.e. almost always nanostructures are realized.

For coated MS221 cutting tools microhardness is 22.28 GPa at the grain size of 36 nm; microhardness reduces with grain size increasing and with for grain size of 105 nm microhardness becomes equal 16.08 GPa (Fig. 14, curve 5).

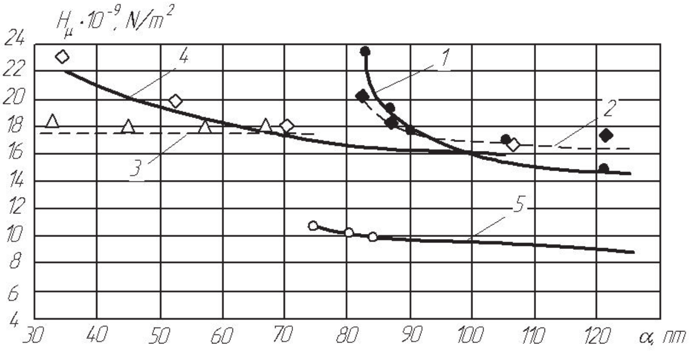

Fig. 14. The microhardness dependence on the grain size for coating: 1 – 0.2HfN + 0.8ZrN on the K40; 2 – on the Sandvik Koromant (H13 plates); 3 – for the Al_2O_3 + 0.2HfN + 0.8ZrN two-layer coating on the Sandvik Koromant; 4 – 0.2HfN + 0.8ZrN coating on the MS221; 5 – for the uncoated Sandvik Koromant (H13)

Microhardness changes relatively slightly on the grain size of the uncoated Sandvik Koromant plates (see Fig. 14). It can be seen that the grain size variation from 36 to 176 nm reduces microhardness from 8.9 to 10.42 GPa.

Also, the Sandvik Koromant hard alloy microhardness small change shows the sufficiently high isotropic structure, and hence the of the plate manufacturing quality technology (see Fig. 14, curve 5).

The similar microhardness dependences on the grain size for the 0.18HfN + 0.82ZrN coating on the T15K6 plate are shown in Fig. 15 (grain size was considered as average statistical, measured by the REM-106, microhardness was measured by the PMT-3 instrument).

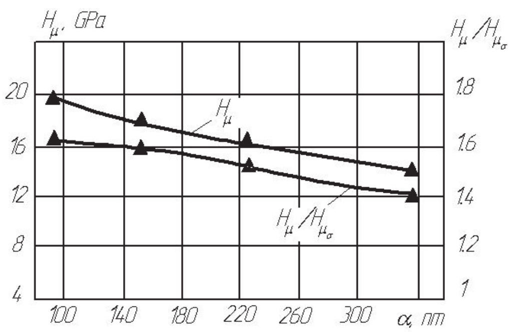

Fig. 15. 0.18HfN + 0.82ZrN coated P40 plate microhardness H_{μ_n} and relative microhardness dependence on the grain size a, nm

It can be seen that at the grain size increasing the coating microhardness is reduced, but still remain larger than microhardness of the hafnium or zirconium nitrides. The microhardness relative change (coated cutting tool with respect to the uncoated cutting tool) on grain size is shown in Fig. 15. It is seen that the microhardness maximum increase is realized for the nanostructured coatings case.

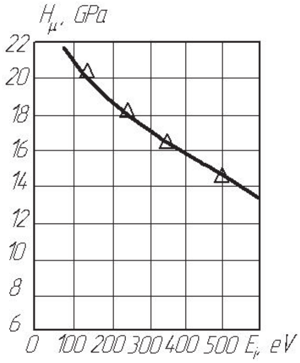

Fig. 16. The microhardness dependence on the ion energy

As result of the nanostructures realization only for one mode at the 110 eV ion energy (Fig. 16), it is not possible to expect effective work of the T15K6 cutting tool.

All this confirms the thesis that the nanostructures significantly increase the microhardness.

From the preceding it follows that for the effective coatings use such condition is necessary: the coating grain size should be less than in the cutting tool base material, and preferably nanostructure realization.

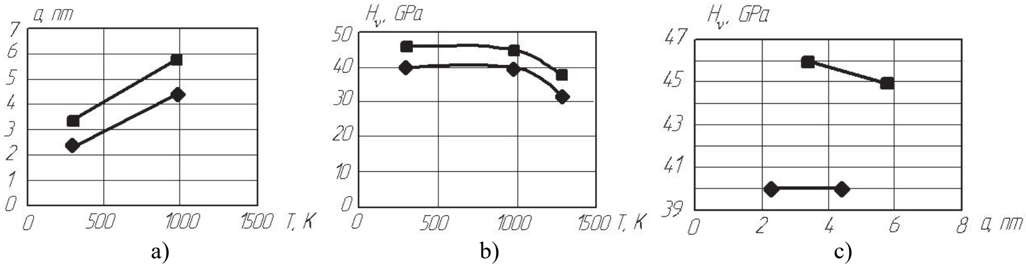

a) b) c)

Fig. 17. Dependence of the a) grain size and b) microhardness on the temperature,
c) microhardness dependence on the grain size (■ – maximum value, ◆ – minimum value)
for $TiB_2 + 0.25TiN$ nanostructure

On the study basis [2] annealing temperature influence on the grain size and microhardness and the microhardness dependence on the crystallite size were analyzed (Fig. 17) for diboride. Investigations of the samples with the obtained in the experiment maximum and minimum microhardness were conducted. These curves analysis shows that the grain size is in the range 2.3, ..., 19.6 nm, at that for many diborides grain size maximum values depend on the temperature.

The maximum microhardness values are realized at the temperatures close to normal $T = 273$ K, at the temperature increase to 1000 K, microhardness values reduced insignificantly, while the further temperature increase significantly reduces the microhardness from 46 to 32 GPa ($TiB_2 + 0.25TiN$), Fig. 17.

For $TiB_2 + 0.5TiN$ coating the maximum grain size value increases at the temperature growth and minimum size value has maximum; grain size is in the range from 2.7 to 5.5 nm. The maximum microhardness value are realized at the temperature close to 1000 K, microhardness decreases at the further temperature increase. The microhardness is also reduced with the grain size growth (Fig. 18).

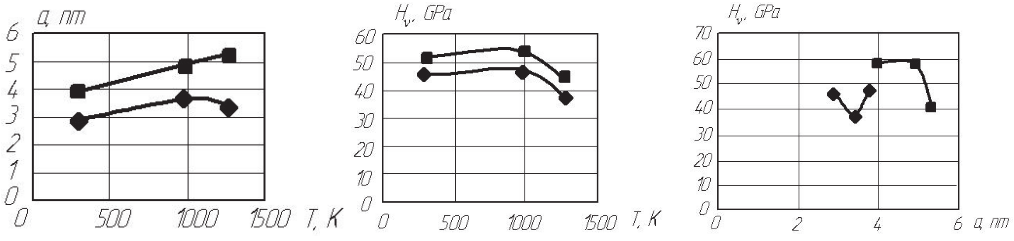

a) b) c)

Fig. 18. Dependence of a) the grain size and b) microhardness on the temperature, c) microhardness dependence on the grain size (■ – maximum value, ◆ – minimum value) for TiB_2 +0.5TiN nanostructure

Diboride TiB_2 + 0.75TiN research showed that at the temperature growth to 1000 K, the grain size increases significantly, then the grain growth is slowing. Microhardness decreases slightly in the range temperature up to 1000 K and later it decreases considerably. The microhardness dependence on the grain size allows to predict it in dependence on the diboride grain size (Fig. 19).

Similar studies of the titanium nitride (TiN) showed that it behaves much the same way, but the grain size is slightly higher and reaches above 20 nm, which is realized at the temperature of 1000 K (Fig. 20(a)). The maximum microhardness is also realized at the temperature of 1000 K. At the further temperature growth microhardness also reduced, though not as fast as for diborides (Fig. 20(b)). The microhardness dependence on the grain size allows to predict the microhardness value on the grain size.

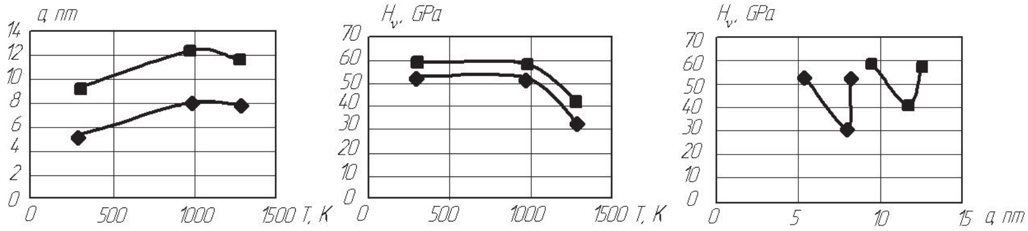

a) b) c)

Fig. 19. Dependence of a) the grain size and b) microhardness on the temperature, c) microhardness dependence on the grain size (■ – maximum value, ◆ – minimum value) for TiB_2 + 0.75TiN nanostructure

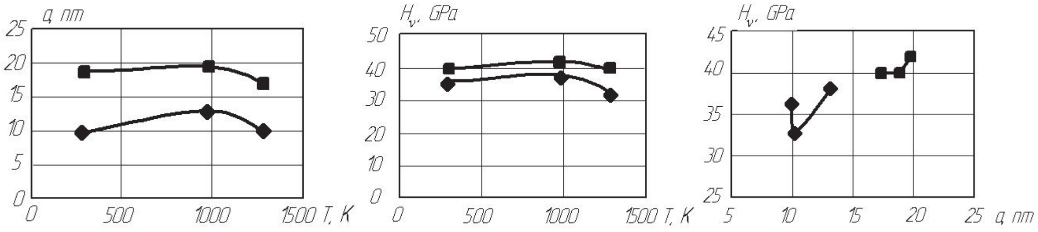

a) b) c)

Fig. 20. Dependence of a) the grain size and b) microhardness on the temperature, c) microhardness dependence on the grain size (■ – maximum value, ◆ – minimum value) for TiN nanostructure

The microhardness dependences on the temperature were obtained for TiB_2, maximum microhardness value is realized at the temperature close to 1000 K. Later the temperature decreases (Fig. 21).

The grain size and microhardness as a function of the TiN percentage (Fig. 22(a), (b)) and the microhardness dependence on the coating grain size (Fig. 22(c)) were also studied. It is seen that at the TiN concentration growth the grain size increases up to 18 nm (maximum size) and 10 nm (minimum size). The maximum microhardness is realized at the near 77 % TiN concentration. The microhardness dependence on the grain size (Fig. 22(c)) shows that the maximum its value is realized at the about 10 nm grain size at $T = 273$ K.

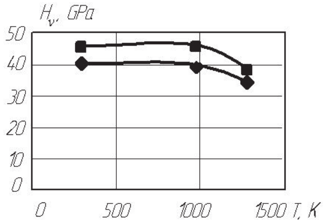

Fig. 21. Dependence of the microhardness on the temperature
(■ – maximum value, ◆ – minimum value) for TiB_2 nanostructure

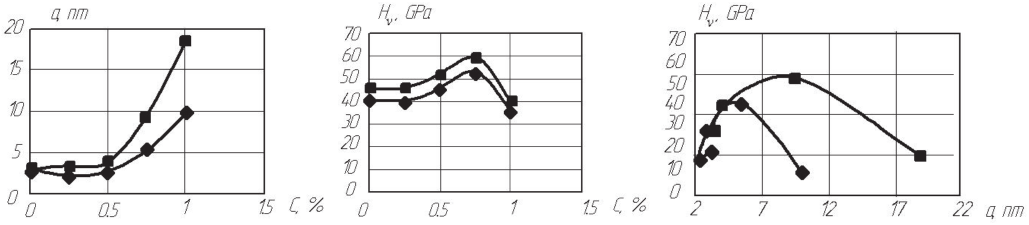

a) b) c)

Fig. 22. Dependence of a) the grain size and b) microhardness on the TiN percentage, c) microhardness dependence on the grain size (■ – maximum value, ◆ – minimum value)
at the temperature T = 273 K for diborides

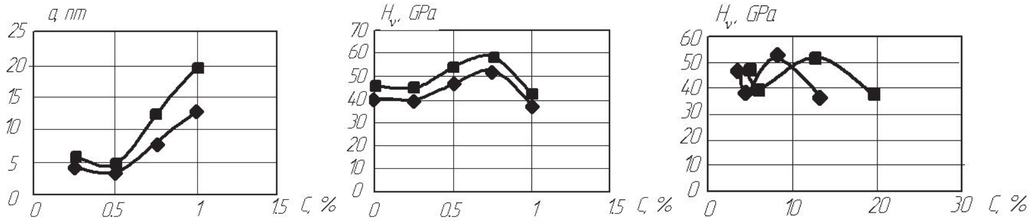

a) b) c)

Fig. 23. Dependence of a) the grain size and b) microhardness on the TiN percentage, c) microhardness dependence on the grain size (■ – maximum value, ◆ – minimum value)
at the temperature T = 973 K for diborides

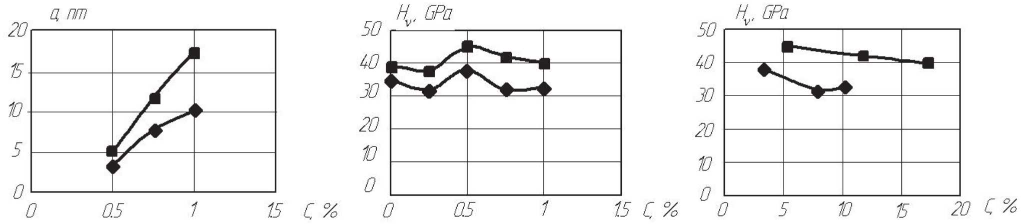

a) b) c)

Fig. 24. Dependence of a) the grain size and b) microhardness on the TiN percentage, c) microhardness dependence on the grain size (■ – maximum value, ◆ – minimum value)
at the temperature T = 1273 K for diborides

The grain size and microhardness dependence on the TiN percentage (Fig. 23(a), (b)) and this coating microhardness dependence on the grain size (Fig. 23(c)) were examined. It is seen that at the TiN concentration growth the grain size increases up to 20 nm (maximum size) and 13 nm (minimum size). The maximum microhardness is achieved at the near 80 % TiN concentration. The microhardness dependence on the grain size (Fig. 2(c)) shows that the maximum value is realized at the about 10 nm grain size at $T = 973$ K.

Similar dependences for $T = 1273$ K are shown on Fig. 24. It is seen that at the TiN percentage growth the grain size increases and achieves maximum value 17.10 nm for 100 % TiN concentration (Fig. 24(a)). The microhardness dependence on the TiN coating percentage is shown in Fig. 24(b). It is seen that microhardness maximum value is realized at the 50 % TiN concentration and near 5 nm grain size (Fig. 24(c)). The grain size influence on the elastic modulus (Young's modulus) was studied in [8] (Fig. 25). The figure shows that the Young's modulus increases with grain size growth for Ni + 2 % (mass.) P (Fig. 25(a)) [37] and for ZrO_2 + 3 % (mass.) Y_2O_3 (Fig. 25(b)).

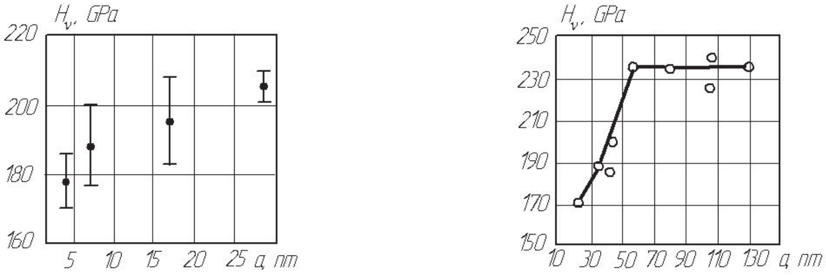

a) b)

Fig. 25. Grain size influence on the Young's modulus for a) Ni + 2% (mass.) P [37] and b) ZrO_2 + 3% (mass.) Y_2O_3 [6]

2.1. Conclusions

The microhardness decrease with grain size increasing for 0.2HfN + 0.8ZrN coated K40, Sandvik Koromant, MS221 materials was disclosed.

Two-layer Al_2O_3 + (0.2HfN + 0.8ZrN) coated Sandvik Koromant plate microhardness changes slightly (due to the fact that almost always nanostructures realized) with the grain growth (33.7-63.8 nm, $H_\mu = 16.08$-17.14 GPa.

The 0.2HfN + 0.8ZrN coated P40 plate microhardness is lower than for other hard alloys with the same coating, that is associated with significantly large grain size, which from nanostructured at the $E_i = 110$ eV transforms to submicrostructured at the $E_i = 250$-500 eV.

The coating effective application criterion will such condition: the coating grain size should be less than the cutting tool base material grain size.

The most effective functioning of the nanostructured coatings is shown.

The grain size increases and the microhardness decreases at the temperature growth.

The maximum microhardness values implemented are realized at the grain sizes in the range of 5 to 10 nm.

The TiN concentration growth in the diboride increases the grain size.

The maximum microhardness is realized at the TiN concentration from 50 % to 80 %.

The maximum microhardness for the diborides are realized in the grains sizes range from 5 to 13 nm.

It has been proved that modulus of elasticity increases at the grain size growth.

3. Coating grain size influence on the material removable volume for the resistance period, the cutting tool durability and the hardened K19195 steels and G10450 steel machining productivity

In order to evaluate the grain size influence on the efficiency of the K19195 hardened steel machining were conducted the investigations of the grain size in the 0.18HfN + 0.82ZrN coating on the P40, K40 (USSR), K40 (Russia), MS221 hard alloys and VOK 60 ultrahard material.

Surface layer composition (a) of the coating and cutting tool, this layer percentage, plate photograph (b) and the surface layer photomicrograph with grain sizes are shown on the Figs. 11-15. It is seen that the grain size for P40 is in the range of 75.1-106 nm for plates processed in the plasma flow center, and in the range of 113-266 nm for the plate on the flow periphery at the 250 eV ion energy. In this case, we observed 32.04 % Zr and 24.95 % Hf in the surface layer. It can be seen that Hf to Zr ratio greatly exceeds the cathode elements ratio what, obviously, due to the zirconium evaporation nature from the plate surface layer, which is larger than hafnium evaporation. As a result, a surface layer is zirconium-depleted, as evidenced by the surface layer percentage composition.

Similar studies for K40 (USSR) plate with the same coating are shown on the Fig. 26. It is seen that the grain size is in the range of 106, ..., 219 nm. If the plates are located on the ions flow axis, the zirconium percentage composition is 56.5 % and hafnium percentage composition is 38.48 %. Whereas if they are located on the periphery, then Zr and Hf percentage is 55.29 % and 37.67 % accordingly. It is seen that in this case the surface layer zirconium-hafnium ratio is increased in relation to hafnium (relative to its cathode portion). It is shown that the coating grain size on the K40 plate is slightly higher than for P40 plate. In this case is realized submicrostructure grain and the surface layer percentage determines the zirconium and hafnium evaporation nature (Zr evaporates faster than Hf)

Investigations of the grain size influence on the removable material volume during the durability period, the durability of the 0.18HfN + 0.82ZrN coated K40 (USSR) cutting tool and K19195 hardened steel processing performance shown (Fig. 26), that material removable volume for durability period G has maximum value $1.8 \cdot 10^4$ mm^3, the cutting tool durability has relatively low value $T = 600$ s and the processing capacity $P = 40$ mm^3/s.

It is obvious that, although this cutting tool effectiveness at the unhardened steel and cast iron processing is high enough, it is small for K19195 hardened steel.

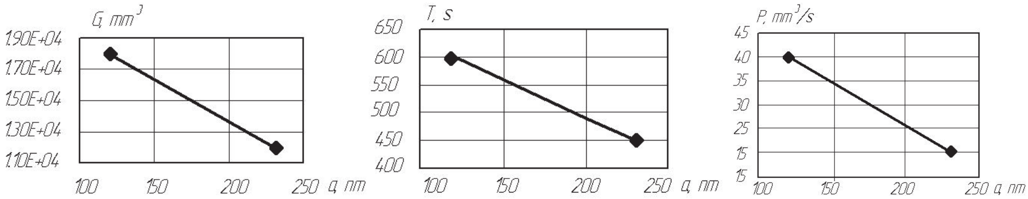

a) b) c)

Fig. 26. Dependencies of a) the K19195 hardened steel removable volume for durability period, b) the 0.18HfN + 0.82ZrN coated K40 (USSR) cutting tool durability and c) processing performance from the grain size

Investigation of the K40 (Russia) plate cutting tool (Fig. 27) revealed that the grain size becomes somewhat larger than K40 (USSR) plate grain size and lies in the range 108-303 nm for the plates on the flow axis and in the range 188-370 nm for plates on the flow periphery. In the first case, the zirconium/hafnium composition ratio is 67.48/28.42. In this case, the percentage compositions ratio is closer to the cathode original ratio. For the periphery plates ratio is close to the P40 ratio and equal 59.16/36.31, i.e. in this case zirconium selective evaporation has large influence on the coating properties (Fig. 27).

Similar dependences for the case of the ShKh15 hardened steel processing by the K40 (Russia) cutting tool with the same coating (Fig. 27) allow to provide the same volume of the removable material over the durability period $3.5 \cdot 10^7$ mm^3 and at the almost nanostructured grain size 106 nm, the grain size growth decreases rapidly to $2.5 \cdot 10^4$ mm^3. The maximum cutting tool durability is realized with another grain size (in the 140-210 nm range) and at the further grain growth cutting tool durability is reduced. Processing performance dependence from the grain size repeats dependence for G and the maximum value is 320 mm^3/s (Fig. 27).

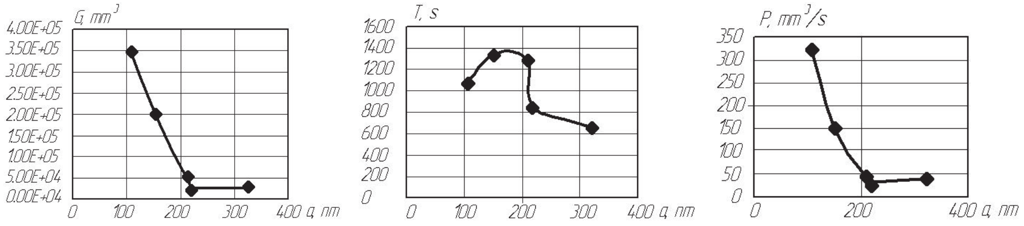

a) b) c)

Fig. 27. Dependencies of a) the K19195 hardened steel removable volume for durability period, b) the 0.18HfN + 0.82ZrN coated K40 (Russia) cutting tool durability and c) processing performance from the grain size

The spectral composition and percentage analysis of the coating on the MS221 plate didn't performed unfortunately. The grain size investigations in the MS221 plate coating is shown on the Fig. 12. Grain size is in the range of 110-229 nm for plates on the flow axis and grain size is 128-428 nm on the flow periphery. In this case microhardness were measured, which, depending on the grain size, in the first instance was in the range 1270-1413 Hv and a larger value corresponds to a smaller grain size, while for the plates, located on the periphery, microhardness ranges is in the range from 915 to 1184 Hv. Measurements were performed by the PMT-3 instrument. In the last case lower microhardness values Hv from 732 to 891 were observed, which are associated with the submicrostructure grain size presence, which turn into microstructure grain. In this case, the microhardness minimum values were implemented.

Analysis of the removable volume dependencies for the durability period G, durability T and processing performance P for K19195 hardened steel turning by the cutting tools from 0.18HfN + 0.82ZrN coated MS221 plate shows that the maximum value of the removable volume $G = 5.5 \cdot 10^5$ mm^3 is obtained with 120 nm grain size, cutting tool durability $T = 870$ s and processing capacity $P = 64$ mm^3/s at the same grain size. It can be seen that 0.18HfN + 0.82ZrN coated MS221 cutting tool allows to obtain acceptable results at the ShKh15 hardened steel processing (Fig. 28).

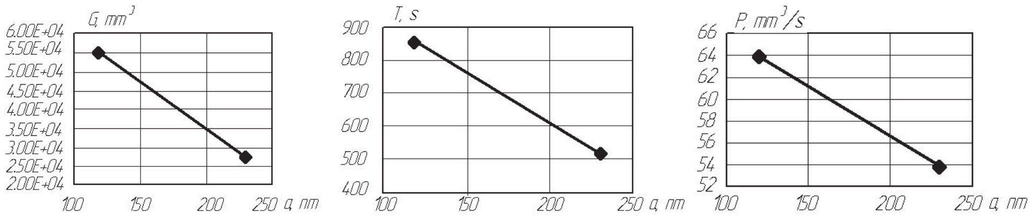

a) b) c)

Fig. 28. Dependencies of a) the K19195 hardened steel removable volume for durability period, b) the 0.18HfN + 0.82ZrN coated MS221 cutting tool durability and c) processing performance from the grain size

If we analyze Table 1 [1] in respect to coating efficiency rating, we find that the coating on the K40 plate with minimal grain size has maximum removable material volume during the durability period, although in this case its durability is somewhat different from the maximum. For the

MS221 plate the mode with fairly high rating on the removable material volume for durability period is realized too and has third rating (Table. 1). Obvious that this material may be used for the ShKh15 hardened steel processing.

VOK60 superhard material use for ShKh15 hardened steel processing showed that the maximum removable material for the durability period $G = 2.6 \cdot 10^5$ mm^3, the maximum durability – $T = 200$ s (implemented at $a \approx 70$ nm), and the maximum processing performance is provided at the grain size 103 nm. It can be seen that the VOK60 superhard material is not effective at the ShKh15 hardened steel processing (Fig. 29).

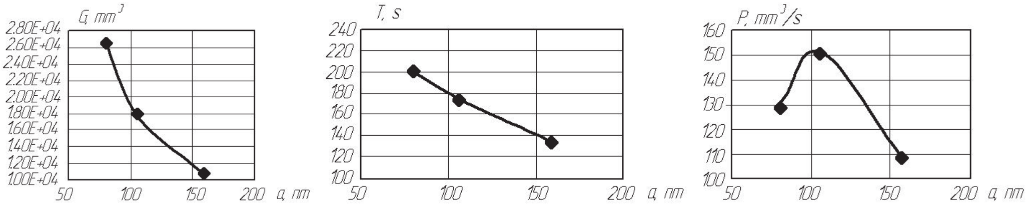

a) b) c)

Fig. 29. Dependencies of a) the K19195 hardened steel removable volume for durability period, b) the 0.18HfN + 0.82ZrN coated VOK60 cutting tool durability and c) processing performance from the grain size

Despite the fact that for coated P40 plate we have the grain size in the surface layer close to nanostructured size, the hardened steel processing tool performance is not high and has only tenth rating. Obviously, it's connected with P40 relatively low microhardness in comparison with K40 that reduces P40 efficiency. Performed investigations of the hard alloy cutting tools performance were also continued for the hardened steel turning; the results are shown on the Figs. 30-36. In this case, as the cutting tool were used 0.18HfN + 0.82ZrN coated carbide Sandvik Koromant, two-layer Al_2O_3 + (0.18HfN + 0.82ZrN) coated Sandvik Koromant and hard alloys P40, MS221. Compared with the previous variants have been added Al_2O_3 + (0.18HfN + 0.82ZrN) coating, for which we have grain sizes from 75.1 to 159 nm, i.e. in this case nanostructured grain was realized, which should provide a high rating. Unfortunately, this coating has fourteenth rating and, in principle, it is don't make sense to use it for the hardened steels processing due to the small Al_2O_3 coating surface layer microhardness. At the same time the 0.18HfN + 0.82ZrN coating on the Sandvik Koromant plate provides maximum efficiency rating and the maximum cutting tool durability. This suggests that cutting tool operability and efficiency provides not only the minimum grain size, but the cutting tool surface layer microhardness, which is equal 35 GPa for this coating.

For the same coating on the MS221 plate is realized the second mode on the material removable volume for the durability period, although the overall rating based on durability and productivity, takes on the maximum value, and this coated hard alloy can be used in all cases for the G10450 hardened steel processing.

Unfortunately, 0.18HfN + 0.82Zrn coated P40 hard alloy can't be used effectively both for G10450 hardened steel machining, and for K19195 hardened steel machining.

Analysis of the 0.18HfN + 0.82ZrN coated MS222 cutting tool research results showed that the maximum removable material volume (45 hardened steel) for the durability period $G = 1.1 \cdot 10^5$ mm^3 at the $a = 70$ nm, the maximum durability $T = 800$ s at the $a = 95$ nm and the productivity $P = 30$ mm^3/s at the $a = 150$ nm. This suggests that each of the productivity and efficiency criteria has own grain size (Fig. 30).

Similar investigations were carried out for the MS221 cutting tool with the same coating (Fig. 34). The maximum value is realized for $G = 1.05 \cdot 10^5$ mm^3 at the $a = 123$ nm, for $T = 850$ s at the $a = 123$ nm and for $P = 40$ mm^3/s at the $a = 210$ nm. For the same MS221 coated cutting tool are realized more efficient modes $G_1 = 7.2 \cdot 10^5$ mm^3 at the $a = 105$ nm (Fig. 32) and

$G_2 = 5.7{\cdot}10^5$ mm^3 for the a = 73 nm (Fig. 33) and $G_3 = 8{\cdot}10^5$ mm^3 (Fig. 34), $T_1 = 2500$ s, $T_2 = 1900$ s and $T_3 = 800$ s, and $P_1 = 400$ mm^3/s, $P_2 = 30$ mm^3/s and $P_3 = 15$ mm^3/s, respectively. It can be seen that the first mode is more preferred, then the second mode can be used for employment.

For 0.18HfN + 0.82ZrN coated Sandvik Koromant cutting tool results of the 45 hardened steel turning are shown on the Fig. 35 and 36. It was found that $G_1 = 1.27{\cdot}10^5$ mm^3 is realized at the $a =$ 110 nm, the $G_2 = 5{\cdot}10^5$ mm^3 for $a =$ 300 nm; $T_1 =$ 4500 s, $T_2 =$ 4000 s, and $P_1 = 50$ mm^3/s and $P_2 = 70$ mm^3/s. It is evident that with the grain size growth all parameters, except P, are reduced, and P increases and reaches a maximum at the $a =$ 560 nm. All this suggests that, despite the fact that the first mode for Sandvik Koromant cutting tool is successful on the removable volume for the durability period and cutting tool durability, but the mode with 560 nm large grain size is more rational on the productivity.

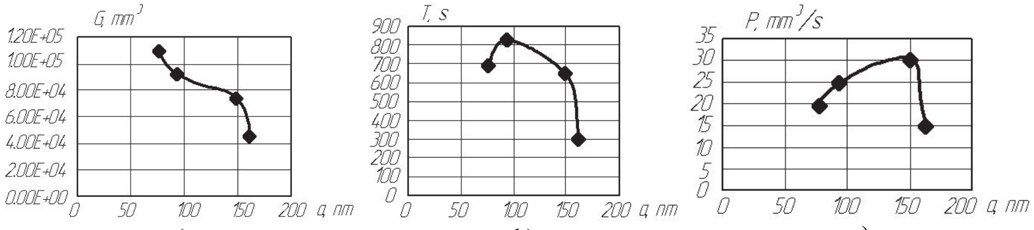

a) b) c)

Fig. 30. Dependencies of a) the manufacturable G10450 hardened steel removable volume for durability period, b) the 0.18HfN + 0.82ZrN coated MS222 cutting tool durability and c) processing performance from the grain size

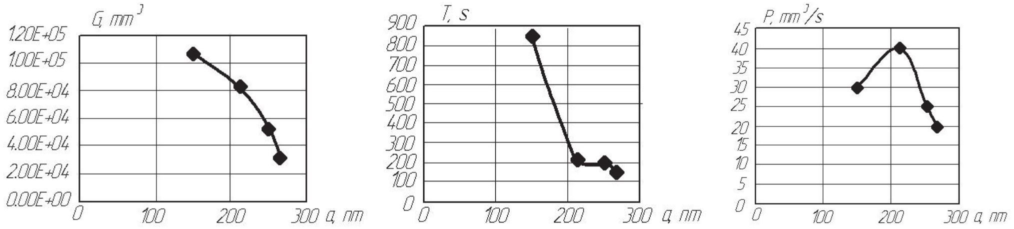

a) b) c)

Fig. 31. Dependencies of a) the manufacturable G10450 hardened steel removable volume for durability period, b) the 0.18HfN + 0.82ZrN coated MS221 cutting tool durability and c) processing performance from the grain size

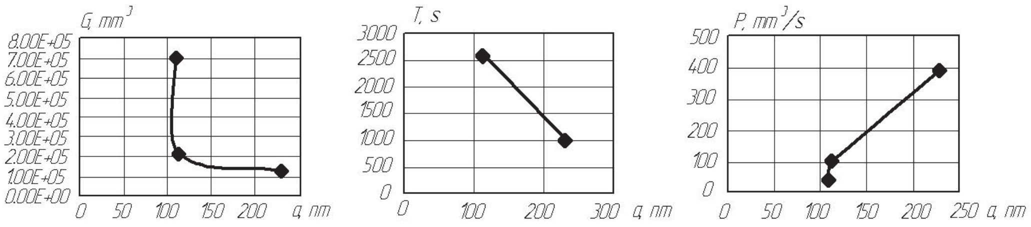

a) b) c)

Fig. 32. Dependencies of a) the manufacturable G10450 hardened steel removable volume for durability period, b) the 0.2HfN + 0.8ZrN coated MS221 cutting tool durability and c) processing performance from the grain size

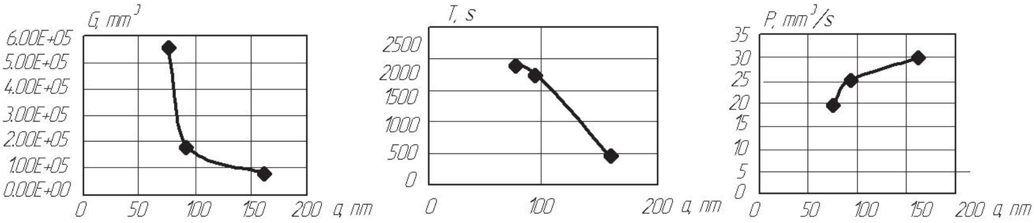

a) b) c)

Fig. 33. Dependencies of a) the manufacturable G10450 hardened steel removable volume for durability period, b) the 0.2HfN + 0.8ZrN coated MS221 cutting tool durability and c) processing performance from the grain size

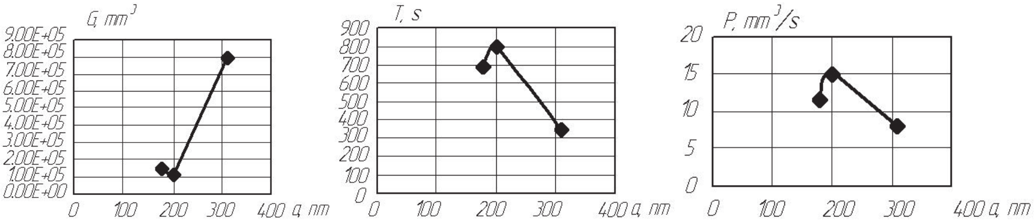

a) b) c)

Fig. 34. Dependencies of a) the manufacturable G10450 hardened steel removable volume for durability period, b) the 0.2HfN + 0.8ZrN coated MS221 cutting tool durability and c) processing performance from the grain size

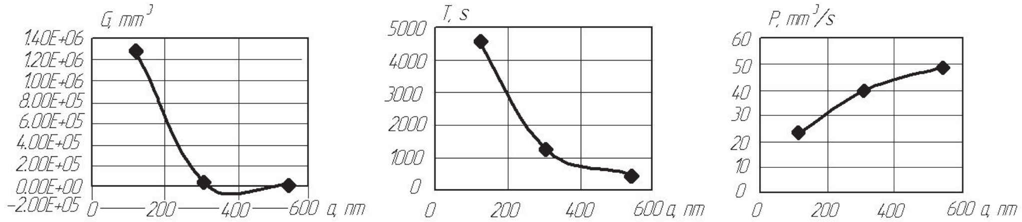

a) b) c)

Fig. 35. Dependencies of a) the manufacturable G10450 hardened steel removable volume for durability period, b) the 0.2HfN + 0.8ZrN coated Sandvik Koromant cutting tool durability and c) processing performance from the grain size

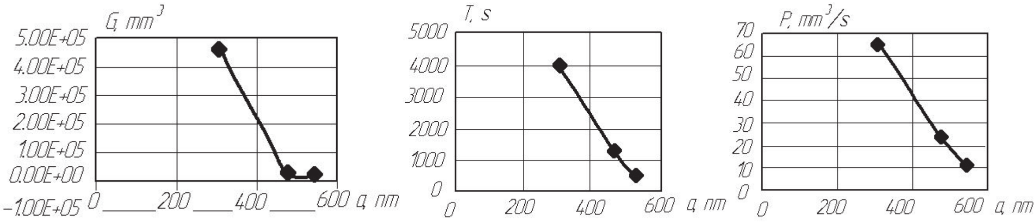

a) b) c)

Fig. 36. Dependencies of a) the manufacturable G10450 hardened steel removable volume for durability period, b) the 0.2HfN + 0.8ZrN coated Sandvik Koromant cutting tool durability and c) processing performance from the grain size

3.1. Conclusions

1) It is shown that at the effectiveness and efficiency assessing of the coated hard alloys at the K19195 hardened materials and G10450 steel processing it is necessary to take into account the coating grain size at that to the smaller grain size is generally (but not always) corresponds to more

effective processing (the maximum removable material volume for the durability period) and its working capacity.

2) For 45 steel effective processing can be used hard alloy of the Sandvik Koromant company with 0.18HfN + 0.82ZrN coating and MS221hard alloy, which will be both effective and serviceable.

3) It was found that 0.18HfN + 0.82ZrN coated K40 hard alloy and MS221 plate with the same coating have greater efficiency for the K19195 hardened steel processing.

4. The cast iron machining effectiveness by the nano- and submicrostructure coated cutting tool

Investigation results of the material removable volume for the durability period G, cutting tool durability and iron cast machining performance P are shown on the Figs. 37-46. Thus, in the special cast iron machining case by the 0.2HfN + 0.8ZnN coated Sandvik Koromant company cutting tool at the coating deposition displacement potentials are $U = 250$ V and $U = 500$ V (Figs. 37 and 38 respectively). Obviously, that at the smaller values of $U = 250$ V removable volumes value significantly greater than for $U = 500$ V; also the cutting tool durability values are higher, which with the grain size growth is reduced substantially: from $G = 1.2 \cdot 10^6$ to $2 \cdot 10^5$ mm^3 ($U = 250$ V) and $T = 1700$ to 200 s ($U = 250$ V) and from $G = 7.2 \cdot 10^5$ to $1.8 \cdot 10^5$ mm^3 and $T = 770$ to $T = 270$ s ($U = 500$ V). All this confirms the theoretical predictions that these values are associated with cutting tool material physical and mathematical properties, which with the grain size growth is reduced, that leads to these quantities dependence on the grain size. The maximum processing performance for $U = 250$ V is realized at the grain size near 110 nm, while for $U = 500$ V it realized at the grain size about 150 nm. Material removable volume over the durability period, cutting tool durability and machining performance which can be used at the processing by 0.2HfN + 0.8ZnN coated Sandvik Koromant tool may be estimated on these dependencies.

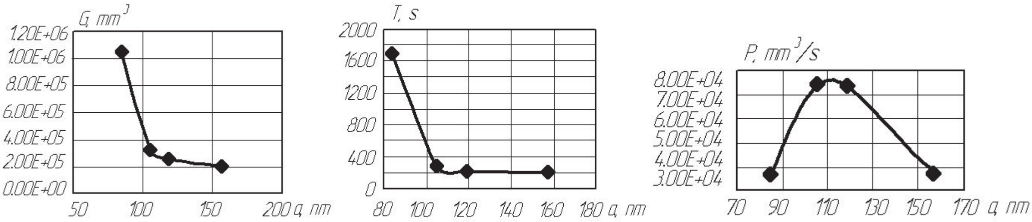

a) b) c)

Fig. 37. Dependencies of a) the manufacturable special cast iron (NiW) removable volume for durability period, b) the 0.2HfN + 0.8ZrN coated Sandvik Koromant cutting tool durability at the displacement potential (U = 250 V) and c) processing performance from the grain size

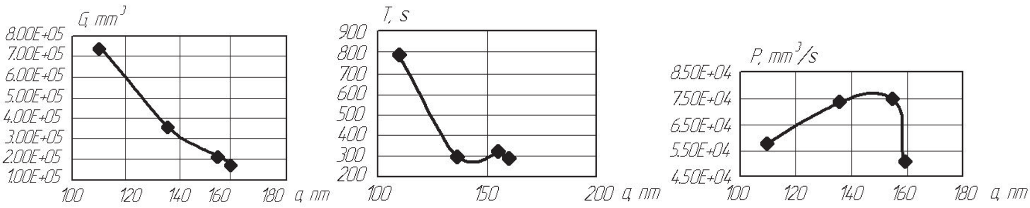

a) b) c)

Fig. 38. Dependencies of a) the manufacturable special cast iron (NiW) removable volume for durability period, b) the 0.2HfN + 0.8ZrN coated Sandvik Koromant cutting tool durability at the displacement potential (U = 500 V) and c) processing performance from the grain size

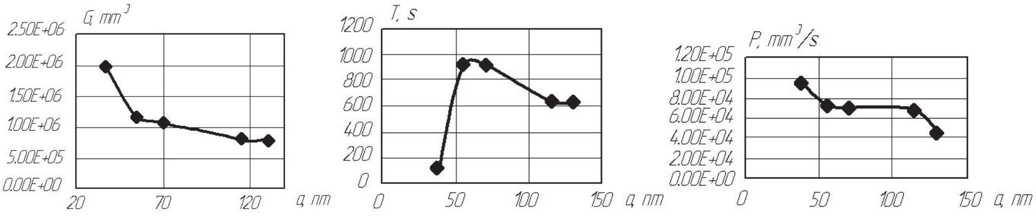

a) b) c)

Fig. 39. Dependencies of a) the manufacturable special cast iron (NiW) removable volume for durability period, b) the 0.2HfN + 0.8ZrN coated MS221 cutting tool durability at the displacement potential (U = 250 V) and c) processing performance from the grain size

Similar dependences for the case of the cast iron machining by 0.2HfN + 0.8ZnN coated MS221 cutting tool at the displacement potential $U = 250$ V are shown in Fig. 39. Evidently that the removable volume and productivity are reduced with the grain size growth, while the cutting tool durability has maximum value, for nanostructured grain ($a = 35$ nm) productivity G reaches $2 \cdot 10^6$ mm^3 and then decreases to $7.5 \cdot 10^5$ mm^3 at the $a = 130$ nm. Durability maximum is realized at the 60 nm grain size, and at the smaller and larger grain size durability is somewhat lower. Productivity for nanostructured grains is 10^5 mm^3/s, i.e. presented dependences allow to evaluate the performance of the coated MC221 tricarbidic hard alloy at the cast iron processing.

A similar dependences for processing of the of special cast iron by 0.2HfN + 0.8ZnN coated K40 (Russia) cutting tool at the displacement potential $U = 250$ V are shown on the Fig. 40. Evidently, that the removable volume is significantly reduced with increasing grain size and at the 130 nm grain size the cutting modes are almost unacceptable for processing. At the same time durability dependence has nonmonotonic character: at first it reduced, then it rises, and the minimum durability is realized at the 120 nm grain size. Productivity behaves similarly – it is maximal both at the small grain size (80 nm) and large grain size (120 nm).

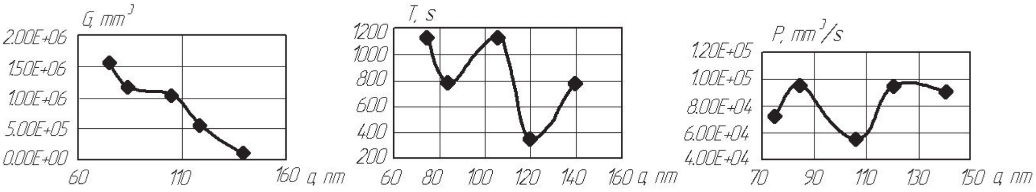

a) b) c)

Fig. 40. Dependencies of a) the manufacturable special cast iron (NiW) removable volume for durability period, b) the 0.2HfN + 0.8ZrN coated K40 (Russia) cutting tool durability at the displacement potential (U = 250 V) and c) processing performance from the grain size

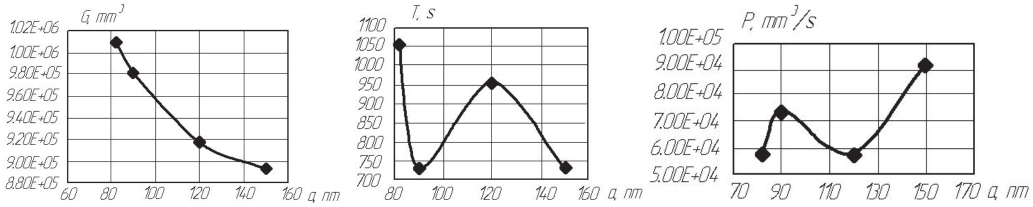

a) b) c)

Fig. 41. Dependencies of a) the manufacturable special cast iron (NiW) removable volume for durability period, b) the 0.2HfN + 0.8ZrN coated K40 (Russia) cutting tool durability at the displacement potential (U = 500 V) and c) processing performance from the grain size

For the same cutting tool with the same coating but at the 500 V potential (Fig. 41) maximum removable volume significantly decreased, although durability remained practically permanent.

Al_2O_3, durability and productivity changes have undulating character. The maximum grain size is equal 120 nm.

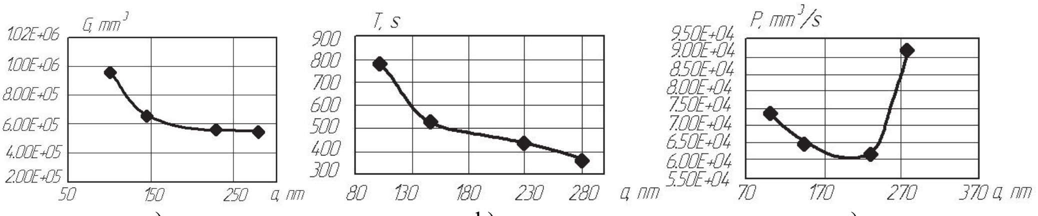

a) b) c)

Fig. 42. Dependencies of a) the manufacturable special cast iron (NiW) removable volume for durability period, b) the 0.2HfN + 0.8ZrN coated K40 (Russia) cutting tool durability at the displacement potential (U = 110 V) and c) processing performance from the grain size

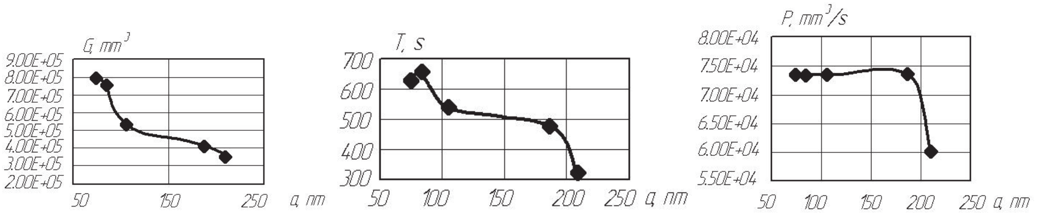

a) b) c)

Fig. 43. Dependencies of a) the manufacturable special cast iron (NiW) removable volume for durability period, b) the 0.2HfN + 0.8ZrN coated P40 cutting tool durability at the displacement potential (U = 250 V) and c) processing performance from the grain size

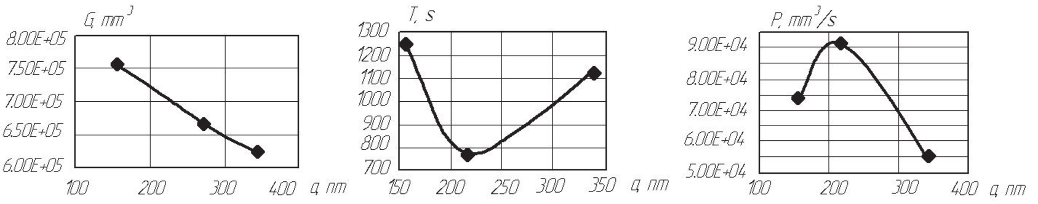

a) b) c)

Fig. 44. Dependencies of a) the manufacturable special cast iron (NiW) removable volume for durability period, b) the 0.2HfN + 0.8ZrN coated K40 (USSR) cutting tool durability at the displacement potential (U = 250 V) and c) processing performance from the grain size

For similar conditions, but with displacement potential equal 110 V, removable volume decreased, durability also decreases relatively smoothly and the productivity is reduced firstly and then reaches to the maximum value at the 275 nm size – Fig. 42. The cast iron processing effectiveness by P40 cutting tool with the same coating when the displacement potential is 250 V is low, since removable volume is reduced to $8 \cdot 10^5$ mm^3, the maximum durability is 660 s, but the productivity is maintained at the high level in the grain sizes range from 70 to 180 nm and equal $7.4 \cdot 10^4$ mm^3/s (ris.43). For the case of the special cast iron processing by K40 (USSR) cutting tool with the same coating at the 250 V displacement potential results are shown on Figs. 42-44. It can be seen that the removable volume is approximately the same as for P40 plate and decreases with grain size increasing due to rather high grain size values. At the grain growth the durability at first decreases and then slightly increases (minimum value at the 215 nm grain size), whereas productivity in this case has maximum value (Fig. 44).

At the cast iron processing by the TH20 cutting tool with the same coating at 250 V displacement potential the removable volume is relatively little, durability is low too and the maximum productivity is realized at the 240-320 nm grain size and equal $9.3 \cdot 10^4$ mm^3/s, i.e. this mode is favorable for the maximum processing productivity case (Fig. 45).

Similar dependences for the special cast iron processing case by Al_2O_3 + 0.2HfN + 0.8ZrN coated Sandvik Koromant cutting tools show that the maximum removable volume increased by more than an order of magnitude. This is due to the fact that the Al_2O_3 coating (cutting tool outer coating) has minimal adhesive interaction with cast iron, what provides minimum adhesive wear and friction coefficient significant reduction, but even with the grain size growth in the nanostructured range (from 37 to 95 nm), removed metal volume value still decreases. Durability also decreases with grain size increasing, but productivity increases and reaches maximum value at the 95 nm grain size. Obviously that the two-layer coating at the cast iron processing has large advantages, since adhesive wear is the main wear form and Al_2O_3 outer coating significantly reduces its (Fig. 46).

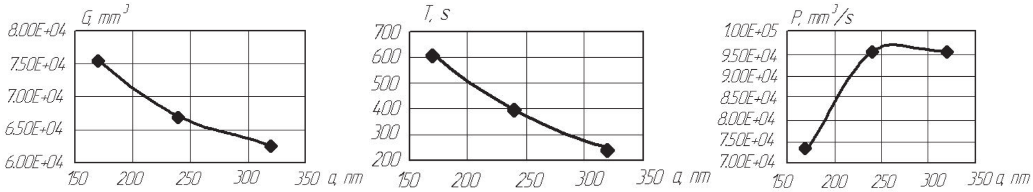

a) b) c)

Fig. 45. Dependencies of a) the manufacturable special cast iron (NiW) removable volume for durability period, b) the 0.2HfN + 0.8ZrN coated TH20 cutting tool durability at the displacement potential (U = 250 V) and c) processing performance from the grain size

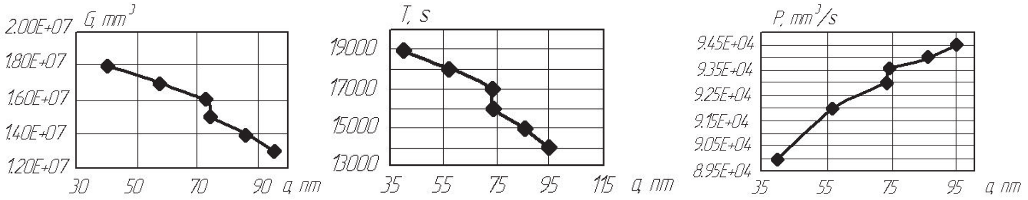

a) b) c)

Fig. 46. Dependencies of a) the manufacturable special cast iron (NiW) removable volume for durability period, b) the Al_2O_3 + 0.2HfN + 0.8ZrN coated Sandvik Koromant cutting tool durability and c) processing performance from the grain size

It has been shown that at the cast iron processing the coating adhesive interaction with the manufacturable material is an important characteristic which provide unique value of removable volume for durability period of the $1.3 \cdot 10^7$-$1.8\ 10^7$ mm^3 order. The maximum durability (19,000-14,000 s) also realized in this case, maximum productivity is realized at the minimum G and T values.

MS221 ($U = 250$ V), Sandvik Koromant ($U = 250$ V) and VK8 (Russia) ($U = 250$ V) cutting tools have acceptable processing modes. All other cutting tools and coating deposition modes are less effective.

Performed investigations allow to predict the removable material volume over the durability period, cutting tool durability and processing productivity depending on the coating grain size. It is important to select the cutting tool coating and processing mode.

5. Conclusions

The microhardness and yield strength decrease with grain size increasing for wide range of the 0.2HfN + 0.8ZrN coated materials (K40, Sandvik Koromant, MS221) was disclosed.

Two-layer Al_2O_3 + (0.2HfN + 0.8ZrN) coated Sandvik Koromant plate microhardness changes slightly (due to the fact that almost always nanostructures implemented) with the grain growth

(33.7-63.8 nm, H_{μ} =16.08-17.14 GPa.

The coating effective application criterion will condition: the coating grain size should be less than the cutting tool base material grain size.

Maximum microhardness is realized at the TiN concentrations in diborides from 50 to 80 % and grain sizes range from 5 to 13 nm.

It is proved that modulus of elasticity increases with the grain size growth.

It is shown that at the effectiveness and efficiency assessing of the coated hard alloys at the K19195 hardened materials and G10450 steel processing it is necessary to take into account the coating grain size at that to the smaller grain size is generally (but not always) corresponds to more effective processing (the maximum removable material volume for the durability period) and its working capacity.

For G10450 steel effective processing can be used 0.18HfN + 0.82ZrN coated Sandvik Koromant company solid alloy, MS221 and K40, which will be both effective and operable.

It found that at the cast iron processing the coating adhesive interaction with the manufacturable material is an important characteristic which provide unique value of removable volume for durability period of the 1.3 10^7-1.8 10^7 mm^3 order. The maximum durability (19,000-14,000 s) also realized in this case, maximum productivity is realized at the minimum G and T values.

Performed investigations allow to predict the removable material volume over the durability period, cutting tool durability and processing productivity depending on the coating grain size. It is important to select the cutting tool coating and processing mode.

References

[1] **Gusev A. I.** Nanocrystalline Materials: Methods of Obtaining and Properties. Publishing House of RAS, Ekaterinburg, 1998, p. 302.

[2] **Andrievsky R. A.** Nanomaterials: the concept and modern problems. Physics of Metals and Metallography, Vol. 91, Issue 1, 2003, p. 50-56.

[3] **Gusev A. I.** Nanomaterials, Nanostructures, Nanotechnologies. Fizmatlit, Moscow, 2005, p. 416.

[4] **Kostyuk G. I.** Nanotechnology: Selection of Technological Parameters and Installations, Processing Capacity, Physical and Mechanical Characteristics of Nanostructures. Publishing House of the International Academy of Science and Innovate Technologies, 2014, p. 479.

[5] **Kostyuk G. I.** Nanotechnology: Theory, Experiment, Technology, Perspectives. Technologies, 2012, p. 648.

[6] **Kostyuk G. I.** Nanostructures and Nanocoatings: Perspectives and Reality. Zhukovsky "KhAI", 2009, p. 406.

[7] **Kostyuk G. I.** Physical and technical principles of coating, ion implantation and ion doping, laser processing and hardening, combined technologies. Book 1. Physical Processes of Plasma-Ion, Ion-Beam, Plasma, Light-Beam and Combined Technologies. Publishing House of the AINU, 2002, p. 596.

[8] **Kostyuk G. I.** Physical and Technical Principles of Coating, Ion Implantation and Ion Doping, Laser Processing and Hardening, Combined Technologies. Book 2. Handbook for Calculating the Basic Physical and Technological Parameters, Assessing the Possibilities, Choosing the Type of Technology and Equipment. Publishing House of the AAS, 2002, p. 482.

[9] **Kostyuk G. I.** Effective Tool with Nanocoatings and Nanostructured Modification Layers. Book. 1. Plasma-Ion and Ion-Beam Technologies, Publishing House "Planet-print", 2016, p. 735.

[10] **Kostyuk G. I.** Effective Tool with Nanocoatings and Nanostructured Modification Layers. Book. 2. Laser Technologies, Publishing House "Planet-print", 2017, p. 507.

[11] **Kostyuk G. I.** Effective Coatings and Modified Hardened Layers on Cutting Tools. Publishing House of the International Academy of Science and Innovate Technologies, 2012, p. 728.

Kostyuk Gennady Igorevich Professor of the Department of Theoretical Mechanics, Machine Science and Robot Mechanics Systems of the National Aerospace University. N. E. Zhukovsky "KhAI", vice-president of the International Academy of Sciences and Innovative Technologies. Doctor of Technical Sciences, Professor, Academician of the Academy of Engineering Sciences and the Academy of Sciences of Technological Cybernetics of Ukraine. The scientific heritage of G. I. Kostyuk counts 1070 scientific works (including 210 works in the far abroad), 8 of them are monographs, 32 textbooks and textbooks, 12 patents for inventions and 13 copyright certificates. Under his leadership is protected 4 doctoral and 25 master's theses.

4.3. Effect of technological factors on electromagnetic wave absorption properties of the polymer composites

Tamaz Natriashvili[1]**, Jimsher Aneli**[2]**, Lana Shamanauri**[3]
R. Dvali Institute of Machine Mechanics, 10 Mindeli Str., Tbilisi 0186, Georgia
E-mail: [1]*T_natriashvili@yahoo.com*, [2]*jimaneli@yahoo.com*, [3]*lana-Shamanauri@mail.ru*

Abstract. Effect of different technological factors on the electromagnetic wave (EMW) with frequencies (3-10 GHz) absorbing properties of polymer composites based on epoxy and silicon resin with electric conducting (carbon black, graphite) and magnetic (nickel, cobalt, ferrite) nanofillers have been investigated. There are obtained the composites with one and binary fillers, concentration of which changes in the wide range. Relatively high absorption is manifested for composites containing 40-50 wt% filler. It is established that the high frequency absorption capability of investigated materials essentially increases with the degree of homogeneity of distribution of filler particles in the polymer matrix. For the composites with ferrite and graphite so called synergistic effect (non-additive increasing of some parameters at definite proportion of two or more fillers) was observed. By variation of the absorber profile the composite with maximal absorption of EMW has been selected. Besides of the effect of electric and magnetic fields at hardening of the composites on the wave absorbing capability has been investigated. It is established that the level of the EMW absorption may be regulated by collection of the sandwich type absorber contained several absorbing films with different distribution and content of these films.

Keywords: polymer composite, electric and magnetic fillers, absorption of electromagnetic waves, synergistic effect, sandwich type absorber.

1. Introduction

Currently a great interest causes the problem of the absorption of high and ultrahigh frequency electromagnetic waves (from the range hundred millions to several ten milliards Herz) by different materials, because this problem is significant at solution of many practical tasks [1, 2]. These materials in the form of thin plates often are used in design of the cameras without echo with radio-engineering destination. These materials are used also for the protection of communication equipment's and staff, etc. [2-4]. In general, the absorbers of EMW present the ceramic and polymer composites filled with different effectively absorbing fine dispersed fillers or constructions, at interaction with which the intensity of these waves decreases essentially [5]. The absorbers of EMW waves are used widely for design of the complexes including antenna system [6]. The materials absorbing EMW are used also in the sphere of sertification of compatibility with electromagnetic waves [7].

The EMW absorbers on a physical basis divided on three groups:

1. Materials and installations, in which the decreasing of the reflected energy is reached by their muffling near absorber surface because of interference, which are manufactured as the package of thin plate like absorber films [8, 9].

2. Second group includes the materials, in which EMW energy translates to thermal energy on the basis of dielectric loses and in result of muffling of waves in absorber with structural inhomogeneity. This group includes also the absorbing coatings made from all organic and inorganic material, by which the reflecting materials (usually metallic) are coated. In this case the coatings absorb the amount of the EMW energy more than they rich to the reflective surface. The absorbers of these groups have very high design, which is presented as the tubular cells, usual cells, conical, pyramidal, honeycomb, wedge-shape, porous rubber carpets et al, the fundamental principle of which is the monotonic increasing of the amount of included particles, which are responsible in the absorbing-reflecting processes [10].

3. This group includes the ferromagnetic materials interacting with E and H fields of EMW

and have the electric and magnetic losses. They are produced mainly as ferrite plates or the rubber carpets. The creation of the absorbers on their basis now is very perspective and actual [11].

Classification of the radio-wave absorbing materials (RAM) has a conditional character. The resonance or frequently tuned RAM provides the partial or full neutralization of the emitted energy. The neutralization effect is importable for absorber, the thickness of which is equal to 1/4 of the wave length. In this case the waves reflected from absorber surface are in anti-phase to incident wave and consequently in result of interference of these waves it takes place neutralization of the waves (Yauman effect). Consequently, the considered phenomenon realized only in the case of fixed frequency of EMW.

The absorbers on the basis of ferromagnetic fillers mainly included the fine dispersed magnetic particles (the nanoparticles among them) are characterized with wide range of absorbed waves (in result of absorption and reflection of the EMW). This absorption is based on increasing of both dielectric and magnetic loses [12-14].

The RAM filled with different type ferromagnetic (shortly magnetic) high dispersive particles at irradiation by EMW under effect of alternative magnetic fields take participation in the oscillatory motion and the high frequency energy translates to the heat one. The heat energy dissipates and disappeared. There are the RAM consisting electric conducting material and dielectric layers. Weakening of the reflected wave is due to summation of the opposite phases of the waves (interference) reflected from the object metal surface, dielectric and electric conducting layer [15, 16]. Besides of today the works on the noted problem are sufficiently large, many unresolved issues are stay, among which the mechanism of the absorption of the EMW in the heterogeneous organic or inorganic systems is very essential. One of the main embarrassing inhibitory reasons of widening the investigations on the given theme is the strong dependence of the absorption energy on the frequency of EMW.

The aim of the presented work is creation of the materials effectively absorbing RW on the basis of new polymer composites containing electric conducting and magnetic fine dispersed powders.

2. Experimental

Experimental manipulations were provided in two directions: 1) Obtaining of the polymer composites and 2) measurements for establishment of absorption of the EMW energy by composite materials.

2.1. Research objects and methods of obtaining

The samples on the basis of diane epoxy resin and some inorganic (graphite, carbon black, ferrite, cobalt micro-particles and nickel nano-particles) fillers were obtained. Polyethylene polyamine was used as a hardener. In the second series the polydimethylmethylvinylsiloxane resin as polymer matrix was used for obtaining the EMW absorber including the same fillers. The composites were obtained by following manipulations of the procedures: 1) Mixing of ingredients in the spatial mixer; 2) Placing of reaction blend to the cuvette with form of parallelepiped and sizes 70×50×5 cm; 3) Solidification of blends; 4) 3-fold sandwich type absorbers preparation by gluing the plates with thickness 1 mm.

With aim of study of the dependence of absorption properties of the composites the samples with different geometrical shapes and surfaces were obtained (Fig. 1). There were obtained the samples with following forms: a) saw type; b) rectangle sinusoidal and c) conic like. With this aim it was prepared the cuvettes with corresponded profiles from Teflon: a) rectangular sinusoidal, b) conical axial section and c) saw profile.

2.2. Testify of the obtained composites on EMW absorption

The sample testing of the obtained composites on EMW absorption was provided on the installation presented on the Fig. 1.

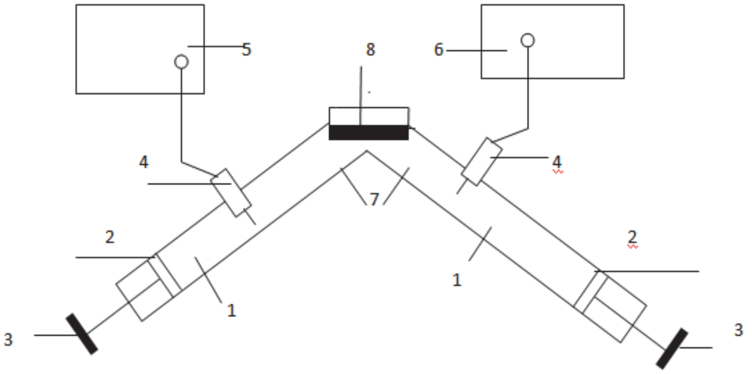

Fig. 1. Scheme of registration of the EMW reflected from samples: 1 – waveguide made from brass list, 2 – plunger – coordinator, 3 – its handle, 4 – the transmitting and receiving antennas (left contains the detector), 5 – generator of super high frequency, 6 – coordinator of the reflected EMW intensity, 7 – substrate of waveguide, 8 – reflecting plate with sample (attached from below)

The principle of working on the device is the following: EMW generated on the generator 5 with use of the transmission transfers to the waveguide and falls on the reflector plate 7 (without sample) and after reflection from it transfers to second wave guide, oriented in rectangular direction to first one, from which transmits through the receiver antenna 4 to the detector 6 and fixes as signal on the zero-indicator (is measured in the decibels). So, the device gives possibility of measuring of EMW intensity of reflected waves of any frequencies from the range 3-10 GHz. After that, they are placed on the surface of the reflector plate the sample and repeat the manipulations described above. By comparison of the intensities (in decibels) reflected from reflector without and with sample one estimates the ability of the absorption properties of the composite. Testify was provided by following manipulations: 1) switching of the device; 2) after 15-20 min the measuring of the intensity of reflected waves intensity from plate without sample; 3) displacement of the sample on the plate; 4) measuring of the wave intensity reflected from sample; 5) establishment of the absorption ability of the composite by comparison of intensities reflected from plate without and with sample.

3. Results and discussion

There were conducted the experiments, main aim of which was the research of the EMW absorbing ability of the obtained polymer composites taking into account of such factors, as the type and composition of the investigated composites. Besides of it was interesting to define the some features of composite structure after influence of different physical factors on the microstructure during hardening of the material (effect of high electric and magnetic fields, geometry of the samples).

3.1. Dependence of the EMW absorption on the recipe of composites

Experiments were conducted on the composites on the basis of diane epoxy resin and inorganic fillers - graphite, carbon black, ferrite and some metal micro-powders.

From the character of the curves presented on Fig. 2 it is clear that if at low concentrations of fillers, the curves have an ascendant character, after definite concentrations these curves become descending. It is known that in general pure polymers, as a rule are transparent to radio waves and after introduction to them particles effectively reactive with EMW the value of absorption or reflection processes increase. However, after definite concentration of such fillers the increasing of the EMW slows down and at future increasing of the filler concentrations the absorption of EMW decreases. The main reason of these phenomena is due to proportion of two processes – absorption and reflection of the EMW after impact of them on the filler particles. If in composites containing relatively low concentrations of fillers a process of absorption prevails the process of reflection (absorption grows) at more high concentrations of the fillers the second process (reflection) gradually grows because of increasing of the integral reflecting surface (a sum of the part of filler particle surfaces located in perpendicular to waves falling on these surfaces of the fillers) and at high concentrations already reflection is prevails the absorption, in result of which the material becomes a reflector of EMW.

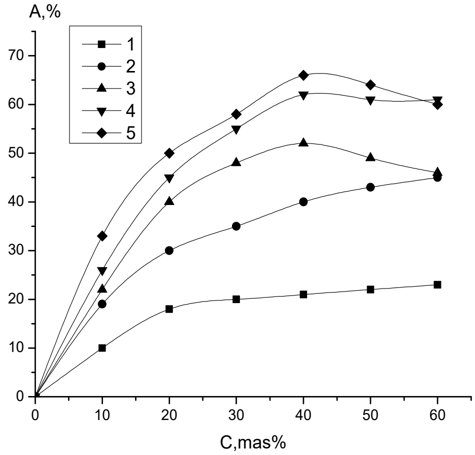

Fig. 2. Dependence of the EMW absorption of composites containing different fillers: carbon black of type P803 (1); carbon black of type P357 (2); synthetic graphite (3); natural graphite (4); blend of synthetic and natural graphite (content 50/50 %) (5)

The analysis of the curves presented on the Fig. 2 shows that best result gives the composite containing two types of fillers – the blend of synthetic and natural graphite. This fact leads to opinion that the falling on the sample the EMW undergoes to diffraction and interference on the two types filler particles in different ways with enhancing of these processes. The composites containing natural graphite show also good absorption properties at definite filler concentrations.

3.2. Dependence of the absorption properties of composites on the homogeneity of filler particles distribution in the polymer matrix

It was interesting to define the dependence of EMW absorption properties of composites on the homogeneity of filler particles distribution in the polymeric matrixes. The experiment was conducted on the composites based on epoxy resin and graphite high dispersive fillers. The homogeneity of the composite plate was studied with estimation of the local elemental square (5×5 mm) average electric resistivity on the plate. Definition of the ratio of average resistance of the elemental squares on the average resistivity of the full plate gave the degree of homogeneity of the material. From the Fig. 3 it is shown that the increasing of the structural homogeneity of the polymer composite correspondingly stipulates EMW absorption. The explanation of this phenomenon may be connected with existing of different resonance structures the polymer matrix, in result of which the absorption process is conducted with gradual connecting of this structures at different frequencies EMW.

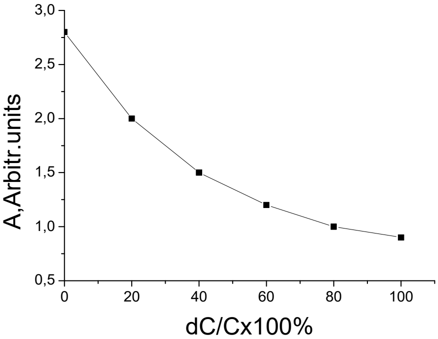

Fig. 3. Dependence of EMW absorption on the degree of homogeneity of the filler particles distribution in the polymer matrix, C is filler concentration and dC/C the relative derivation of the filler concentration from it average value

3.3. Dependence of EMW absorption of the composites on the EMW frequency

The curves on the Figs 4-7 show that the value of the RW absorption depends both on composite composition and on the frequency of EMW. Here one can see the different extremes on the curves. The location of the minimums on the curves and their depths are dependent on the type and concentration of the fillers. Namely, the composite containing 20 wt% graphite is characterized with one minimum near 6,2 GHz and 7.2 GHZ frequencies, which are correspond to 5 and 3 Db, respectively. The composite with 30 wt% of graphite is characterized with analogical minimum near 6.3 GHz (8 Db), while for composites with 40 and 50 wt% such minimums (10.5 and 9.5 respectively) appear at one and same frequency (6.2 GHz). The sample containing 50 % graphite shows the similar minimums (9.5 Db at 5.5 and 6.2 GHz respectively). Composite with 40 wt% graphite appears the maximum of the EMW absorption (10.5 Db).

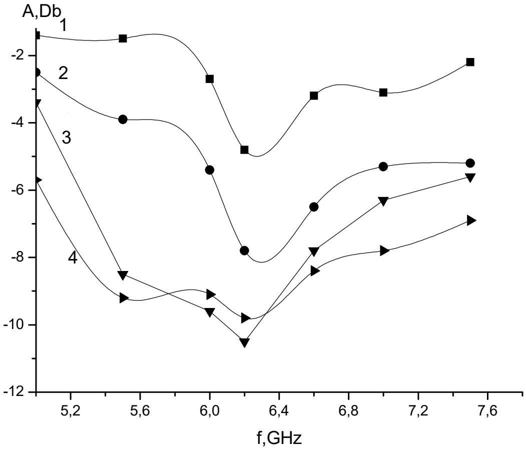

Fig. 4. EMW absorption ability of the composites based on epoxy resin and graphite for following concentrations of the filler (in wt%): 20 (1), 30 (2), 40 (3), 50 (4)

The character of considered dependences mainly is based on the well-known phenomenon, which is responsible for the extremes of the properties at fixed concentration of the filler – on two competing processes (absorption and reflection of EMW). One from them increases at relatively low concentrations of the filler and second one – at relatively high concentrations, which is due to gradation of the filler absorption – reflection processes: at high concentrations the proportion of reflection in the reflected intensity increases, which leads to decreasing of the global absorbed intensity EMW.

The main reason of the absorption of the EMW can be ascribed to interference-diffraction phenomena, which usually take place in the heterogeneous composites. In this case it must be foreseen a high heterogeneity of the investigated materials and based on it the heterogeneous character of the composite structure. Therefore, it is admissible that the separate region of the composite can be differed structurally from the neighbor one. Respectively the physical properties of lasts must be depended on the region coordinates. In this case it will be admissible that the EMW absorption properties of separate regions will be differ one from another in result of realization of the individual diffraction-interference processes in these regions. Therefore, the absorption properties of one and same composition can be changed by monitoring of the material microstructure, or, in other words by technological manipulations. The dependences of the absorption properties on the frequency of EMW presented on the Figs. 4-7. This phenomenon probably may be described in terms of difference in local microstructure, partially by the local resonances of diffraction-interference phenomena.

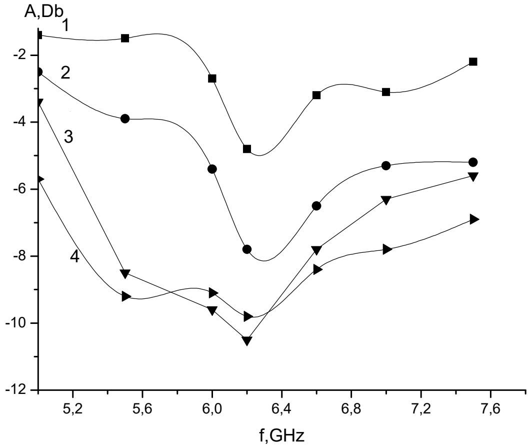

Fig. 5. EMW absorption ability of the composites based on epoxy resin and graphite for following concentrations of the filler (in wt%): 20 (1), 30 (2), 40 (3), 50 (4)

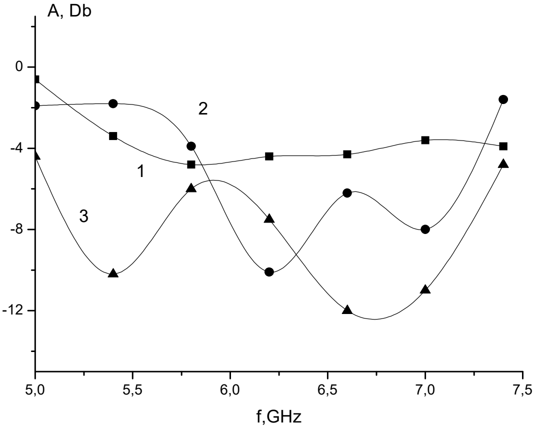

Fig. 6. EMW absorption ability of the composites based on epoxy resin and ferrite for following concentrations of the filler (in wt%): 20 (1), 30 (2), 40 (3)

The data obtained from Figs 5-8 allow us to express the opinion that the EMW absorption ability of the composites with binary filler is essentially depends not so much on filler concentration but on the proportion of the components included to this combined filler. Here it appears so called synergistic effect. The best result (maximal absorption EMW) is reached for composite with 25-25 wt% of the graphite and ferrite powders blend.

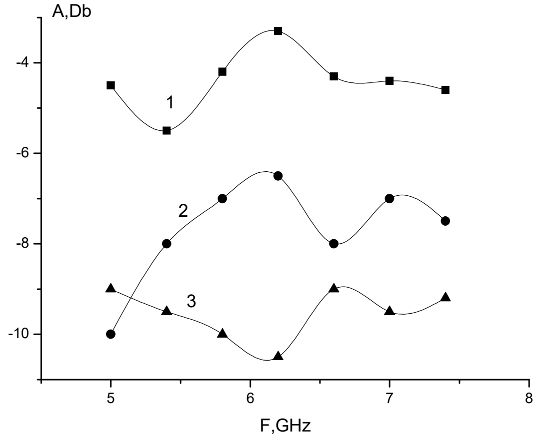

Fig. 7. EMW absorption ability of the composites based on silicon rubber and graphite for following concentrations of the filler (in wt%): 30 (1), 50 (2), 40 (3)

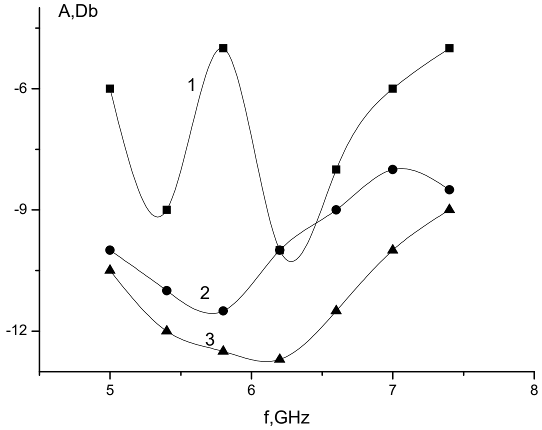

Fig. 8. EMW absorption ability of the composites based on epoxy resin and binary fillers for following proportions graphite/ferrite of the filler concentrations (in wt%): 15/35 (1); 30/20 (2); 25/25 (3)

3.4. Absorption of EMW by the package of the absorbing films

From a practical point of view, it is important a definition of the EMW absorbing properties of the sandwich type packets constructed from the absorbing films with different types of the fillers and their concentrations. The testing of such sandwiches was conducted on the films packets contained three different films (both different concentrations of one type filler and different concentration of these fillers) with one and same thickness.

On the Fig. 9 it is shown the schematic picture of different sandwiches, each of which contains three different films (thickness 1 mm) located differently relative to each other. experiment on revealing of the EMW absorption properties shows that the best result achieves for sandwich, in which the films are located in order of ladder like increasing of the filler concentration if the EMW is falling from film with lowest concentration of filler and vice versa at falling of EMW from reverse side of the same sandwich the result is worse than all. These results may be described as follows.

It is known [4] that protecting from EMW coatings are characterized with good absorbing properties if it microstructure contains the absorbing fillers displaced in polymer matrix with gradient of particles distribution in perpendicular to the absorber surface direction. It must be noted that the obtaining of such films is practically difficult for manufacture and consequently expensive. However, there are some methods, by use of which it would be simplify the design of such materials. With this aim it is possibility of obtaining of sandwich type material, made from films with gradation of distribution of filler particles. The idea, which was realized by us partially coincides with one expressed by German scientist Yauman in the middle years of XX century. for the submarines. The thickness of experimental installation of this scientist was about 10 cm. Such construction could be used on submarines, but not avia-cosmic fly apparatus. Recently it was obtained by us the absorbers as sandwich made from thin absorbers as package of the thin films – composites with different type and distribution of absorbing filler. On the scheme presented in the Fig. 9 there are presented the packages, each of which contains 3 films with different types and concentrations of the filler. Thickness of full package was about 1 mm. The testify shows that from these packages the one with gradual increase of filler concentration in the row of the films possesses higher coefficient of EMW absorption if the wave falls from the film with less contenting of the filler. Such distribution of the films in the package is right on the basis of following considerations: EMW after falling on the film with low concentration of the filler particles will pass all the film with minimal losses of energy and with some derivation from start direction. After the entrance to the second film contenting the filler with more high concentration the EMW will pass all this film with energy losses higher than in first film and more derivation from initial direction. This tendency of the EMW will by increased at passing through the third film, after which it will reach to metal surface of the aircraft, reflected from which it will pass the package in reverse direction, although this EMW will be very week in comparison with initial one and deviated from start direction. The packages with other distribution of the films are less effective than that described above.

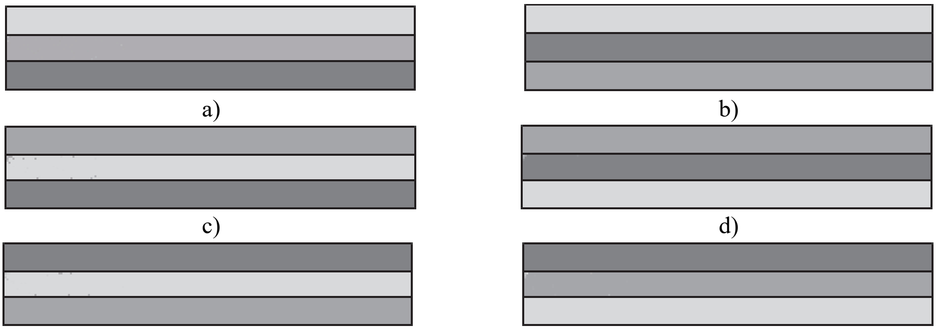
a) b) c) d) e) f)

Fig. 9. Schema of sandwiches with variation of dislocation of the absorber films.
Rectangle with light color corresponds to films with relatively low filler concentration,
semi dark to middle and dark – high concentration of filler

On the Table 1 there are given the numerical data of the EMW absorption (in %) by packages with three different distributions of the films.

Analogical dependences at frequencies 5.6 GHz are presented on the Table 2.

In accordance with the Table 2 data the maximal absorption shows the package with index A, on which the wave falls from left side. The gradation of the absorption value presented in the Table 1 is determined by following terms. In the first sample (package A) the wave will pass relatively “easy” the package firstly through the plate with less content of the filler because of low concentration of one (the processes of the wave absorption-reflection processes are relatively weak). The passing of the waves through the second plate, containing more (in comparison with first plate) concentration of the graphite will absorb more amount of the EMW energy. The passing of EMW through the third plate will be characterized with more intensive absorption-reflection properties than previous plates. The waves falling on the metal surface (after passing through the third plate) reflects with weakened energy from last and undergoes to repeated absorption-reflection processes and therefore the energy of the waves exited from package will be essentially lower than that falling initially on the package. In case of wave falling on the package from the reverse side the energy of waves exited from the package is more than in first case because in the second case the wave falling on the third plate (with relatively high concentration of the filler) reflects from it more intensively and therefore the part of absorbed energy is much less than in first case.

Table 1. EMW absorption by sandwiches designed from films on the basis of epoxy resin and graphite with different concentration of latter ($f = 8.0$ GHz)

#	Position of films	Absorption of EMW, %
1	1-2-3	84.4
2	1-3-2	67.7
3	2-1-3	53.3
4	2-3-1	55.2
5	3-1-2	65.6
6	3-2-1	61.3
Film 1: Epoxy resin (80 Wt.%) + graphite (20 Wt.%) Film 2: Epoxy resin (70 Wt.%) + graphite (30 Wt.%) Film 3: Epoxy resin (60 Wt.%) + graphite (40 Wt.%)		

Table 2. EMW absorption ability of the sandwich type absorbers ($f = 5.6$ GHz). The sequence of the plates in the package (concentration of graphite in the plates) (the wave falls on the package from left side-plate with less content of the filler)

Packing index	Position of films	Absorption of EMW, %
A	30-40-50	54.6
B	30-50-40	49.3
C	40-30-50	44.5
D	40-50-30	41.8
E	50-30-40	38.4
F	50-40-30	37.5

3.5. Effect of samples geometrical sizes on the absorption of EMW

There were conducted the experiments on the samples obtained with use the following way: from the fluoroplast sheet (thickness 3 mm) it was obtained the plates with sizes 70×50 mm. In these plates the holes with different profiles were made, which after were filled with composition material (epoxy glue + 50 wt% graphite) for hardening. Vertical section of this sample is shown on the Fig. 10 (top scheme corresponds to cylindrical holes, middle-conical and bottom-ladder like).

The experimental data of Table 3 allow make the conclusion that the absorption capability of the cover-protector can be regulated by change of configuration of the composite materials placed in the dielectric cover.

Table 3. The absorption capability of the composites displaced in the holes with different profiles

#	Vertical section profile of the sample	Absorption of EMW, %
1	Cylindrical	84
2	Conical	91
3	Ladder like	78

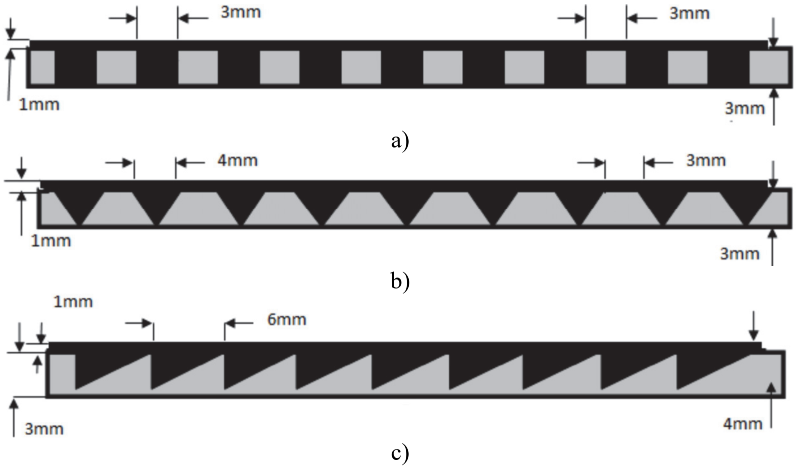

Fig. 10. Vertical sections of the forms with different shapes: cylindrical; b) conical; c) ladder like. Black area – absorbent material, light color area – dielectric substrate (Teflon)

3.6. Effect of binary fillers in the EMW absorbing properties of polymer composites

Investigation of the EMW absorption properties of the polymer composites containing of binary fillers present a definite interest because of here is the possibility of appearing of so called synergistic effect of fillers – non-additive enhancing of some physical/chemical properties at definite proportion of the ingredients in the fillers. The composites based on epoxy glue containing of binary fillers (graphite + carbon black; graphite + ferrite; ferrite + carbon black) were used for investigation of their EMW absorbing properties. On the Figs. 11-13 it is shown the dependence of the EMW (10 GHz) absorption on the proportion of the components in binary fillers. From these dependences it is clear that the absorption of EMW in binary systems one of the important meaning has the proportion of the ingredients in composite materials. It may by proposed that binary filler promotes to creation of resonance microstructures with different volumes, which will be the basis of formation of interference-diffraction phenomena and enhancing of EMW respectively. These proportions promote to synergistic effect noted above, in this case – maximal absorption of EMW, which is unattainable at using of only one filler with any concentrations.

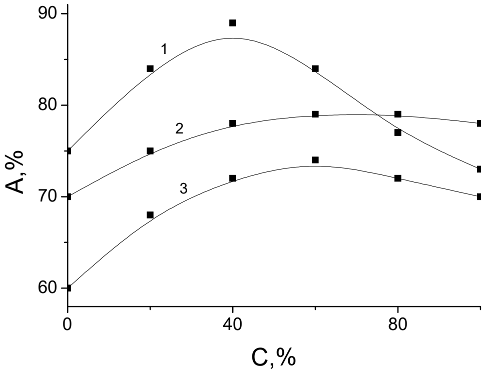

Fig. 11. Dependence of the EMW absorbing level on the proportion of fillers graphite/ ferrite in the composite based on epoxy glue. On the x-axes – the concentration of graphite in binary fillers for total concentration of fillers 50 (1), 40 (2) and 30 wt% (3)

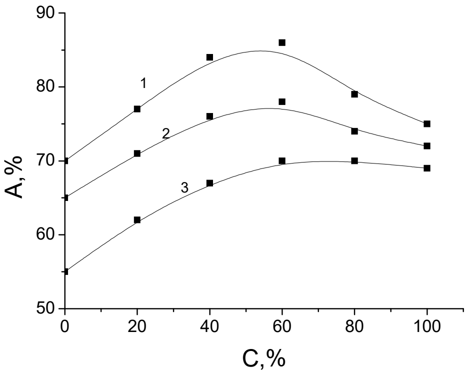

Fig. 12. Dependence of the EMW absorption on the proportion of ingredients of binary fillers in the composite based on epoxy glue and binary filler (graphite/ carbon black) for total concentrations of filler in the composites 40 (1), 50 (2) and 30 wt% (3); on the x-axis – the concentration of the graphite in binary filler

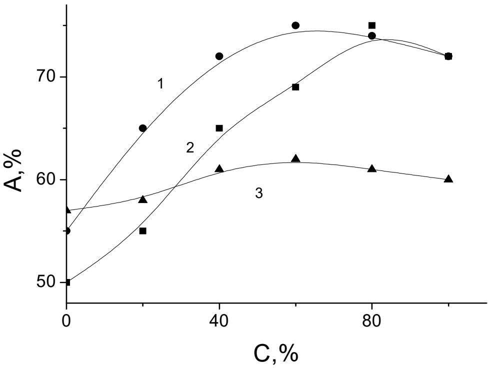

Fig. 13. Dependence of EMW absorbing processes in composites based on silicon rubber with binary filler (ferrite/carbon black) on the content of fillers at their total concentrations 30 (1), 40 (2) and 50 wt% (3); on the x-axis – the concentration of the ferrite in binary filler

3.7. EMW absorption capability of the composites modified with constant electric and magnetic fields

The composites with two types of the filler were selected as the research objects: natural graphite and ferrite. These materials were tested on the EMW absorption capability for study of the electric and magnetic field effect during hardening of the composites. The results of testify are presented on the Fig. 14.

From the Fig. 14 one can see that the absorption capability of the both composites increases at increasing of the electric field during process of composite hardening up to definite level, after which stopped and transacted to the saturation state. The composite in labile state creates the favorable medium for the molecular polarization, which leads to orientation of molecules. The filler particles, which are interacted with lasts receive the orderly state respectively, decrease the entropy of the system and increase the order of the particles in polymer matrix. It is one from suitable conditions for increasing of EMW absorption. It is difficult to say that at higher electric field absorption would be high, because saturation of the corresponding curve gives an opposite result. At very high fields the dielectric it will be expected a breakthrough in the dielectric, in result of which the irreversible structural transformations can be occurred.

Experiments on definition of the effect of the magnetic field were conducted on the composites based on epoxy resin and synthetic graphite and cobalt. To testify the following samples were underwent: 1) epoxy resin + graphite (35 wt%), epoxy resin + cobalt (35 wt%). These composites were obtained at hardening of composites in the constant magnetic fields from the range 0.1-0.6 Tesla. On the Fig. 15 there are presented the dependences of EMW absorption of the level of “technological” magnetic field for both composites.

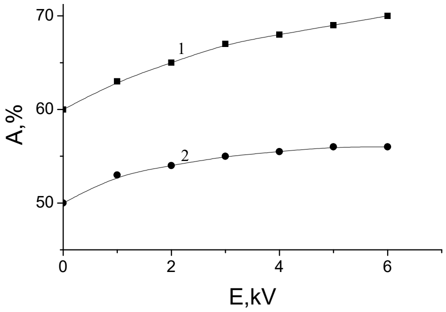

Fig. 14. Dependence of the EMW absorption on the “technological” electric field for composites based on epoxy glue with natural graphite (1) and ferrite (2) at filler concentration in samples 60 wt%

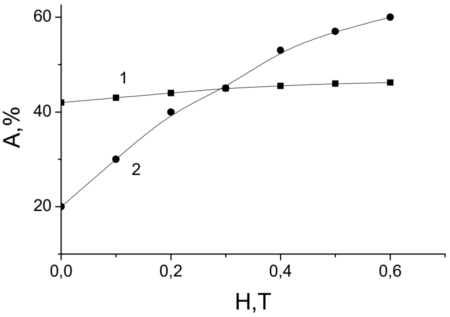

Fig. 15. Dependence of EMW absorption level on the “technological” magnetic field for the epoxy-composites containing a graphite (40 wt%) (1) and cobalt (40 wt%)

As in case of composites underwent to electric field, it must be foreseen the orientation role of the magnetic field. It is clear that this effect will be effective for system including the magnetic particles. From the curves presented on the Fig. 15 one can see that the magnetic field effect is more significant for the system including ferromagnetic particles than for the system including diamagnetic ones.

4. Conclusions

It is shown experimentally that the reception of composites and their obtaining methods are the main factors, variation of which gives the possibility of regulation of their character of EMW absorption. The dependence of the absorption of EMW (3 GHz) energy by polymer composites on the concentration of the fillers (electric conducting or ferromagnetic particles) is extreme – has a maximums at definite concentrations and type of lasts. Composites containing graphite and ferrite filler with definite proportion are characterized with synergistic effect. It is established also that the higher is the homogeneity of the degree of particles distribution in the polymer matrix the higher is the EMW absorption level, which is due to exist of resonance structure of the noted particles in the polymer medium. The composites EMW absorption may be regulated also by their hardening under conditions of the strong constant electric and magnetic fields. Increasing of the absorption of EMW by polymer composites can be reached with use of package of thin layers, in which the type, composition and order of distribution of lasts change in perpendicular to the film plane. One of the ways of change of the absorption of EMW by composites is also the regulation of the layers surface form. It is established that the absorption of the plate covered with low height conical holes and filled with investigated composite is essentially higher than the analogical material covered with holes with other (cylindrical or ladder-like) profiles.

References

[1] **Lagarkov A. N., Pogosian M. A.** Fundamental and applied problems of stels-technologies. Proceedings of Russian Academy of Sciences, Vol. 73, Issue 9, 2003, p. 848, (in Russian).

[2] **Bochkarev A. M., Dolgov M. N.** Radiolocation of the fly apparatus. Foreign Radioelectronics, Vol. 2, 1989, p. 3-17, (in Russian).

[3] **Finkelstein M. I.** Principles of Radiolocation. Guid Book for High Schools. 2nd Edition. Radio and Communications, 1983, (in Russian).

[4] **Aneli J. N., Khananashvili L. M., Zaikov G. E.** Structuring and Conductivity of Polymer Composites. Nova Science Publishers, New York, 1998, p. 326.

[5] **Schnabel W.** Polymers and Electromagnetic Radiation: Fundamentals and Practical Applications, Wiley, 2014, p. 360.

[6] **Volkov V. P., Zelenetsky A., et al.** Synthesis and properties of electromagnetic wave shielding polymer materials with low flammability. Journal of Applied Polymer Science, Vol. 116, Issue 5, 2010, p. 2775-2782.

[7] **Batrakov K., Kuzhir P., Maksimenko S., et al.** Flexible Transparent Graphene/Polymer Multilayers for Efficient Electromagnetic Field Absorption. Scientific Reports, Vol. 4, 2014, p. 231.

[8] **Roberts J. A., Imholt T., Ye Z., et al.** Electromagnetic wave properties of polymer blends of single wall carbon nanotubes using a resonant microwave cavity as a probe. Journal of Applied Physics, Vol. 95, Issue 8, 2004, p. 4352.

[9] **Dosoudil R., Franek J., Slama J.** Electromagnetic wave absorption performances of metal alloy/spinel. IEEE Transactions on Magnetics, Vol. 48, Issue 4, 2012, p. 1524-1527.

[10] **Folgueras L. de Castro, Rezende Mirabel C.** Multilayer radar absorbing material processing by using polymeric nonwoven and conducting polymer. Materials Research, Vol. 11, Issue 3, 2008, p. 245-249.

[11] **Bregar V. B.** Advantages of ferromagnetic nanoparticle composites in microwave absorbers. IEEE Transactions on Magnetic, Vol. 40, Issue 3, 2004, p. 1679-1684.

[12] **Bhavsar V., Tripathi D.** Advance in electronic and electronic engineering. Research India Publications, Vol. 4, Issue 4, 2014, p. 417-424.

[13] **Huang J. C.** Carbon black filled conducting polymers and polymer. Advances in Polymer Technology, Vol. 21, 2002, p. 299.

[14] **Clingerman M. L., Weber, King J. A.** Synergistic effect of carbon fillers in electrically conductive nylon. Polymer Composites, Vol. 23, Issue 5, 2002, p. 911-924.

[15] **Rohde Ulrich L., Newkirk David P.** EMW Circuit Design for Wireless Applications. Wiley, 2004.

[16] **Keith M., Janda B., King J., Perger F., Oxby T.** Polymer matrix composites. for EMI shielding applications. Polymer Composites, Vol. 26, 2005, p. 671-678.

Tamaz Natriashvili received Ph.D. degree in machine technology from Georgian Technical University, Tbilisi, Georgia in 2003. Now he works as director of the Institute of Machine Mechanics. His current research interests include technical novelties in the field of automobile engines.

Jimsher Aneli received Ph.D. degree in chemical technology from Georgian Technical University, Tbilisi, Georgia in 1995. Now he works at the Institute of Machine Mechanics in Tbilisi, Georgia. His current research interests include technical novelties in the field of technical application of polymer composites.

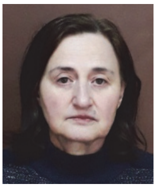

Lana Shamanauri received Ph.D. degree in chemical technology from Georgian Technical University, Tbilisi, Georgia in 2009. Now she works at the Institute of Machine Mechanics in Tbilisi, Georgia. His current research interests include Technical application of polymer composite materials.

4.4. Studying of the seawater drops properties on superhydrophobic surface

Tatiana Popova[1], **Aleksei Ukolov**[2]
Kerch State Marine Technological University, Kerch, Crimea
E-mail: [1]*tanap178@gmail.com*, [2]*ukolov_aleksei@mail.ru*

Abstract. Superhydrophobic properties of the surface lead to the effect of non-wetting the liquid of a solid and the formation of a contact angle close to 180°. The nature of this phenomenon is explained by the features of the surface microrelief having an ordered texture consisting of microprotrusions of the cavity between which they are filled with gas. This phenomenon is widely studied and has already found its use in various practical applications where it is important that the liquid does not interact completely with a solid surface.

In that work we give a brief review of the properties of superhydrophobic surfaces and the directions of their use. The well-known methods are being analyzed for creating a superhydrophobic layer in order to select the optimal method of coating deposition, on materials in contact with the sea environment.

The results of a study of the drops of natural sea water in the Kerch Strait on the superhydrophobic surface of A40S shipbuilding steel are considered. An experimental setup and a technique for determining the droplet angle in the process of evaporation from a superhydrophobic surface are described. An analysis of the stability of the superhydrophobic state was performed with a droplet volume decrease and increase in the concentration of salt in the liquid. The influence of the force of gravity on the drops shape is estimated.

It is shown that in the evaporation process the contact angle decreases, but before the crystallization process begins, it exceeds 150°, thereby maintaining superhydrophobic properties of the surface. Completion of evaporation of the droplet is accompanied by the formation of a solid NaCl crystal, which is certainly an advantage when removing such impurities from the steel surface. In addition, such an effect will not cause degradation of the microstructure of the surface, its contamination with fine crystals, and block the gas channels providing superhydrophobic properties.

The behavior of seawater drops on the superhydrophobic surface differs from the properties of distilled water. While evaporating, the salt concentration enlarges, increasing the specific gravity of the solution. Thus, there is no significant advantage of the surface tension force with respect to the gravitational pull. This phenomenon involves the deviation of the drop's shape from the spherical in the process of evaporation, up to the point of time corresponding to the onset of crystallization of the salt and further distortion of the droplet surface.

The obtained results contribute to the further research of the properties of superhydrophobic coatings and expand the possibilities of their use in shipbuilding.

Keywords: wetting, superhydrophobic surface, surface tension, shipbuilding steel, contact angle, seawater drop.

1. Introduction

In the 90s of the last century, the German botanist Wilhelm Barthlott explained the appearance of the "lotus effect" – the phenomenon of low water wetting of the surface of leaves and petals of plants (Fig. 1), insect claws (Fig. 2), etc. The botanist associated this effect with the features of microstructure of surfaces interacting with water.

The microstructure of non-wetting surfaces has many microprotrusions or microvilli that reduce the interaction forces between the molecules of the liquid and the surface. This feature leads to the fact that on the surface the liquid forms globular droplets spontaneously rolling down from it (Fig. 1), collecting dust and some contaminants, thereby creating a self-cleaning effect. Thus, the "lotus effect" in nature acts as a "protector" of plants against microorganisms, fungal diseases, algae fouling, etc. In the case of a Gerridae, microvilli, creating non-wetting between the legs of the insect and the surface of the water (Fig. 2), facilitate smooth sliding along its surface. It should be noted that the surface of the wings of many other insects, butterflies have a similar structure. Not getting wet, insects do not lose the ability to fly. Subsequently, water-repellent surfaces were called superhydrophobic.

Fig. 1. Drops of water on top of the Geranium leaves

Fig. 2. Insect Gerridae on top of the water surface

The examined properties of plant and insect surfaces led to the search for functionally different superhydrophobic materials [1-3], which can be used in technology: to prevent fouling and sedimentation [4], to obtain water repellent, self-cleaning surfaces [5], reduce friction of fluid flow and increase thermal conductivity [6], in the electric power industry [7], and etc. Teflon surfaces have already become famous for having superhydrophobic properties and are being used in everyday life and production [8].

Superhydrophobic properties of surfaces depend on the characteristics, micro/nanorelief, surface energy and chemical composition of the surface substance.

To key factors affecting superhydrophobicity of the surface, X. Yao, Y. L. Song, L. Jiang include micro/nanostructures, hierarchical structures, low surface energy coatings that provide a large surface-to-volume ratio of the microfluidic device, which affects behavior and significantly increases the pressure loss of the flow to the superhydrophobic surface.

These factors are used in the manufacture of superhydrophobic surfaces on various substrates of metal, which are gradually applied in industry and everyday life [9]. So, N. Rungraeng, Y.-C. Cho, S. H. Yoon, and S. Jun have shown that plate heat exchangers with superhydrophobic surfaces can effectively prevent contamination and reduce heat transfer during the pasteurization process [10].

It is known that the effectiveness of solar panels and wind generators working in severe weather conditions is drastically reduced by the accumulation of ice and snow. Methods of removing ice from surfaces can be divided into two categories: active and passive. The active method includes thermal procedures, mechanical scraping and the use of anti-ice chemical reagents. R. Carriveau, F. Cucchiella, A. Edrisy and others consider a passive method that makes it easy to remove ice by reducing the surface energy and low adhesion strength [11, 12].

The passive method has a huge potential for use – airplanes, wind turbines, photoelectric devices, power lines. Using a metal surface with a superhydrophobic coating will make it possible to detach the condensed droplets from the cooled surface even under the action of gravity.

Superhydrophobic surfaces show excellent characteristics that can be used in hydrodynamics, heat engineering, power engineering, electrical and telecommunications. They have a huge potential for use, their efficiency significantly exceeds their production costs as the price of chemical reagents is not high and the methods of manufacturing such surfaces are relatively simple. After the organization of a large-scale production of water-repellent surfaces, an economic effect can be obtained.

Despite the fact that the study and production of superhydrophobic surfaces over the past fifteen years have achieved great success, many problems associated with achieving real technological applications are waiting to be solved.

Studying the properties of superhydrophobic surfaces, we came to the possibility of their application in shipbuilding, as well as in the real operating conditions of vessels in the waters of the Black Sea [13]. We associate our research with this:

– properties of superhydrophobic states,
– interaction of such surfaces with the waters of the Black Sea,
– the development of more simple methods for creating superhydrophobic surfaces.

Our further plans lie in the direction of checking the reliability of surfaces under pressure, wear, friction, immersion, pollution and under other conditions.

2. Main text

The liquid practically does not wet superhydrophobic surfaces because of the special relief of these coatings. On a hard surface, there are irregularities (cavities, microprotrusions, villi) filled with air. A drop of liquid, falling on such a surface, does not penetrate into the irregularities as a result of air entrapment by microscopic irregularities.

2.1. Contact angle

The phenomena of wetting and non-wetting by liquid surfaces are characterized by the angle of contact (the contact angle), determining its hydrophilic or hydrophobic properties. A liquid with a hydrophilic surface forms a contact angle of less than 90° (Fig. 3), with a hydrophobic angle of more than 90° (Fig. 4). Surfaces having a contact angle with a fluid angle of more than 150° are called superhydrophobic (Fig. 5).

In 1805, Thomas Young was the first who described the concepts of contact angle and wetting. During the next two centuries, many researchers conducted theoretical studies and developed analytical methods for studying the properties of this phenomenon.

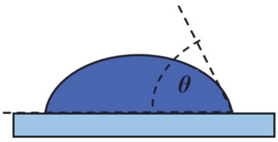

Fig. 3. Hydrophilic surface, $\theta < 90°$

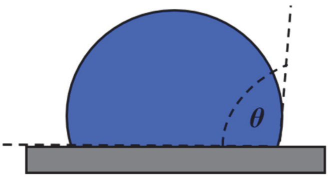

Fig. 4. Hydrophobic Surface, $\theta > 90°$

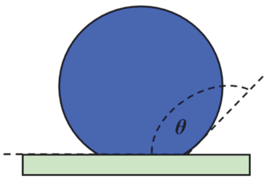

Fig. 5. Superhydrophobic surface, $\theta > 150°$

Scientists have demonstrated the various intermolecular interactions between a liquid and a solid material lead to different wetting properties [14]. Significant progress was made in studying the relationship between roughness and hydrophobicity, observing the hysteresis of the contact angle (the difference between the contact angle on the horizontal surface and the slanting), the discovery of superhydrophobicity induced by the micro- and nanoscale hierarchy [1].

The contact angle is the main index used to estimate the wetting of a solid surface. It usually characterizes the behavior of a liquid drop on a solid surface in the air and is determined by the angle between the tangent at the three-phase point and the solid surface. The relationship between the contact angle and the surface tension coefficients of interface boundaries can be described by the Young's equation:

$$\gamma_{SG} - \gamma_{SL} - \gamma_{LG}\cos\theta_c = 0, \tag{1}$$

where θ_c – contact angle, γ_{SG} , γ_{SL} and γ_{LG} – surface tension coefficients of the solid/gas boundary, solid/liquid, and liquid/gas, respectively.

Methods for measuring the contact angle, can be grouped into methods of tensiometry and goniometry.

Tensiometry methods determine the value of the contact angle using the Young Eq. (1). If the coefficients of the surface tension of the interphase boundaries do not change, the contact angle is constant and can be found from Eq. (1). Problems in measuring the edge by this method appear: first, if the values of the surface tension coefficients are unknown, secondly, impurities, the adsorption of the vapor on the solid phase, the electrostatic potential, the surface roughness, heterogeneity and external forces lead to a change in the apparent contact angle θ_c.

In the methods of goniometry, the contact angle is observed and measured from the two-dimensional image of drops on a solid surface (Figs. 3-5).

Modern methods for measuring the contact angle of droplets, described in the literature, can be divided into two groups: analytical and exclusively image processing methods. Analytical methods require some fluid properties (for example, the surface tension coefficient) to determine the contact angle and usually cannot measure the contact angle of asymmetric drops (for example, drops on inclined surfaces). Image processing methods do not have this limitation, so they are related to common methods. But these and other methods contribute to a deeper study of the properties of superhydrophobic surfaces.

2.2. Wentzel's and Cassie-Baxter's states

Unevenness on superhydrophobic surfaces can both be filled with liquid partially, and not penetrate into the irregularities at all. In these cases, two states of water droplets on a solid surface are distinguished: the Wentzel's state (Fig. 6) and the Cassie-Baxter's state (Fig. 7), as it is detailed in work [7].

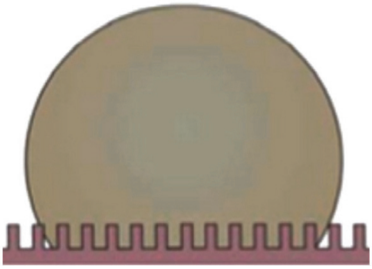

Fig. 6. Wentzel's state [7]

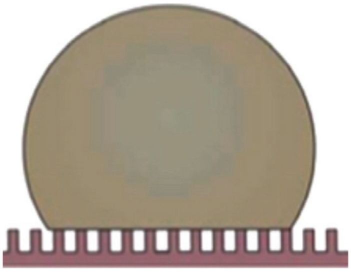

Fig. 7. Cassie-Baxter's state [7]

In the Wentzel's state, water penetrates into the structured surface, the droplets become spiked, which prevents them from slipping easily. In the Cassie-Baxter state, the liquid lies on top of a structured surface with a gas layer (as in the case of Insect Gerridae). This gas gap is an effective boundary that ensures the glide of the droplet at the liquid-gas interface.

The nature of a solid superhydrophobic surface is explained by the influence of its roughness on a drop of liquid. The wettability phenomenon of a solid surface can be interpreted using the Wenzel's and Cassie-Baxter's models (Figs. 6, 7).

Assuming that the liquid fills the space between the protrusions on the surface (Fig. 6), the Wenzel approach correlates with the apparent contact angle θ' and the thermodynamic contact angle θ as:

$$\cos\theta' = r\cos\theta, \quad (2)$$

where r is the coefficient of roughness, which determines the ratio between the true surface area and its horizontal projection. When one of the values (θ', θ, r) changes, a regular change (decrease or increase) of the others occurs.

Cassie and Baxter put forward the idea that the surface captures air in hollow spaces of roughness (Fig. 7), identifying $\cos\theta'$ of the apparent angle's contact θ' on the superhydrophobic surface as follows:

$$\cos\theta' = f_{LS}\cos\theta - f_{LV}, \tag{3}$$

where f_{LS} – the proportion of the area of the liquid which is in contact with the solid, f_{LV} – the proportion of the area of the liquid which is in contact with trapped air. Wherein:

$$f_{LS} + f_{LV} = 1. \tag{4}$$

Thus, the hysteresis of the contact angle can distinguish two states. With greater hysteresis, the droplets will be considered to belong to the Wenzel’s solution entering the surface grooves. Whereas with lower hysteresis values, the surface can be considered as a columnar structure supporting the fluid and decreasing the available area.

Since superhydrophobicity mainly arises from the air trapped in the grooves by a solid surface or coating, the presence of its volumes of very small nanoscopic scales (nanobubbles) is the subject of a wide range of interpretations and observations. Despite the existence of nanobubbles on hydrophobic surfaces, discussions still occur, where the authors compare conflicting results, and also study the properties of nanobubbles (V. Graig, X. Zhang, J. Hu [15]). Theoretically, such bubbles should dissolve under the action of their internal pressure for a short time, but experimentally with the help of a highly sensitive surface method of atomic force microscopy, unusual peculiar properties and forms of nanobubbles are found.

We have developed a technique for performing experimental studies to determine the contact angle of water droplets on the natural, polished and superhydrophobic surface of A40S (8×90×50 mm) ship steel using an installation that will be described later.

2.3. Mechanical properties of steel grades A40S

Steel grade A40S has high strength and ductility. It is intended for the manufacture of hulls or other welding constructions of ships and floating structures. The chemical composition of steel grade A40S is presented in Table 1.

Mechanical properties of steel grade A40S at t =20 °C: short-term strength limit 530-690 MPa, yield stress for permanent deformation 390 MPa, elongation at break 19 %.

Table 1. Chemical composition of steel A40S in shares

Grade	C, not more than	M_n	S_i	P and S, not more than	C_r	N_i	C_u	A_l
A40S	0.12	0.5-0.8	0.8-1.1	0.035	0.6-0.9	0.5-0.8	0.4-0.6	0.015-0.06

Fig. 8. Surface of experimental samples after rolling

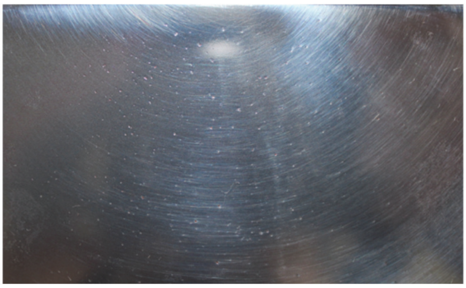

Fig. 9. Surface of experimental samples after polishing

The surface of the samples (Fig. 8) was previously ground with a decrease in the grain size of the abrasive. Final mechanical polishing was carried out with a solution of chromium dioxide Cr_2O_3 in pure kerosene, until reaching a mirror surface (Fig. 9).

The quality of the prepared surface is also confirmed by microscopic observations (Figs. 10, 11) using an MBR-1 optical microscope with an OI-18A luminescent illuminator and a Canon EOS550D digital camera conjugated with a microscope.

Despite the presence of processing defects (Fig. 10), the polished surface has a uniform relief compared to the untreated sample (Fig. 11).

Drops of distilled water were applied to a natural (after rolled), polished and superhydrophobic (water repellent) surface.

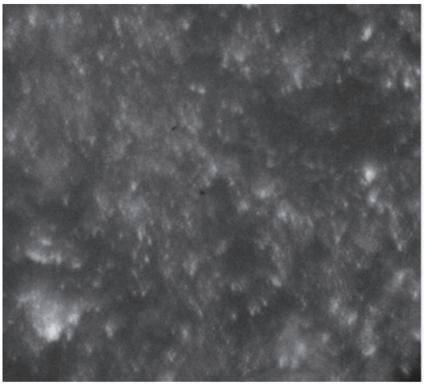

Fig. 10. Microstructure of untreated surface (steel A40S)

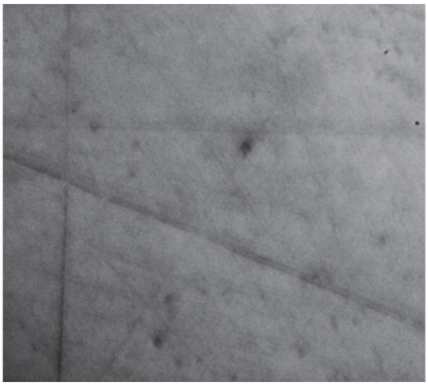

Fig. 11. Microstructure of polished surface (steel A40S)

2.4. Methods for creating superhydrophobic surfaces and choosing the optimal path for this research

Methods for creating superhydrophobic surfaces by processing a material with a low surface energy are mainly one-step processes and have the advantage of ease of implementation. There are many ways to make textured surfaces: mechanical pulling, laser processing and plasma processing, chemical etching, lithography, sol-gel method, layer by layer deposition and colloidal mounting, electrical or chemical reactions.

Chemical precipitation through a surface chemical reaction forms a layer with nanoscale topography, including nano-pins and nano-rods. It is convenient and quite easy to use various methods, including chemical vapor deposition (CVD), which uses a gaseous base to deposit particles or films. One can use chemical bottom desolutions (CBD) and electrochemical deposition (ECD) that use wet chemical solutions or electrochemically conductive substrates to precipitate hard metals and oxides.

We choose chemical vapor deposition (CVD) as a simple way to produce a superhydrophobic surface on a sample of A40S steel.

Superhydrophobicity of the steel surface was created with the help of the easily accessible superhydrophobic system NeverWet Base Coat. This is a new class of coatings, which causes water droplets to form almost ideal spheres, while keeping objects dry and clean.

The water-repellent properties were imparted to the surface by the precipitation of a hydrophobic solution by applying a two-layer coating. The first layer – the base layer – contains methyl isobutyl ketone, butyl acetate and mineral alcohols applied by uniform spraying in 2-3 passes from a distance of about 15 cm for 3-4 seconds. The sample is then left to stand for 30 minutes under normal ambient conditions maintained in the laboratory. The second layer is applied by depositing an upper coating containing silica nanoparticles. For approximately 12 hours, the surface is dried under normal laboratory conditions prior to the experiment and measurement.

2.5. Experimental setting

Observation and photoshooting of the drops were carried out on a specially designed apparatus for determining the contact angle of the droplet (Fig. 12). On the optical bench (1), a specimen holder (2), a light source (3), a collecting lens (4), a digital camera Canon EOS 550D (5), linked to an ACER computer (6) are mounted to receive the image coaxiality. A drop of water after deposition on the surface of a steel sample and optical magnification is fixed by means of a viewfinder in real time by a computer.

The received images were analyzed using the sPlan 7.0 program and the built-in electronic protractor.

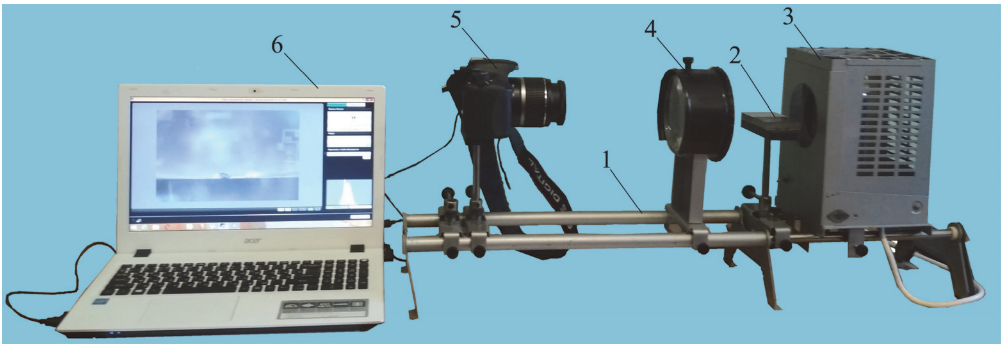

Fig. 12. Experimental setting for determining of the contact angle of the drop

2.6. Results and discussion

The image of water droplets on a natural (after rolled), polished and superhydrophobic surface of A40S steel is shown in the figures below (Figs. 13-15). The determination of the droplet angle by means of a graphical analysis and an electronic protractor showed that its value depends on the quality of the surface treatment. In the presence of a rough relief of the sample after steel rolling, the drop passes into the Wentzel state, which enhances the wetting effect and reduces the contact angle (Fig. 12).

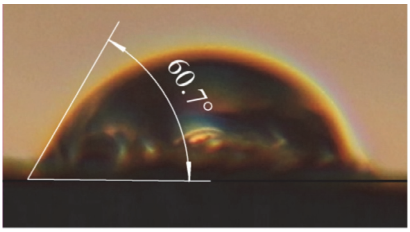

Fig. 13. A drop of water on a natural (after rolled) surface

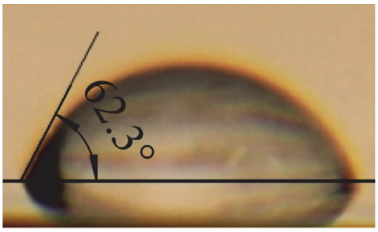

Fig. 14. A drop of water on a polished surface

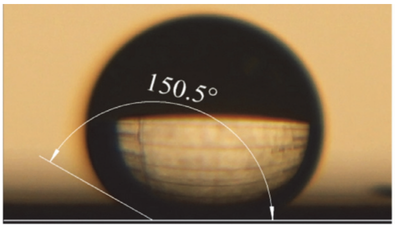

Fig. 15. A drop of water on a superhydrophobic surface

Polishing eliminates the influence of unevenness and leads to an increase in the contact angle (Fig. 14).

The deposition of a microstructured (superhydrophobic) coating causes a transition to the Cassie-Baxter state (Fig. 15). In this state, the liquid lies on top of the structured surface above the gas layer. This gas gap is an effective medium that ensures the glide of the droplet at the liquid-gas interface. The contact angle of the surface obtained exceeds 150°, which is confirmed by its superhydrophobic properties.

The approbation of the method for determining the contact angle on samples of A40S shipbuilding steel using the described installation showed good agreement with the previously used scientific methods.

The superhydrophobic surfaces obtained, the images of drops on the natural (after rolling), polished and superhydrophobic surfaces do not contradict the wetting theory, which makes it possible to find ways to further extend the application of superhydrophobic coatings, including marine technologies.

The change in the angle of contact between the drop and the surfaces is due to their different processing and the presence of a superhydrophobic layer. The transition from the acute contact angle to the blunt angle on the surface of the deposited layer indicates its hydrophobic properties and the presence of the non-wetting effect, in contrast to the untreated and polished samples.

In the course of the subsequent experiment, drops of natural sea water from the Kerch Strait were used, the salinity of which was determined by the salt meter and was 17 ppm (17 g salt/1 kg water).

Precipitation of the drop onto the superhydrophobic surface was carried out by flowing from the tip, which provided a drop of 10^{-8} m^3. Next, there was a photoshooting of the droplets evaporating (Fig. 16) in the laboratory. The interval between shots was reduced from 20 minutes at the beginning of the evaporation process up to 2 minutes at the end of the measurements. The total test time was about 4 hours (Table 2).

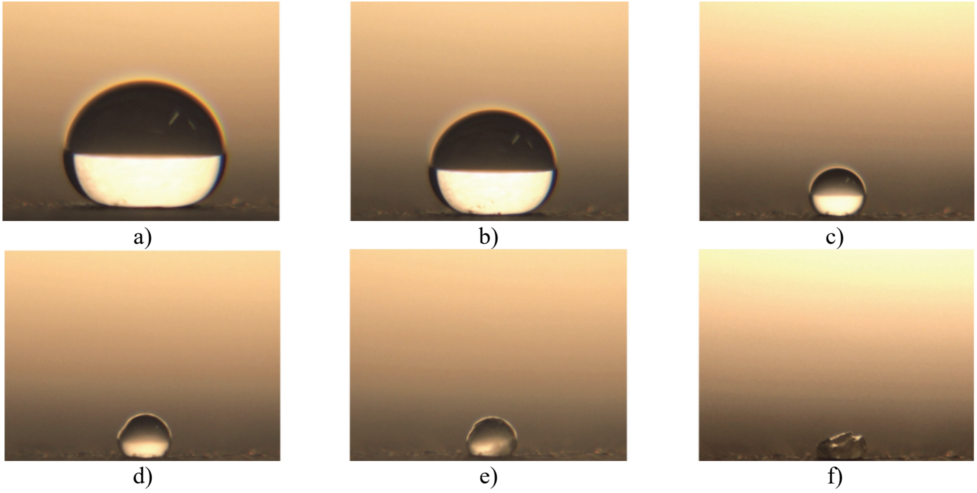
a) b) c)
d) e) f)

Fig. 16. A sea water drop on a superhydrophobic surface during evaporation: a) t = 0 min, b) t = 70 min, c) t = 161 min, d) t = 189 min, e) t = 198 min, f) t = 220 min; image magnification: ×23

Fig. 16 selectively shows the stages of evaporation of a drop of seawater on the superhydrophobic surface of A40S steel. The data of some properties of these droplets are shown in Table 2. Time after the droplet formation (Fig. 16(a)), after 1 hour of evaporation (Fig. 16(b)) and after 3 hours of evaporation (Fig. 15(c)), the drop gradually reduced the linear dimensions, while remaining in this form. After more than 3 hours (Figs. 16(d), 16(e)), a precipitate appears in the droplet, and the shape of the droplet is distorted, especially at the upper part. The process of evaporation of the salt crystal formation is completed (Fig. 16(f)). Attention is drawn to the fact that even with multiple the repetition of such an experiment as a result of the crystallization of the salt from the solution always produces a single, solid fragment of the solid phase. This phenomenon is significantly different from the results of evaporation of a drop of NaCl solution on hydrophilic surfaces, including shipbuilding steels. Under such conditions, a number of individual crystals arise, the size and concentration, which increases closer to the perimeter of the contour of the precipitated drop. On the superhydrophobic surface, the resultant force acting on the impurity will be directed into the droplet during evaporation, which leads to a uniform growth of the crystal during evaporation.

Table 2. Some a sea waters drops properties dependence on the evaporation time

Evaporation time, (min)	Contact angle (°)	Diameter horizontal, d_{hor} (c.u.)	Diameter vertical, d_{ver} (c.u.)	$\frac{d_{hor}}{d_{ver}}$	Radius horizontal, r_{hor} (mm)	Radius vertical, r_{ver} (mm)	Average radius, r_{av}, (mm)	Average volume, V_{av}, (μl)	Quantity of water molecules N_w ($\times 10^{19}$)	Concentration of water molecules, n_w ($\times 10^{28}$ m^{-3})	Concentration of salt molecules, n_s ($\times 10^{27}$ m^{-3})
0	168.0	69.0	54.0	1.278	1.500	1.174	1.337	10.00	33.30	3.32	0.17
28	165.6	63.5	50.7	1.252	1.380	1.102	1.242	8.01	26.60	3.32	0.22
52	165.5	58.4	47.3	1.235	1.270	1.028	1.145	6.35	21.10	3.32	0.28
70	163.4	54.6	44.5	1.270	1.187	0.967	1.077	5.23	17.30	3.31	0.33
94	167.9	49.1	41.1	1.195	1.067	0.893	0.980	3.95	13.00	3.30	0.44
108	162.8	47.5	38.7	1.228	1.033	0.841	0.937	3.44	11.30	3.29	0.51
127	158.9	40.7	35.5	1.146	0.885	0.772	0.828	2.38	7.78	3.27	0.74
150	161.6	35	30.8	1.136	0.760	0.670	0.715	1.53	4.95	3.23	1.14
161	155.1	31.8	28.2	1.128	0.691	0.613	0.652	1.16	3.71	3.19	1.51
188	152.7	24.7	21.2	1.165	0.537	0.461	0.499	0.52	1.56	3.01	3.37
189	154.1	24.1	20.6	1.170	0.524	0.448	0.486	0.48	1.43	2.98	3.64
195	142.9	24.3	20.8	1.168	0.528	0.452	0.491	0.49	1.48	2.99	3.55
198	130.4	23.0	18.8	1.223	0.500	0.409	0.454	0.39	1.14	2.90	4.46
200	135.0	22.8	18.2	1.253	0.496	0.396	0.446	0.37	1.06	2.87	4.72
202	135.0	21.7	17.2	1.262	0.472	0.374	0.423	0.32	0.88	2.79	5.53
204	137.5	21.6	16.5	1.309	0.470	0.359	0.414	0.30	0.82	2.76	5.88
206	136.0	21.1	15.8	1.335	0.459	0.343	0.401	0.27	0.73	2.70	6.48
208	142.9	20.7	14.7	1.408	0.450	0.320	0.385	0.24	0.62	2.61	7.34
210	142.6	20.8	14.2	1.465	0.452	0.309	0.380	0.23	0.60	2.59	7.60
213	135.0	20.7	13.2	1.568	0.450	0.287	0.368	0.21	0.53	2.51	8.35
216	145.0	21.2	11.5	1.843	0.461	0.250	0.355	0.191	0.45	2.41	9.31
220	137.5	21.2	10.9	1.945	0.461	0.237	0.349	0.18	0.42	2.36	9.84
223	135.0	21.2	11.1	1.910	0.461	0.241	0.351	0.18	0.43	2.38	9.66
226	139.5	21.4	11.1	1.928	0.465	0.241	0.353	0.18	0.44	2.40	9.48

The stability of the hydrophobic state of a drop of seawater on a structured surface was studied by measuring the contact angle (Table 2) for each observation stage. The graph of the variation of the contact angle versus the evaporation time is shown in Fig. 17.

Contact angle is defined by equation:

$$\cos\theta_C = \frac{\gamma_{SG} - \gamma_{SL}}{\gamma_{LG}}, \tag{5}$$

where θ_C – contact angle, γ_{SG}, γ_{SL} and γ_{LG} – surface tension coefficients of the solid/gas boundary, solid/liquid, and liquid/gas, respectively.

Despite the increase in salt concentration due to evaporation of water, the contact angle at the initial stage varies slightly (150° < θ_C < 168°), thus maintaining the superhydrophobic state of the drop.

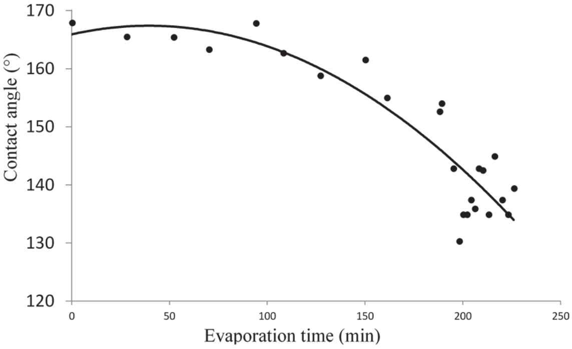

Fig. 17. The graph of the contact angles and evaporation times dependence

After 3 hours of testing, the value of the contact angle decreases. However, this evaporation stage already corresponds to the distortion of the drop-shaped form (Figs. 16(d), 16(e)), which indicates the onset of crystallization of the NaCl-salt, which undoubtedly introduces a change in Eq. (5).

Approximately, the dependence of the surface tension γ_{LG} on the temperature T, the fluid density ρ, and the molar mass μ of the substance is expressed by the equality:

$$\gamma_{LG} = B(T_k - T - \tau) \cdot \left(\frac{\rho}{\mu}\right)^{\frac{2}{3}}, \tag{6}$$

where B – a constant coefficient, T_k – the critical temperature, and τ – the magnitude of the temperature dimension. Under the isothermal conditions of the experiment, the main contribution to the change in γ_{LG} will be made by the factor ρ/μ Eq. (6), which in turn can be represented for a mixture of substances:

$$\frac{\rho}{\mu} = \frac{m(\nu_1 + \nu_2)}{Vm} = \frac{n_1 + n_2}{N_A}, \tag{7}$$

where m – the mixture weight, V – the drop volume, ν – the amount of the substance, n – the concentration of the components, and N_A – the Avogadro number. At the initial stage of the experiment, the ratio $(n_1)/(n_2) \approx 10^2$ and the value of the ratio Eq. (7) is mainly determined by the number of water molecules in the droplet volume. Evaporation of water leads to a decrease in its concentration and an increase in the concentration of salt in the drop. Decay n_1 occurs faster than n_2, which in time leads to an increase in their sum, and consequently to a decrease in θ_C Eq. (1). At the end of evaporation, $n_1 \approx 0$, while the calculated value of $n_2 = 2 \cdot 10^{28}$ m^{-3} coincides with the concentration of molecules in the NaCl crystal.

In most cases, in the studies of droplets on a superhydrophobic surface, accurate analysis of the contact angle is made difficult by distortion of their shape due to gravity. According to the research [16], the droplet volume should be within 0.5-10 μl. In general, the use of small droplets avoids the deformation of water droplets caused by gravity. However, due to the lack of proper wetting of the superhydrophobic surface, it is very difficult to create drops of water with a volume of less than 4 μl on them.

In the general case, while studying liquid droplets, the actions of capillary (σL) and gravitational ($g\rho L^3$) forces are compared, calculating the Bond's number (Eötvös number) by the formula:

$$B_0 = \frac{\rho g L^2}{\gamma}, \tag{8}$$

where L – the characteristic size of the liquid drop, for example, the height at its center, γ – the surface tension of the liquid, g – the acceleration due to gravity, ρ – the density of the liquid.

However, the process of evaporation of seawater drop causes variability in the density and surface tension of the liquid, which disrupts the dependence Eq. (8). Therefore, in the given work, to estimate the effect of gravity on the shape of a drop of seawater during evaporation on a superhydrophobic surface, the ratio of the horizontal radius r_{hor} of the droplet to the vertical r_{ver} in the middle section of the drop was calculated. The graph of the relationship (r_{hor}/r_{ver}) versus the evaporation time is shown in Fig. 18.

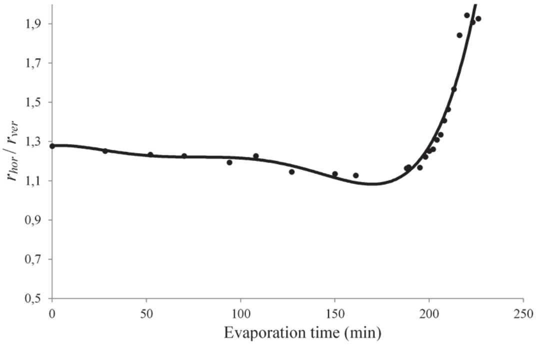

Fig. 18. The graph of the contact angles and r_{hor}/r_{ver} ratios dependence

A new method for measuring the contact angles of superhydrophobic surfaces was proposed in [17]. A 5 µl drop of water was placed on the sample, and the contact angle was measured after the droplet had decreased in volume to 0.3 µl after evaporation for 40 min under ambient conditions.

The initial volume of droplets was $V = 10$ µl, and $r_{hor}/r_{ver} \approx 1.3$. In the process of evaporation, the difference in the radii of the droplet decreases, reaching its minimum at the level of $r_{hor}/r_{ver} \approx 1.16$; volume $V = 0.5$ µl. The minimum deviation from the spherical shape coincides with the onset of the active crystallization of salt in the droplet volume, which leads to an increase in the r_{hor}/r_{ver} ratio and further coarsening of the contour. Further nucleation of the solid phase leads to an even greater discrepancy between the horizontal and vertical radii, but the predominance of salt crystals in the volume no longer makes it possible to determine the resulting formation as a drop.

In the general case, the change in the volume of the droplet from time (Fig. 19), before the onset of the phase transformation, is inversely proportional, the character of which is related to the external conditions of evaporation (humidity, saturated vapor pressure). The onset of the crystallization process is indicated by a decrease in the rate of evaporation and an equalization of the graph of $V = f(t)$ after 190 minutes of testing. At the same time, the concentration of salt in the droplet volume increases sharply (Fig. 20).

The process of phase transition takes about 30 minutes. In this case, the main contribution to volume reduction is made by the vertical component of the linear dimensions of the droplet cross section. The horizontal radius after 190 minutes of evaporation and until the time of full hardening decreases no more than 13 %.

The saturation concentration of NaCl is 35 % and will be achieved when the volume is reduced to 0.2 µl. After that, the horizontal size of the droplet practically remains constant (Table 2), which causes a sharp increase in the r_{hor}/r_{ver} ratio (Fig. 18) and the formation of an elongated crystal on the surface after evaporation of the droplet (Fig. 16(f)).

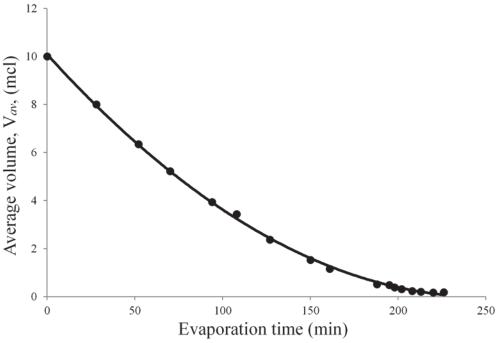

Fig. 19. The graph of the average volume and evaporation time dependence

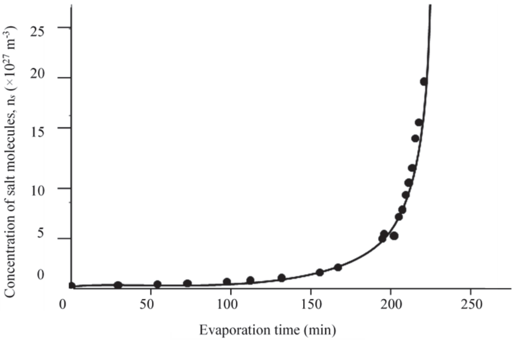

Fig. 20. The graph of the concentration of NaCl molecules and evaporation time dependence

Using the data of Table 2, the concentration of salt in the evaporating drop of sea water was determined by the following method. If we take the salinity of 17 pro mil (the figure characteristic of the Kerch Strait), i.e. in 1 kg of water contains 17 g of NaCl-salt, then the salt concentration is determined by the formula:

$$n_0 = \frac{N}{V} = \frac{m}{m_0 V}, \tag{9}$$

where m = 17 g – mass of salt, m_0 = 58.44 amu molecules NaCl, V = 1, l =10^{-3} m^3 (it is kilo of the substance); and will be equal to:

$$n_0 = \frac{17\cdot10^{-3}}{58.44\cdot1.66\cdot10^{-27}\cdot10^{-3}} = 17.5\cdot10^{25}\ m^{-3}.$$

The number of salt molecules in the drop:

$$N_0 = n_0 \cdot V_0 = 17.5\cdot10^{25}\cdot10^{-8} = 17.5\cdot10^{17},$$

where V_0 = 10^{-8} m^3 – the initial volume of the drop (experimentally determined).

To calculate the water concentration in the drop, the number of molecules in the volume was first determined without the presence of an impurity:

$$N_{0B} = \frac{mN_A}{\mu} = \frac{\rho V N_A}{\mu}, \qquad (10)$$

and subtracted the number of salt molecules:

$$N_B = \frac{\rho V N_A}{\mu} - N_0. \qquad (11)$$

Water molecules concentration:

$$n_B = \frac{N_B}{V}. \qquad (12)$$

NaCl concentration in the crystal was determined theoretically:

$$n' = \frac{\rho_{NaCl}}{m_0} = \frac{2165}{58.44 \cdot 1.66 \cdot 10^{-27}} = 2{,}23 \cdot 10^{28}\ \text{m}^{-3}. \qquad (13)$$

The obtained theoretical data are conformed with our calculations on the experimentally obtained data.

Of course, it is difficult to affirm quantitatively good accuracy on such a scale. However, some qualitative conclusions can be made.

3. Conclusions

The review of the properties and methods of creating superhydrophobic surfaces is aimed at finding possible ways of implementing their various applications in the shipbuilding industry.

The work deals with the conditions of non-wetting by a liquid of hard surfaces, the dependence of the contact angle on the surface type, methods of its calculation or determination. Attention is paid to the physical mechanism of the stable state of Cassie-Baxter with air trapped by the superhydrophobic surface between the drop and its roughness.

A technique for performing experimental studies to determine the contact angle of water droplets on the natural, polished and superhydrophobic surface of A40S steel is developed. The choice of steel-type was since this steel is widely used in the world shipbuilding industry.

Superhydrophobicity of the surface on the steel was achieved by chemical vapor deposition (CVD) using the NeverWet Base Coat superhydrophobic system. The adequacy and correctness of the described and implemented technique for surface preparation and application of the superhydrophobic layer are confirmed by optical observations of water droplets and the drop contact angle analysis.

The scheme of the installation for graphical determination of the contact angle of a liquid drop on the surface of a solid is described. The images were analyzed using sPlan 7.0. The contact angle was measured by the electronic protractor built into the program. The results gave good agreement with previously used scientific methods.

In the experiment, drops of natural sea water (the Kerch Strait) were used. The determination of the contact angle of the drops showed that its value depends on the quality of the surface treatment. In the presence of a rough relief of the sample after steel rolling, the drop passes into the Wentzel’s state, which enhances the wetting effect and reduces the contact angle. The change in the angle of contact between the drop and the surfaces is due to their different processing and the presence of a superhydrophobic layer. The transition from the acute contact angle to the blunt angle on the surface of the deposited layer indicates its hydrophobic properties and the presence of the non-wetting effect, in contrast to the untreated and polished samples.

The obtained superhydrophobic surfaces, the images of drops on the natural (after rolling), polished and superhydrophobic surfaces do not contradict the wetting theory, which makes it possible to search for ways to further extend the use of superhydrophobic coatings, including in marine technologies.

The phenomenon of evaporation of seawater drops was studied. The research of the behavior of natural sea water droplets on the created superhydrophobic surfaces on samples of A40S shipbuilding steel showed that in the process of evaporation the contact angle decreases, but before the crystallization process remains $\theta_C > 150°$, thereby retaining the superhydrophobic properties of the surface. Completion of evaporation of the drop is accompanied by the formation of a solid NaCl crystal, which, of course, facilitates the removal of such impurities from the steel surface. In addition, such an effect will not cause degradation of the microstructure of the surface, its contamination with fine crystals, and block the gas channels providing superhydrophobic properties.

Reducing the volume during evaporation does not completely eliminate the effect of gravity on the shape of the droplet, but reaches its minimum for volumes of 0.5 μl.

Thus, the obtained results contribute to the evaluation of the capabilities of superhydrophobic coatings in interaction with seawater, expand their application for self-cleaning and protection from various natural formations of surfaces of materials used by the marine industry.

The results provide an opportunity to obtain and further study protective coatings for structures and mechanisms used in the marine environment, the performance of which depends on the phenomenon of absolute non-wetting of a solid surface, including shipbuilding steel. It is necessary to conduct a thorough characterization of the mechanical and thermodynamic stability of the superhydrophobic state in real operating conditions. It is important to develop simpler and more standardized methods for creating and verifying the reliability of surfaces under pressure, wear, friction, immersion, pollution and other conditions.

Acknowledgements

This research is supported by the Kerch State Maritime Technological University under the Contract No. AAAA-A18-118021990017-5 with third-party organizations.

References

[1] **Feng Li L. S. H., Li Y. S., et al.** Super-hydrophobic surfaces: from natural to artificial. Advanced Materials, Vol. 14, Issue 24, 2002, p. 1857-1860.

[2] **Zhang Y.-L., Xia H., Kim E., Sun H.-B.** Recent developments in superhydrophobic surfaces with unique structural and functional properties. Soft Matter, Vol. 8, Issue 2, 2012, p. 11217-11231.

[3] **Koch K., Bhushan B., Barthlott W.** Multifunctional surface structures of plants: an inspiration for biomimetics. Progress in Materials Science, Vol. 54, Issue 2, 2009, p. 137-178.

[4] **Barthlott W., Neinhuis C.** Purity of the sacred lotus, or escape from contamination in biological surfaces. Planta, Vol. 202, Issue 1, 1997, p. 1-8.**Neinhuis C., Barthlott W.** Characterization and distribution of waterrepellent, self-cleaning plant surfaces. Annals of Botany, Vol. 79, Issue 6, 1997, p. 667-677.

[6] **Yan Y. Y., Gao N., Barthlott W.** Mimicking natural superhydrophobic surfaces and grasping the wetting process: a review on recent progress in preparing superhydrophobic surfaces. Advances in Colloid and Interface Science, Vol. 169, Issue 2, 2011, p. 80-105.

[7] **Zhang P., Lv F.Y.** A review of the recent advances in superhydrophobic surfaces and the emerging energy-related applications. Energy, Vol. 18, Issue 15, 2015, p. 1068-1087.

[8] **Van der Wal P., Steiner U.** Super-hydrophobic surfaces made from Teflon. Soft Matter, Vol. 3, Issue 4, 2007, p. 426-429.

[9] **Yao X., Song Y. L., Jiang L.** Applications of bio-inspired special wettable surfaces. Advanced Materials, Vol. 23, 2011, p. 719-734.

[10] **Rungraeng N., Cho Y-C., Yoon SH., Jun S.** Carbon nanotubepolytetrafluoroethylene nanocomposite coating for milk fouling reduction in plate heat exchanger. Journal of Food Engineering, Vol. 111, Issue 2, 2012, p. 218-224.

[11] **Carriveau R., Edrisy A., Cadieux P., Mailloux R.** Ice adhesion issues in renewable energy infrastructure. Journal of Adhesion Science and Technology, Vol. 26, Issues 4-5, 2012, p. 447-467.**Cucchiella F., D'Adamo I.** Estimation of the energetic and environmental impacts of a roof-mounted building-integrated photovoltaic systems. Renewable and Sustainable Energy Reviews, Vol. 16, Issue 7, 2012, p. 5245-5259.

[13] **Pridvorov B., Popova T., Ukolov A.** Superhydrophobic surface. Review. Education, Science and Youth. Vol. 2017, Issue 2, 2017, p. 107-120.

[14] **Bin Su, Tian Ye, Jiang Lei** Bioinspired interfaces with superwettability: from materials to chemistry. Journal American Chemical Society, Vol. 138, Issue 6, 2016, p. 1727-1748.

[15] **Craig V., Zhang X., Hu J.** Nanobubbles at Hydrophobic Surfaces. Drops and Bubbles in Contact with Solid Surfaces. CRC Press, United States, 2012, p. 159-174.

[16] **Zhao T., Jiang L.** Contact angle measurement of natural materials Colloids and Surfaces B. Biointerfaces. Vol. 161, 2018, p. 324-330.

[17] **Zhang X., Shi F., Yu X., Liu H., Fu Y., Wang Z., Jiang L., Li X.** Polyelectrolytemultilayer as matrix for electrochemical deposition of gold clusters: towardsuper-hydrophobic surface. Journal American Chemical Society, Vol. 126, 2004, p. 3064-3065.

Tatyana Popova, Professor, Doctor of pedagogical sciences. Received the Doctor in pedagogy in 2011 at the National Pedagogical University after M. P. Dragomanov, Kiev, Ukraine. Now she is the Head of the Department of Mathematics, Physics and Informatics in the Kerch State Maritime Technological University. Current interests include studying the properties of superhydrophobic surfaces in seawater.

Aleksey Ukolov, Candidate of Physical and Mathematical Sciences. Received Ph.D. degree in solid state physics in 2014 at Kharkiv National University after V. N. Karazin, Kharkov, Ukraine. Currently, docent of the Department of Mathematics, Physics and Informatics of the Kerch State Maritime Technological University. Current interests include the study of low-dimensional structures in near-surface layers of solids.